FAULT DIAGNOSIS FOR GRID-CONNECTED POWER CONVERTERS

by

Tamer Kamel

M.Sc., Cairo University, 2010

A Dissertation Submitted in Partial Fulfillment of
the Requirements for the Degree of

Doctor of Philosophy

in the Graduate Academic Unit of Electrical and Computer Engineering

Supervisors: Yevgen Biletskiy, PhD, Electrical and Computer Engineering
Liuchen Chang, PhD, Electrical and Computer Engineering

Examining Board: Gerhard Dueck, PhD, Computer Science, Chair
Maryhelen Stevenson, PhD, Electrical and Computer Engineering
Saleh Saleh, PhD, Electrical and Computer Engineering

External Examiner: Mohamed El-Hawary PhD, Electrical and Computer Engineering,
Dalhousie University

**This dissertation is accepted by the
Dean of Graduate Studies**

THE UNIVERSITY OF NEW BRUNSWICK

February, 2015

© Tamer Kamel, 2015

ABSTRACT

The reliability and functionality of power electronic converter systems (PECS) are of critical importance for industrial, commercial, aerospace, and other applications. One of the key requirements to ensure reliable functions of PECS is the behavior of the PECS during fault conditions. Characterizing the behavior of PECS during the fault conditions can provide a perspective for improving the design, protection and fault tolerant control.

In general, faults in switching elements of PECS can be classified as Short Circuit (S-C) faults, Open Circuit (O-C) faults, and degradation faults. S-C faults in most cases cause an overcurrent condition that is readily detected and acted upon by standard protection systems, such as over-current, under-voltage or over-voltage protection. However, the degradation faults, as well as O-C faults often do not produce high currents that can trigger fault protection; rather they cause system malfunction or performance degradation. Since the standard protection system may not detect these fault types, their diagnoses become critical for PECS.

The main objective of this dissertation is to investigate and develop new fault diagnostic algorithms for a typical single-phase grid-connected power converter with its DC capacitor banks, as well as to identify the unbalance input voltage to the converter. The power converter in this research consists of three main subsystems: the three-phase uncontrolled rectifier, the boost chopper, and the single-phase inverter circuits. The diagnostic algorithms have been investigated, designed, and implemented as follows: detection of unbalance three-phase input voltage, detection of O-C faults in the rectifier circuit, detection of O-C in the boost chopper circuit, detection of O-C in the inverter circuit, and detection of O-C fault and capacitor aging in the DC capacitor banks.

The constraint for designing the desired fault diagnostics algorithm is the existing number of sensors in the PECS under study. This constraint is incorporated in this work to allow maximum integration of the developed diagnostics with low and medium size PECS.

ACKNOWLEDGEMENTS

For their advice and directions from the initial stages of my PhD program to their help with the final draft of this thesis, I owe extreme debt of gratitude to my supervisors Professors Liuchen Chang and Yevgen Biletskiy. Their help and support were absolutely invaluable.

It gives me great pleasure in acknowledging the support and help of Dr. Riming Shao.

I also would like to thank Mehdi Rahiminejad for his cooperation during the implementation of the experiments of this thesis.

I owe my deepest gratitude to Ms. Cormier, Ms. Burke, Ms. Annett and all the ECE staff for their keen support and attitude.

For her support, care, infinite patience and understanding, million thanks to my wife Thnaa Abdalaal.

For their support and love, my parents, brothers, and family.

Table of Contents

ABSTRACT ……ii

ACKNOWLEDGEMENTS iv

Table of Contents v

List of Tables ix

List of Figures x

List of Abbreviations and Symbols xv

Chapter 1: Introduction 1

1.1 Preface 1

1.2 Problem Statement 3

1.3 Literature Review 5

1.4 Thesis Layout 9

Chapter 2: System Architecture 11

2.1 Introduction 11

2.2 Three-Phase Rectifier 12

2.3 Boost Chopper 13

2.4 Inverter 14

2.5 Summary 15

Chapter 3: Fault Diagnostics in Simulation Environment 16

3.1 Introduction 16

3.2 Fault Diagnosis Methodologies 16

3.2.1. Rectifier fault diagnosis 18

3.2.2. Inverter fault diagnosis 25

3.2.3. Boost chopper fault diagnosis 30

3.3 Factors Influencing Fault Diagnosis 34

3.3.1. Variations in the input supply voltage 34

3.3.2. Variations in the output power 34

3.3.3. Variations in the system parameters 34

3.3.4 Measurements errors 35

3.3.5. The effect of the faults on diagnostic algorithms 35

3.4 Comparison between the Proposed and the Previous Fault Diagnostic Algorithms

……..38

3.5 Fault Diagnosis Evaluation in the Simulation Environment 42

3.5.1. Rectifier fault diagnosis evaluation 42

3.5.2. Inverter fault diagnosis evaluation 43

3.5.3. Boost chopper fault diagnosis evaluation 44

3.6 Summary 45

Chapter 4: Fault Diagnoses in Experimental Environment 47

4.1 Preface 47

4.2 Implementation of the FFT algorithm in the converter DSP 48

4.3 Fault Diagnoses Methodologies 50
4.3.1. Diagnosis methodology for the rectifier O-C faults 50
4.3.2. Diagnosis methodology for the input voltage unbalance 58
4.3.3. Diagnosis methodology for the boost chopper O-C faults 59
4.3.4. Diagnosis methodology for the inverter O-C faults 60
4.4 Fault Diagnoses Evaluation in the Experimental Environment 63
4.4.1 Evaluation of the rectifier O-C fault diagnosis 64
4.4.2 Evaluation of the input voltage unbalance diagnosis 67
4.4.3 Evaluation of the boost chopper O-C fault diagnosis 70
4.4.4 Evaluation of the inverter O-C fault diagnosis 74
4.4.5 On-line testing for the proposed Fault diagnostic algorithms 76
4.5 Summary 77
Chapter 5: ANFIS-Based Diagnosis for O-C Faults in Power Converter 79
5.1 Preface 79
5.2 Adaptive Neuro Fuzzy Inference System (ANFIS) Structure 80
5.2.1 Layer 1: fuzzification layer 83
5.2.2 Layer 2: inference mechanism layer 86
5.2.3 Layer 3: defuzzification layer 86
5.2.4 Layer 4: output layer 87
5.3 ANFIS Fault Diagnostic Algorithm 89

5.4 ANFIS Fault Diagnosis Evaluation 94

5.5 Summary 100

Chapter 6: ANFIS-Based Diagnosis for DC Capacitor Banks Faults in Power Converter 102

6.1 Preface 102

6.2 Capacitor Banks Configuration 105

6.3 Fault Diagnostic Methodology of the Capacitor Banks 106

6.3.1 Factors influence the ripple of the capacitor banks output voltage 106

6.3.2 Ripple amplitude behaviors in the capacitor banks 107

6.3.3 Fault detection and classification of the capacitor banks 110

6.4 ANFIS Fault Diagnostic Algorithm 113

6.5 ANFIS Fault Diagnosis Evaluation 117

6.6 Summary 124

Chapter 7: Contributions and Future Work 125

7.1 General Summary 125

7.2 Major Contributions 126

7.3 Future Work 127

References 129

Appendix A 138

Curriculum Vitae

List of Tables

Table 3-1 Relationship between the harmonic order and the sequence…….18

Table 3-2 Classes indices for the rectifier circuit……..26

Table 3-3 Comparison between the former and proposed fault diagnostic methods…….39

Table 4-1 Relationship between the input frequency and the sampling frequency…..…49

Table 4-2 Relationship between the FFT output indices and the harmonic components.57

Table 4-3 The UN classes at different input frequencies at Rs = 1, 1.5, and 2 ohms……68

Table 4-4 Fault diagnostic index at normal and fault conditions……...76

Table 5-1 Two passes in the hybrid learning procedure for ANFIS [50]……..…89

Table 5-2 The inputs of the ANFIS diagnostic unit……...…91

Table 5-3 The output indices of the ANFIS diagnostic unit……..92

Table 5-4 The training error for different combinations of the input and output membership functions (mf)……94

Table 5-5 The MAE and %E for the testing conditions……...…..……..101

Table 6-1 The inputs of the ANFIS diagnostic unit…….114

Table 6-2 The output indices of the ANFIS diagnostic unit……115

Table 6-3 The MAE and %E for the testing conditions……...……124

List of Figures

Figure 1-1 Block diagram of PECS [1]...……1

Figure 1-2. Power processor block diagram [1]...……2

Figure 1-3. Control, energy, and power electronics are interrelated [2]...……...2

Figure 1-4. Horizontal axis wind energy conversion system [3].....4

Figure 1-5. Chart diagram for the diagnostic methodologies for the O-C faults and the input voltage unbalance in PECSs…….…..6

Figure 2-1. Grid connected power electronic converter under the study……..….11

Figure 2-2. Power electronic converter board…….....12

Figure 2-3. Block diagram of the control loop for the boost chopper circuit [42]..…..…14

Figure 2-4. Block diagram of the control loop for the inverter circuit [42]……..15

Figure 3-1 Rectifier output voltage at (a) Normal conditions (b) Fault conditions……...19

Figure 3-2 Rectifier circuit under the study……...20

Figure 3-3 10% unbalance input voltage for phase A at f_o = 60Hz (a) The three-phase voltages waveforms (b) V_R waveform……..……22

Figure 3-4 10% Unbalance input voltage at f_o =20 Hz…….23

Figure 3-5 10% Unbalance input voltage at f_o =40 Hz…….23

Figure 3-6 10% Unbalance input voltage at f_o =80 Hz…….24

Figure 3-7 Proposed fault diagnosis for unbalance and rectifier faults…….25

Figure 3-8 Three-phase inverter circuit…….26

Figure 3-9 Inverter circuit under the study …….....28

Figure 3-10 Proposed fault diagnosis for Inverter O-C faults……...…29

Figure 3-11 Boost chopper circuit within the system under the study……..……30

Figure 3-12 O-C fault for the boost chopper circuit at a) The switch T b) the switch D...32

Figure 3-13 Proposed fault diagnosis for boost chopper circuit……..…….33

Figure 3-14 Flow chart diagram for the proposed fault diagnoses in power converter.....37

Figure 3-15 Simulated results for the proposed unbalance fault diagnosis……...43

Figure 3-16 Simulated results for the proposed rectifier O-C fault diagnosis……...44

Figure 3-17 Simulated results for the inverter fault diagnosis…….……..45

Figure 3-18 Simulated results for the boost chopper fault diagnosis……46

Figure 4-1 Band pass filter…….51

Figure 4-2 Rectifier output voltage at normal conditions……..51

Figure 4-3 D1 O-C fault at f_o = 80 Hz a) VR waveform b) Rectifier circuit with faulted diode……...53

Figure 4-4 D1 and D4 O-C fault at f_o = 80 Hz a) VR waveform b) Rectifier circuit with faulted diodes…….55

Figure 4-5 Single-phase inverter under the study……..60

Figure 4-6 I_a waveform at normal condition…….…….61

Figure 4-7 I_a waveform at T1 or T4 O-C fault conditions…….....61

Figure 4-8 I_a waveform at T2 or T3 O-C fault conditions…….62

Figure 4-9 The experimental setup for the system under the study……...65

Figure 4-10 $Spect_{norm1}$ at normal and rectifier O-C fault conditions…….…..….65

Figure 4-11 Rectifier O-C faults a) Class C6 b) Class C3.....…...66

Figure 4-12 Proposed rectifier O-C fault diagnosis……...……66

Figure 4-13 $Spect_{norm2}$ at normal and input voltage unbalance conditions……....69

Figure 4-14 Proposed input unbalance voltage diagnosis……..70

Figure 4-15 The AC power supply……71

Figure 4-16 I_{BR} at normal and switch T O-C fault conditions.....71

Figure 4-17 I_{BAVG} at normal and diode D O-C fault conditions……73

Figure 4-18 Proposed boost chopper O-C fault diagnosis…….....73

Figure 4-19 I_{aAVG} at normal and inverter O-C fault conditions…….....74

Figure 4-20 Proposed inverter O-C fault diagnosis……...75

Figure 4-21 X_{FD} at different normal and fault conditions……..77

Figure 5-1 The architecture of the ANFIS…….82

Figure 5-2 Triangular membership function at [a b c] = [2 5 7]……84

Figure 5-3 Trapezoidal membership function at [a b c d] = [1 3 7 9]……...……85

Figure 5-4 Gaussian membership function at [a b] = [2 5]……86

Figure 5-5 Circuit diagram for the power converter……..90

Figure 5-6 ANFIS network with its inputs and output indices for the O-C faults in power converter…...…….93

Figure 5-7 ANFIS outputs and target at normal conditions……..95

Figure 5-8 ANFIS outputs and target at rectifier fault classes at SNR 30 dB……...…96

Figure 5-9 ANFIS outputs and target at rectifier fault classes at SNR 20 dB……...…96

Figure 5-10 ANFIS outputs and target at T O-C fault conditions…….97

Figure 5-11 ANFIS outputs and target at D O-C fault conditions…….97

Figure 5-12 ANFIS outputs and target at T1 or T4 Gate Drive O-C fault conditions…...98

Figure 5-13 ANFIS outputs and target at T2 or T3 Gate Drive O-C fault conditions…...98

Figure 5-14 ANFIS outputs and target at T1 or T4 IGBT O-C fault conditions……...99

Figure 5-15 ANFIS outputs and target at T2 or T3 IGBT O-C fault conditions……...…99

Figure 6-1 Distribution of failures for each power component in power converters, at Ta = 250C [55]……..…102

Figure 6-2 V_1 versus V_S at normal situations…….…….108

Figure 6-3 V_2 versus V_S at normal situations…….…….109

Figure 6-4 ANFIS network with its inputs and output indices for the capacitor banks fault in the power converter…….115

Figure 6-5 ANFIS outputs and target at normal conditions where $m_1=n_1=m_2=n_2=1$.....118

Figure 6-6 ANFIS outputs and target at normal conditions where $m_1=m_2=0.9$ and $n_1=n_2=1.5$…….118

Figure 6-7 ANFIS outputs and target at capacitor aging for C1, where $m_1=0.65$ and $n_1=2.75$, while $m_2=n_2=1$……...119

Figure 6-8 ANFIS outputs and target at capacitor aging for C1, where $m_1=0.55$ and $n_1=3.25$, while $m_2=n_2=1$……..…….119

Figure 6-9 ANFIS outputs and target at capacitor aging for C2, where $m_2=0.65$ and $n_2=2.75$, while $m_1=n_1=1$……...120

Figure 6-10 ANFIS outputs and target at capacitor aging for C2, where $m_2=0.55$ and $n_2=3.25$, while $m_1=n_1=1$……..…….120

Figure 6-11 ANFIS outputs and target at O-C fault for C1, where one capacitor is disconnected from the bank…….121

Figure 6-12 ANFIS outputs and target at O-C fault for C1, where two series capacitor are disconnected from the bank…….121

Figure 6-13 ANFIS outputs and target at O-C fault for C1, where two parallel capacitor are disconnected from the bank……...122

Figure 6-14 ANFIS outputs and target at O-C fault for C2, where one capacitor is disconnected from the bank…….122

Figure 6-15 ANFIS outputs and target at O-C fault for C2, where two series capacitor are disconnected from the bank…….123

Figure 6-16 ANFIS outputs and target at O-C fault for C2, where two parallel capacitor are disconnected from the bank……...123

List of Abbreviations and Symbols

List of Abbreviations

Abbreviations	Full Meaning
ANFIS	Adaptive Neuro Fuzzy Inference System
ANN	Artificial Neural Network
APD	Anti-Parallel Diode
C	Capacitance
DSP	Digital Signal Processor
ESL	Equivalent Series Inductance
ESR	Equivalent Series Resistance
FFT	Fast Fourier Transform
FIS	Fuzzy Inference System
FVFF	Fixed Voltage Fixed Frequency

MAE	Maximum Absolute Error
MF	Membership Function
MPPT	Maximum Power Point Tracking
O-C	Open Circuit
PCA	Principal Component Analysis
PECS	Power Electronic Converter Systems
PWM	Pulse Width Modulation
S-C	Short Circuit
SNR	Signal to Noise Ratio
SVM	Support Vector Machines
VVVF	Variable Voltage Variable Frequency
WECS	Wind energy Conversion System

List of Symbols

Symbol	Meaning
V_S	Line input Voltage
V_R	Output Rectifier Voltage
I_R	Output Rectifier Current
V_B	Output Boost Chopper Voltage
I_B	Output Boost Chopper Current
V_g	Output Inverter Voltage
I_a	Output Inverter Current
$P_{desired}$	Desired Output Power
k	Duty Factor of Boost Chopper
V_{RAVG}	Average value of the Output Rectifier Voltage
V_{BAVG}	Average value of the Output Boost Chopper Voltage

V_{Smax}	Peak Value of the Line Input Voltage
$VB_{desired}$	Reference value for Output Boost Chopper Voltage
I_{dm}	Reference value for Output Inverter Current
V_a, V_b, and V_c	Three phases Voltages
V_o, V_p, and V_n	Three Sequence Voltages
V_{R2}	2^{nd} Harmonic Component of the Rectifier Output Voltage
I_{park}	Park Current
I_{a1}	1^{st} Harmonic Component of the Inverter Output Current
I_{an}	Inverter Output Current at Normal Conditions
P.F	Inverter Output Power Factor
I_{RAVG}	Average value of the Output Rectifier Current
I_{BAVG}	Average value of the Output Boost Chopper Current
I_{BR}	Difference between the average values of I_{RAVG} and I_{BAVG}

$Spect_1$	Spectrum over the 1st and the 2nd harmonics of the Rectifier Output Voltage
$Spect_{norm1}$	Normalized Spectrum over the 1st and the 2nd harmonics of the Rectifier Output Voltage
$Spect_2$	Spectrum over the 2nd harmonics of the Rectifier Output Voltage
$Spect_{norm2}$	Normalized Spectrum over the 2nd harmonics of the Rectifier Output Voltage
I_{aAVG}	Average value of the Output Inverter Current
I_{aABS}	Absolute of the Average value of the Output Inverter Current
UN	Unbalance Ratio
I_{a0N}	Normalized Average Value of the Output Inverter Current
I_{a1N}	Normalized Component of the 1st harmonic order of Output Inverter Current
C_1	Total Capacitance of the 1st Capacitor Bank in the Power Converter under Study
ESR_1	Total ESR of the 1st Capacitor Bank in the Power Converter under Study
C_2	Total Capacitance of the 2nd Capacitor Bank in the Power Converter under Study
ESR_2	Total ESR of the 2nd Capacitor Bank in the Power Converter under Study

V_1	6^{th} Harmonic Component of the Rectifier Output Voltage
V_2	2^{nd} Harmonic Component of the Boost Chopper Output Voltage
f_i	Input Voltage Frequency
f_o	Grid Voltage Frequency
V_{1th}	V_1 at Capacitor Aging Conditions for 1^{st} Capacitor bank
V_{2th}	V_2 at Capacitor Aging Conditions for 2^{nd} Capacitor bank
C_{1ag}	C_1 at Capacitor Aging Conditions for 1^{st} Capacitor bank
ESR_{1ag}	ESR_1 at Capacitor Aging Conditions for 1^{st} Capacitor bank
C_{2ag}	C_2 at Capacitor Aging Conditions for 2^{nd} Capacitor bank
ESR_{2ag}	ESR_2 at Capacitor Aging Conditions for 2^{nd} Capacitor bank
$\hat{V}_{1th}$	Estimated Value for V_{1th}
$\hat{V}_{2th}$	Estimated Value for V_{2th}
n_1	Variation Ratio for C_1

m_1	Variation Ratio for ESR_1
n_2	Variation Ratio for C_2
m_2	Variation Ratio for ESR_2
$\%V_1$	Percentage value of the Measured V_1 over $\hat{V}_{1th}$
$\%V_2$	Percentage Value of the measured V_2 over $\hat{V}_{2th}$
ΔV_1	Voltage Differences between Two Successive Samples of the V_1
ΔV_2	Voltage Differences between Two Successive Samples of the V_2
$ANFIS_O$	ANFIS Output
$ANFIS_T$	ANFIS Target
MAE	Maximum Absolute Error
%E	Percentage Maximum Error

Chapter 1: Introduction

1.1 Preface

The fundamental function of a power electronic converter system (PECS) is to convert the electrical power supplied at certain frequency so that it can meet pre-defined set of conditions. Such conditions include certain voltage level, current level, and/or frequency bands. Figure 1-1 shows generic block diagram for a PECS [1]. The power processors (Figure 1-1) usually consist of more than one power conversion stage (Figure 1-2), where the operation of these stages is decoupled on an instantaneous basis by means of energy storage elements such as capacitors and inductors.

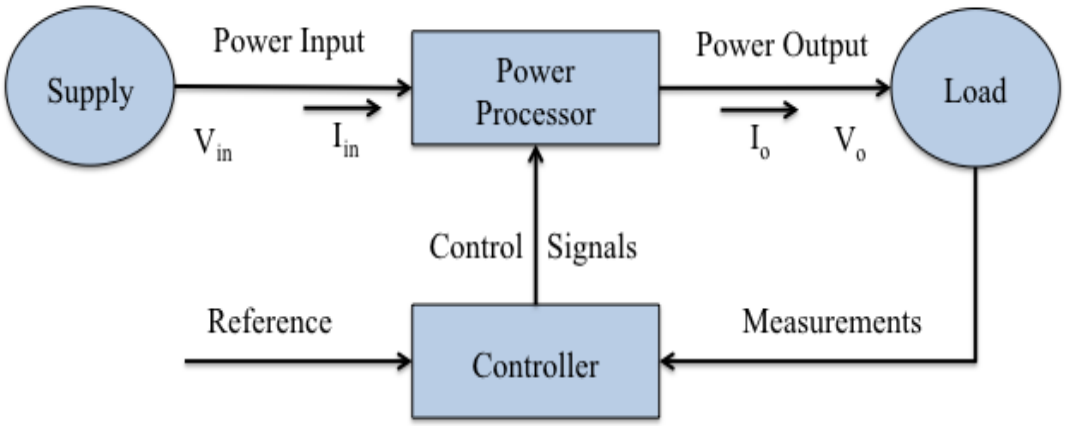


Figure 1-1. Block diagram of PECS [1]

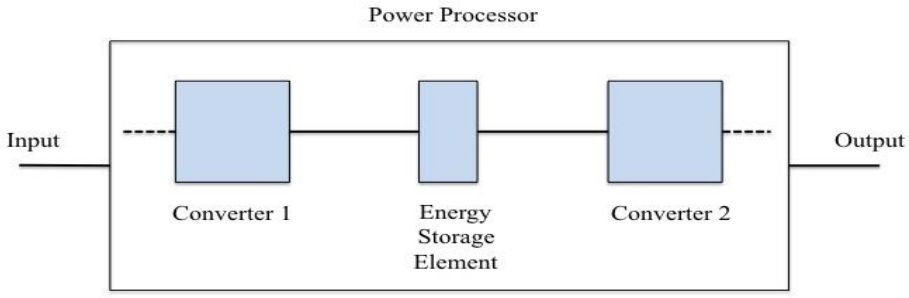


Figure 1-2. Power processor block diagram [1]

Figure 1-3 shows the significance of PECSs as the corner stone in a wide range of industrial applications, including renewable energy applications, motor drives, power systems, etc.. The power electronic system represents the intersection mid-point at which the topics of energy systems, electronics, and control converge and combine [2].

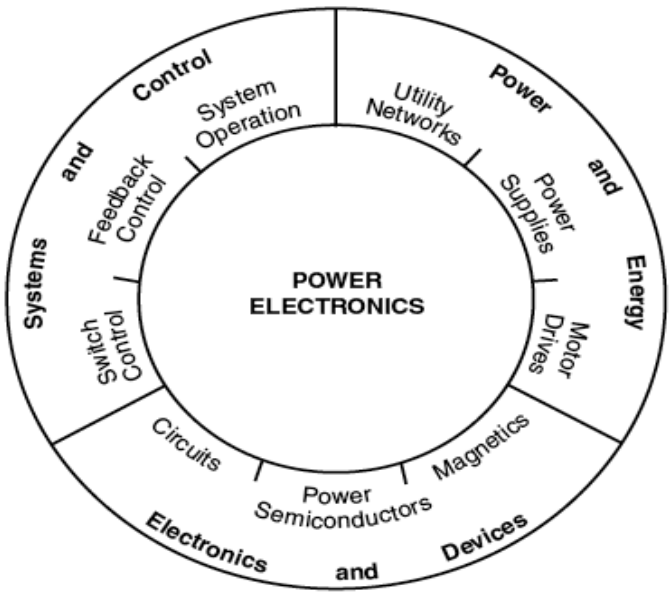


Figure 1-3. Control, energy, and power electronics are interrelated [2]

The aspects of research trends for PECS include; control of the output voltages and currents in different topologies of PECS, development of the maximum power point tracking (MPPT) techniques, implementation of the on-line fault diagnosis, and establishment of the fault-tolerant control systems. This thesis mainly focuses on developing new fault diagnostic algorithms for a single-phase grid-connected power converter with its DC capacitor banks, as well as identifying the unbalance input voltage to the converter.

1.2 Problem Statement

Wind energy conversion systems (as presented in Figure 1-4) are one of the growing areas of application for PECS. The PECS investigated in the present research is used for small wind turbines and includes a three-phase diode rectifier, a dc-dc converter (boost chopper) and a single-phase inverter.

Due to the proliferation of automation in industrial processes, PECSs become more complex and are prone to stresses leading to failures. A failure in one of the power switching elements in a PECS decreases system performance and results in de-function of the system and possible physical damages

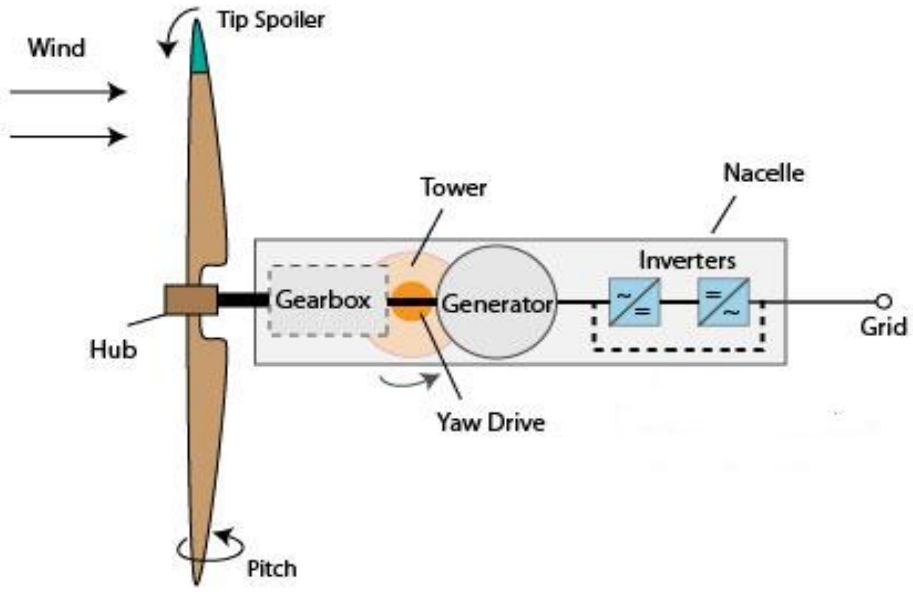


Figure 1-4. Horizontal axis wind energy conversion system [3]

Moreover, if the fault is not quickly detected and rectified, it can lead to a hard failure. Hence, to reduce the failure rate and to prevent unscheduled shutdown, real-time fault detection and isolation schemes must be adopted in PECSs.

Conventional schemes of improving the reliability (such as: conservation design, hardware redundant operation, or protection system) do not provide early detection and isolation of the faults; therefore, a lengthy and costly procedure may be required for searching and clearing defects.

Early fault detection prevents further critical breakdowns. It can prevent more serious and expensive damages for the PECSs with longer repair times. Locating the fault may be also of utmost importance as far as safety is concerned. Incipient fault detection is particularly important for medium and high power applications. However, the additional

cost of the diagnostic system must be kept low. As a result, the monitoring and diagnostic system must be as simple and easy to implement as possible.

The objective of the research presented in this thesis is to investigate and implement new diagnosis methodologies for open circuit (O-C) faults in the power switching elements of the PECS, as well as the identifying the unbalance input voltage to the converter. In general, O-C faults do not trigger standard protection systems implemented in the power converters, but rather cause system malfunction or performance degradation. Such behavior of O-C fault indicates the critical demands for diagnosing these faults. Furthermore, the developed methodologies are established without including any additional sensors or other hardware devices, which are significant for the typical commercial power converters used in small wind turbines.

The possibility of multiple faults occurring at the same instant is very low, and thus is not considered. Since an efficient protective circuit should detect the primary fault once it takes place, so the secondary fault as a consequence of the primary fault has not a possibility to be occurred. Therefore, the secondary fault has been excluded from consideration as well [4].

1.3 Literature Review

The development of fault diagnostic methods has gained interest in recent years. Figure 1-5 provides a brief summary for existing diagnostic methodologies for open circuit (O-C) faults and voltage unbalance faults in PECSs.

The Park Vector and the slope method are considered as the most popular methods in identifying the O-C faults in the three-phase inverters and rectifiers [5-8]. These

methods require the measurements of the three-phase currents. Sliding mode observer is implemented for identifying the faults in the modular multilevel converter [9] using the measurements of the arm currents of the converter, as well as the voltage across each cell of the multilevel converter.

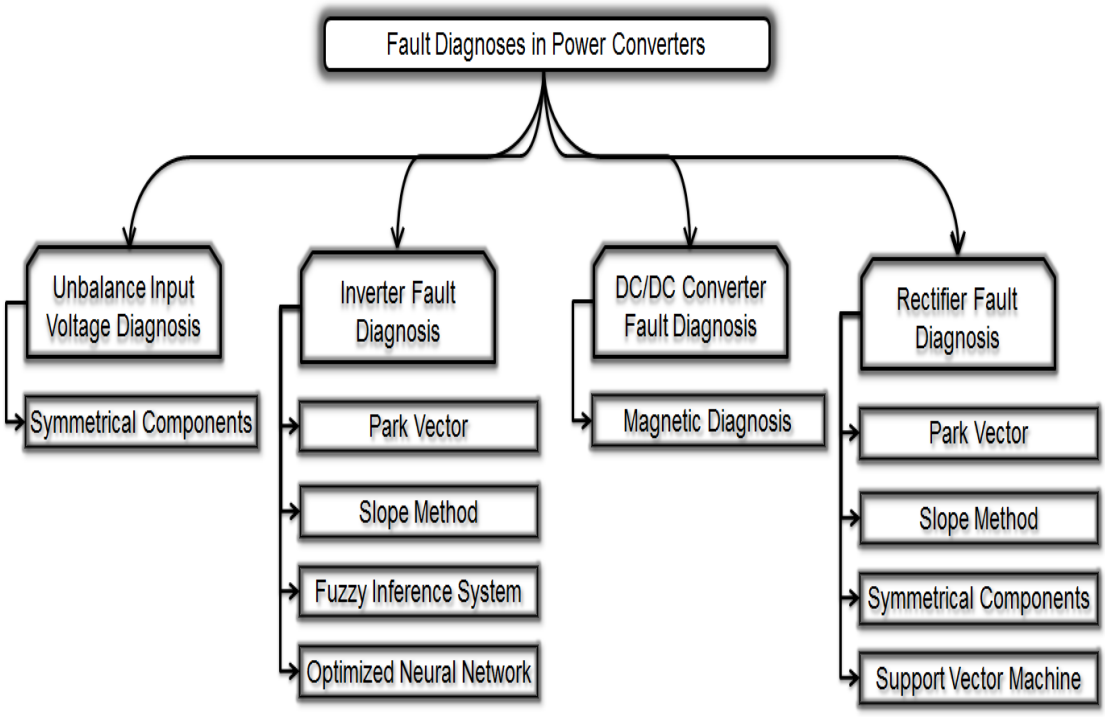


Figure 1-5. Chart diagram for the diagnostic methodologies for the O-C faults and the input voltage unbalance in PECSs.

Machine learning based approach for fault detection and isolation based on the complex wavelet is provided in [10], where inputs are the three-phase currents of the inverter. Moreover, advanced techniques as fuzzy inference system [11-12] and neural networks [13-15] are utilized for the inverter diagnosis, as well as support vector machines [16-17] for the rectifier diagnosis.

Other researches [18-21] employ the measurements of either the three-phase currents or the three-phase voltages in the O-C fault detection of the power inverters. In addition, the research work in [22] provides a monitoring system based on the discrete wavelet transform to detect O-C faults, which occur in the matrix converter topology.

The use of the gate-voltage signals for the inverter faults detection is reported in [23]. O-C fault diagnosis based on the measurements of three-phase currents and the DC-link voltage is presented in [24] for the closed-loop controlled AC regenerative drives. Failure detection system for multi-pulse cycloconverters feeding the synchronous motors is proposed in [25]. The system is based on a newly developed switching-state estimation algorithm, which is compared with the actual switching-state pattern in order to identify the failed switch in the converter. On-line fault diagnosis methods for power transistors in the power converter are proposed in [26], in which additional current sensors are required in particular positions in the converter to obtain the diagnosis result and the fault location by logical judgment with the use of additional logical circuits. Moreover, the measured three-phase currents and their corresponding reference signals are utilized to detect the inverter O-C faults in [27].

Other research works [28-29] uses the Principal Component Analysis (PCA) and S-transform, as well as the Support Vector Machines (SVM) to detect the faults in the three-phase rectifiers. The input to the decision-making unit is the output voltage of the rectifier. Research presented in [30] uses the output rectifier voltage to detect the faults in the rectifier circuit. The output rectifier voltage is compared to a reference signal in order to obtain the residual error, which is utilized to diagnose the failure switch.

For a single-phase inverter circuit, a magnetic field probe is used in [31] to detect the magnetic field near the output inductor of the inverter. The measured waveform is utilized as the diagnostic criterion. Moreover, fault diagnosis based on D-S evidential theory and fuzzy logic is presented in [32]. The inputs to their diagnosis are the output voltage, the input voltage and the temperature of MOSFET.

Regarding the DC-DC converters, the measured magnetic field is implemented as the diagnostic criterion for the O-C faults in the DC-DC circuits [33-35]. Other fault diagnoses for the DC-DC converters are provided in [36-37] depending on the determination of the sign variations of the slope of the output current of the converter.

The unbalance of the input three-phase voltages can be identified by calculating the negative sequence component of the three-phase input voltages, in which the negative sequence becomes larger than its value in the balance conditions taking into consideration the noises and the non-ideal operations of the power converters [38-41].

In this thesis, the proposed fault diagnostic algorithms have been implemented by utilizing the relationship between the sequence components of the electrical signals with their harmonic components. The inputs to the diagnostic algorithms depend solely on the available number of measuring sensors in the commercial power converters implemented in distribution generation systems connected to small wind turbines.

A decision-making unit for the O-C fault diagnosis of the grid-connected power converters is developed by Adaptive Neuro Fuzzy Inference System (ANFIS) algorithm. This single diagnostic unit becomes responsible for detecting, classifying and locating the O-C faults of the power converter in its three main circuits: three-phase rectifier, boost chopper and single-phase inverter circuits.

Finally, another ANFIS-based fault diagnostic unit is developed for the DC capacitor banks faults in the power converter dependent only on the measurements of the output voltages of the capacitor banks, as well as the input voltage of the converter. The ANFIS diagnostic unit identifies the capacitor aging and the O-C faults in the capacitor banks.

1.4 Thesis Layout

The thesis is organized as follows.

Chapter 2 provides a summary of the power electronic converter under study. It presents the three main circuits of the converter, including a three-phase uncontrolled rectifier, boost chopper, and single-phase inverter. The two main control loops, which govern the converter operations, are provided as well.

Chapter 3 investigates and develops new methods for fault detection, localization, and diagnosis for the power electronic converter, as well as the identification of the unbalance input voltage to the converter. The proposed fault diagnoses methodologies are tested and verified in the MATLAB/Simulink environment.

Chapter 4 presents a digital signal processor (DSP)-based diagnostic algorithm, which allows the real-time detection, classification and localization of O-C faults of the power electronic converter, as well as the identification of the unbalance input voltage to the converter. The validation of the proposed fault diagnostic methodologies in the experimental environment is implemented using a coupled DC motor with AC synchronous generator scheme in order to imitate the characteristic of the wind energy conversion system.

Chapter 5 provides a novel decision-making unit for the O-C fault diagnosis of the grid-connected power converters developed with Adaptive Neuro Fuzzy Inference System (ANFIS) algorithm. The ANFIS diagnostic unit is used to detect, classify and locate the O-C faults of the power converters in its three main circuits: three-phase rectifier, boost chopper and single-phase inverter circuits.

Chapter 6 presents a novel fault diagnostic algorithm for the two DC capacitor banks in the power electronic converter under the study using the ANFIS technique. The ANFIS-based diagnostic unit is used to detect faults in the capacitor banks.

Finally, Chapter 7 includes the conclusions on the several fault diagnostic methodologies, which are proposed in the present thesis research.

Chapter 2: System Architecture

2.1 Introduction

The system under study (as illustrated in Figure 2-1) is a single-phase grid-connected power converter, which is a typical commercial power converter for small wind turbines. The power converter converts the electrical power in the variable voltage variable frequency (VVVF) form to the fixed voltage fixed frequency (FVFF) form. The supply of the converter is a wind energy conversion scheme (WECS). The converter output is a single-phase grid. The converter circuit boards are presented in Figure 2-2.

The main circuits of the converter include:

A. Rectifier, which converts the VVVF AC generated by WECS to variable DC voltage;

B. Boost chopper, which increases the DC voltage level;

C. Inverter, which converts the DC voltage to FVFF AC fed into the grid.

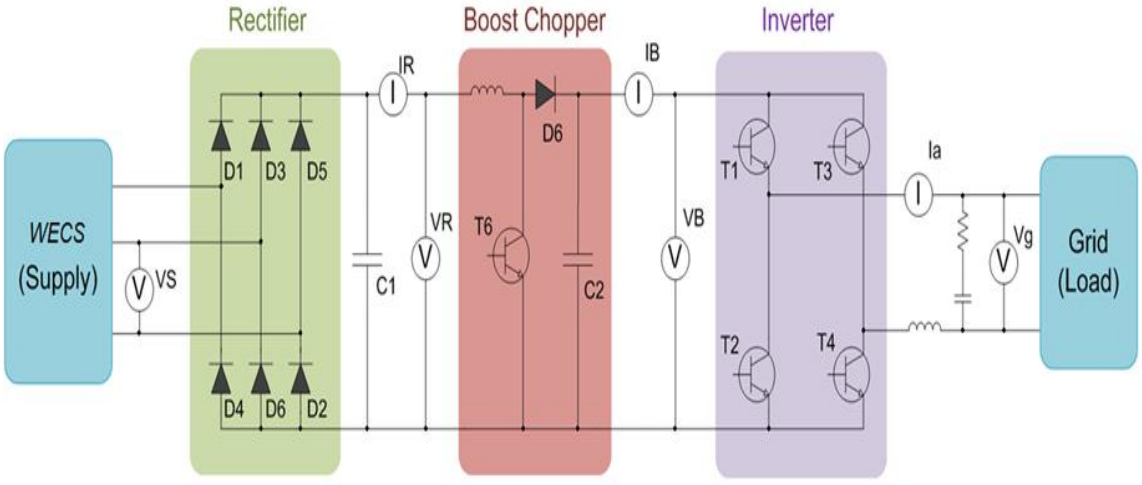


Figure 2-1. Grid connected power electronic converter under the study

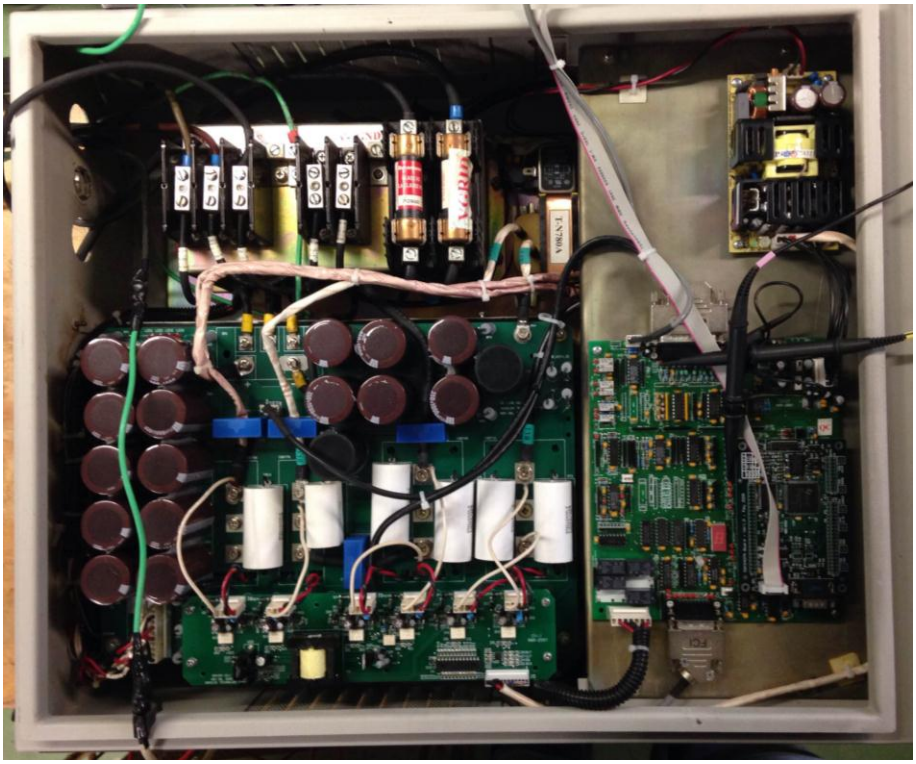


Figure 2-2. Power electronic converter board

For the converter in Figure 2-1, the available sensors are one line voltage (V_S) input to the rectifier, and the output voltages and currents for the rectifier (V_R and I_R), boost chopper (V_B and I_B), and inverter (V_g and I_a). In the following Sections, a brief description for each circuit is given with mathematical equations and/or the control diagrams.

2.2 Three-Phase Rectifier

The three-phase rectifier in this power converter is the uncontrolled type, so the relationship between its input and output voltages with a resistive load is given as follows:

$$V_{RAVG} = \frac{3 * V_{S\max}}{\pi} \tag{2.2.1}$$

where, V_{RAVG} is the average value of the output rectifier voltage and V_{Smax} is the peak value of the input line voltage of the rectifier.

2.3 Boost Chopper

The equation governing the relationship between the input and output voltages of the circuit is:

$$V_{BAVG} = \frac{V_{RAVG}}{1-k} \tag{2.3.1}$$

where, V_{BAVG} is the average values of the output voltage of the chopper and k is the duty factor of the boost chopper circuit. The duty factor is governed by a control loop in order to achieve the maximum power point tracking (MPPT). MPPT is adopted in the system under study in order to achieve the transfer of the maximum possible output power to the load at all supply conditions. The inputs to the MPPT control loop (as presented in Figure 2-3 [42]) are the desired output power ($P_{desired}$) and input voltage (V_R) and current (I_R) of the boost chopper. The PID controller controls the duty cycle by regulating its input signal, which is the error signal between the desired output power and the low pass filtered version of the measured one given in the frequency-domain (s) as follows [42]:

$$k(s) = \left(\frac{0.5s+1}{100s}\right)\left[P_{desired}(s) - \left(\frac{1}{0.01s+1}\right)V_R(s)I_R(s)\right] \tag{2.3.2}$$

where; the duty factor k becomes the output of the PID controller whose proportional, integral, and derivative gains equal to 0.5/100, 1/100, and zero respectively.

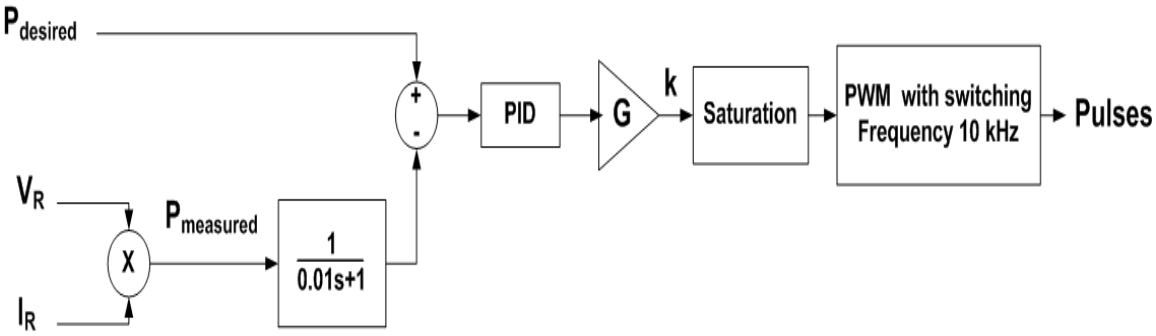


Figure 2-3. Block diagram of the control loop for the boost chopper circuit [42]

2.4 Inverter

The inverter is a single-phase type. A control system accomplishes the Pulse Width Modulation (PWM) of the inverter switches in order to provide a FVFF AC to the electric grid, as well as attain unity power factor for the output current (I_a) into the grid. The inputs to the second control loop (as shown in Figure 2-4 [42]) are the input voltage (V_B) of the inverter with its reference value ($V_{Bdesired}$), as well as the voltage (V_G) and current I_a of the grid. In this control loop, a reference value (I_{dm}) is estimated for the grid current I_a based on the low pass filtered version of the error signal between the $V_{Bdesired}$ and the measured V_B provided in the frequency-domain (s) as follows [42]:

$$I_{dm}(s)=\left(\frac{0.5s+1}{s}\right)\left(\frac{1}{0.01s+1}\right)\left[V_{Bdesried}(s)-V_B(s)\right] \quad (2.4.1)$$

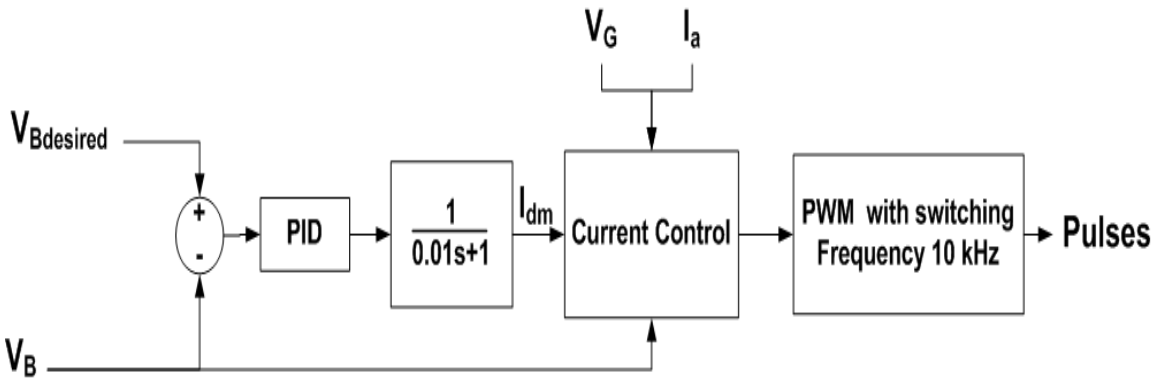


Figure 2-4. Block diagram of the control loop for the inverter circuit [42]

2.5 Summary

This chapter provides a brief description for the power electronic converter under study with its three main circuits: rectifier, boost chopper, and inverter circuits. It also presents the mathematical formulas, as well as the control loops.

Chapter 3: Fault Diagnostics in Simulation Environment

3.1 Introduction

A typical commercial power conversion system for small wind turbines is under study in the present research. The available measuring sensors of this converter are not sufficient to acquire the necessary electrical parameters used for fault diagnostic methods established in the previous research. Such a constraint leads to develop new methods in order to detect and identify the faults.

This chapter provides the proposed fault diagnostic methodologies, which are described in Section 3.2. The factors, which affect fault diagnosis, are provided in Section 3.3 followed by discussion and comparison between the proposed diagnostic algorithms and fault diagnostic algorithms of previous research in Section 3.4. The proposed fault diagnostic methodologies are verified in MATLAB/Simulink environment [43] in Section 3.5. Finally, Section 3.6 presents the summary of the proposed diagnostic algorithms in this chapter.

3.2 Fault Diagnosis Methodologies

Symmetrical components are most commonly used for the analysis of unbalanced three-phase electrical power systems. The sequence components are generated from (3.2.1),

$$\begin{bmatrix} V_o \\ V_p \\ V_n \end{bmatrix} = \frac{1}{3}\begin{bmatrix} 1 & 1 & 1 \\ 1 & a & a^2 \\ 1 & a^2 & a \end{bmatrix}\begin{bmatrix} V_a \\ V_b \\ V_c \end{bmatrix} \tag{3.2.1}$$

where: V_a, V_b, and V_c are the three phase voltages, while V_0, V_p, and V_n are the zero, positive and negative sequences respectively and $a = 1\angle 120^o$. The independence of the symmetrical components and their resultant summation follow the principle of superposition. The symmetrical components convert the three unbalanced phases into three independent sources, which improves traceability for asymmetric fault analysis and unbalance conditions. This mathematical method is widely used in the design of protective relays, which use negative-sequence voltages and currents as a reliable indicator of fault and unbalance conditions [38-41].

The Fourier series decomposes the periodic waveforms into linear combinations of sinusoidal waveforms with frequencies of integer multiples of the fundamental frequency. For a periodic and stationary signal x(t) with fundamental frequency f_0, the Fourier series can be expressed as:

$$x(t) = \sum_{k=-\infty}^{\infty} x_k e^{j2\pi k f_0 t} \tag{3.2.2}$$

where x_0 is the dc value of x(t) and x_k is the harmonic component (magnitude and phase) at each harmonic order k and can be calculated by:

$$x_k = \frac{1}{T}\int_0^T x(t).e^{-j2\pi\frac{k}{T}t}\,dt \tag{3.2.3}$$

where T is the period of the x(t), ($T = 1/f_o$).

There is a relationship between the harmonic contents in the signal and its symmetric components. Each harmonic component can be represented as positive, negative, or zero sequence (as shown in the Table 3-1), which can be extended to include more harmonics.

3.2.1. Rectifier fault diagnosis

The output voltage waveform of a three-phase rectifier in the normal condition with a filtering capacitor can be illustrated in Figure-3-1(a).

The Fourier series expansion of the rectifier output voltage with the filtering capacitor can be deduced in (3.2.4) using (3.2.2) and (3.2.3).

Table 3-1 Relationship between the harmonic order and the sequence

Harmonic order "k"	Phase A	Phase B	Phase C	Sequence
1^{st} order	$0^0 * 1 = 0^0$	$120^0 * 1 = 120^0$	$240^0 * 1 = 240^0$	A-B-C Positive Sequence
2^{nd} order	$0^0 * 2 = 0^0$	$120^0 * 2 = 240^0$	$240^0 * 2 \equiv 120^0$	A-C-B Negative Sequence
3^{rd} order	$0^0 * 3 = 0^0$	$120^0 * 3 \equiv 0^0$	$240^0 * 3 \equiv 0^0$	In Phase Zero Sequence

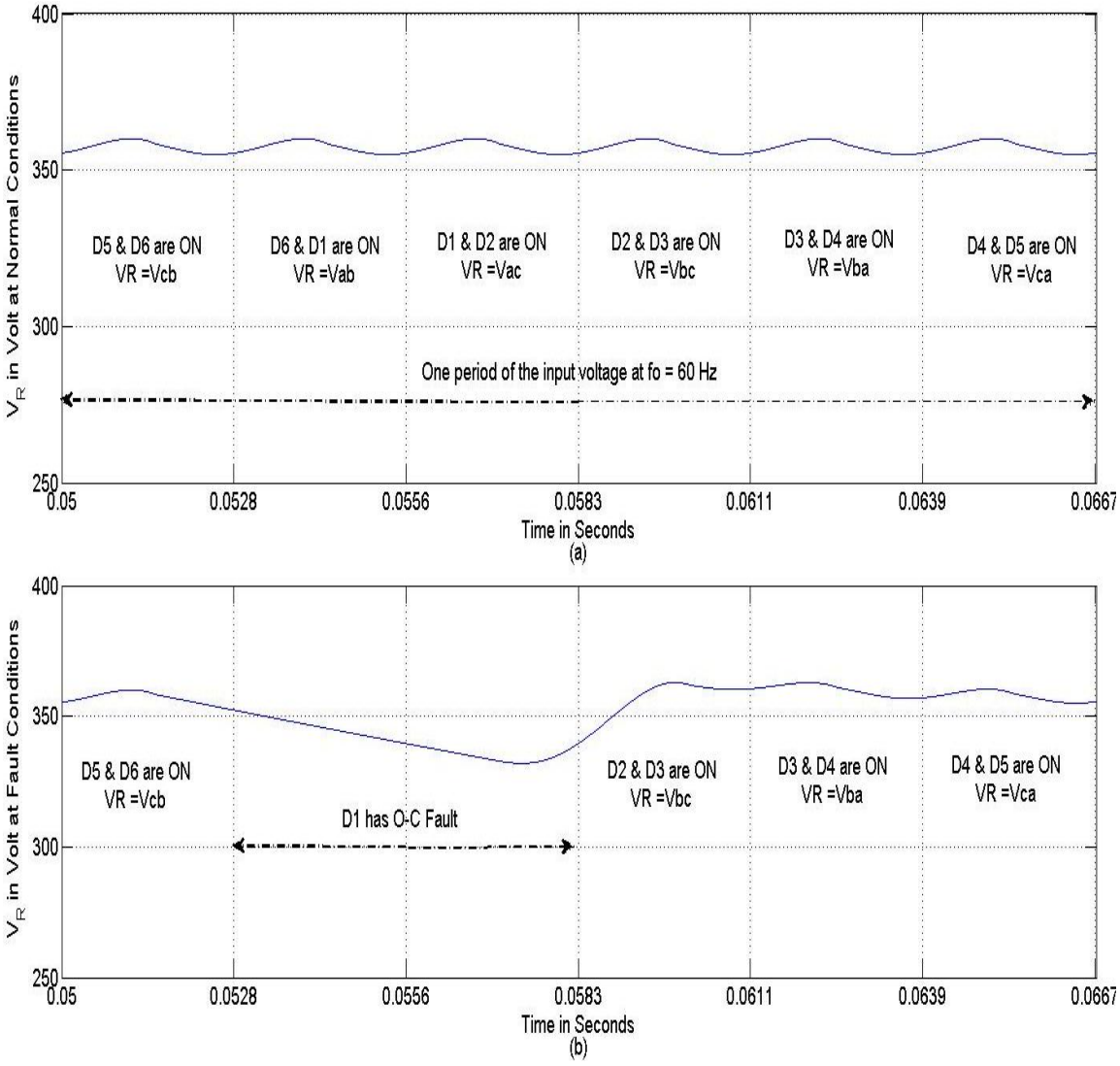


Figure 3-1 Rectifier output voltage at (a) Normal conditions and (b) Fault conditions

$$V_R(t) = \frac{3\sqrt{3}}{\pi} V_{\max} \left(1 - \sum_{k=1}^{\infty} \frac{2}{36k^2 - 1} \cos(6k\omega_o t + \theta_k) \right) \tag{3.2.4}$$

where V_{max} is the maximum input phase voltage and ω_o is the fundamental angular frequency. From Figure 3-1(a), it is shown that the predominant harmonic component in

the V_R waveform is the 6^{th} harmonic under normal operating conditions as it is verified in (3.2.4).

In normal operation of a diode bridge converter circuit, voltages and currents are symmetrical. Under fault conditions they become asymmetrical [44]. Therefore, the rectifier fault can have the same influence to the output waveforms as the unbalanced input on the output rectifier voltage V_R. The reason behind that is if one of the six diodes has an O-C fault, for instance D1 in Figure 3-2, it will disconnect the phase-A from the rectifier output. Figure 3-1(b) provides V_R at D1 O-C fault. It is shown that phase-A is missed during the D1 conduction period, and V_R will decrease till the conduction of D3 starts, where V_R will be equal to the input line voltage again.

Since the loss of one of the three-phases is typically an unbalanced three-phase condition, the rectifier faults can be treated as the unbalanced three-phase input condition with respect to V_R. As a result, the negative sequence approach can be utilized to identify both (1) the unbalanced input conditions and (2) the faults within the rectifier circuit.

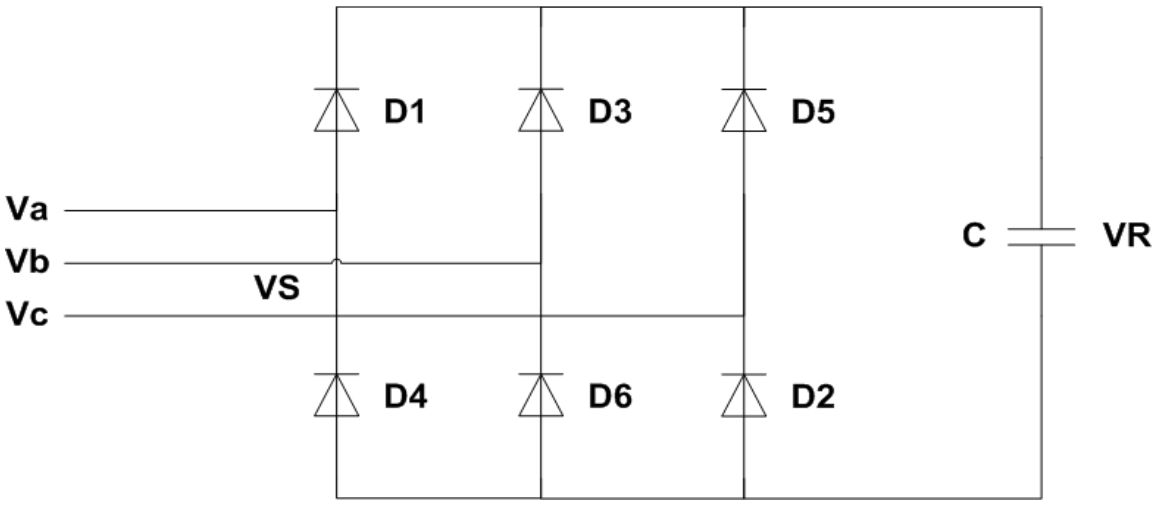


Figure 3-2 Rectifier circuit under the study

From Table 3-1, it can be seen that the 2nd harmonic component of three-phase system can represent the negative sequence component in order to detect the asymmetrical pattern in the system voltages.

However, in the system under the study, as shown in Figure 3-2, there is no access to the three-phase input voltages or the currents. Alternatively, the rectifier output voltage V_R is measured and used to detect the unbalanced input condition, as well as rectifier fault conditions.

There are six peaks in the V_R waveform over one complete period of the input three-phase supply during the normal condition as shown in Figure 3-1. These peaks are dependent on the positive and negative peaks of the input three phases. On the other hand, if one of the three phases is not balanced with the other two phases, its positive and negative peaks become dissimilar to the peaks of the other two phases. This suggests that, two of the six peaks in the V_R waveform become distinguished from the other four peaks and the time between these two peaks will be half the period of the input three-phase supply. Finally, the V_R waveform becomes distorted from its symmetrical pattern in normal conditions and the distorted pattern of its ripple has a frequency double the input frequency of the three-phase system regardless of its input frequency.

Figure 3-3 provides the three-phase voltage of the input 60 Hz supply at 10% [(1)] unbalance at phase A, as well as V_R waveform at the unbalanced conditions.

[(1)] The American National Standards Institute (ANSI) standard C84.1-1995 recommends that electrical supply systems should be designed and operated to limit the maximum voltage unbalance to 3% when measured at the electric-utility revenue meter under no-load conditions [45]. The International Electro technical Commission (IEC) recommends that the maximum voltage unbalance of electrical supply systems be limited to2% [45].

Figure 3-3 illustrates the unsymmetrical two peaks of the unbalanced phase in the three-phase voltages waveform, as well as the effect of such behavior on the V_R waveform. Figures 3-4, 3-5, and 3-6 illustrate the waveforms of V_R at input frequencies 20, 40, and 80 Hz respectively at 10% unbalance input voltage.

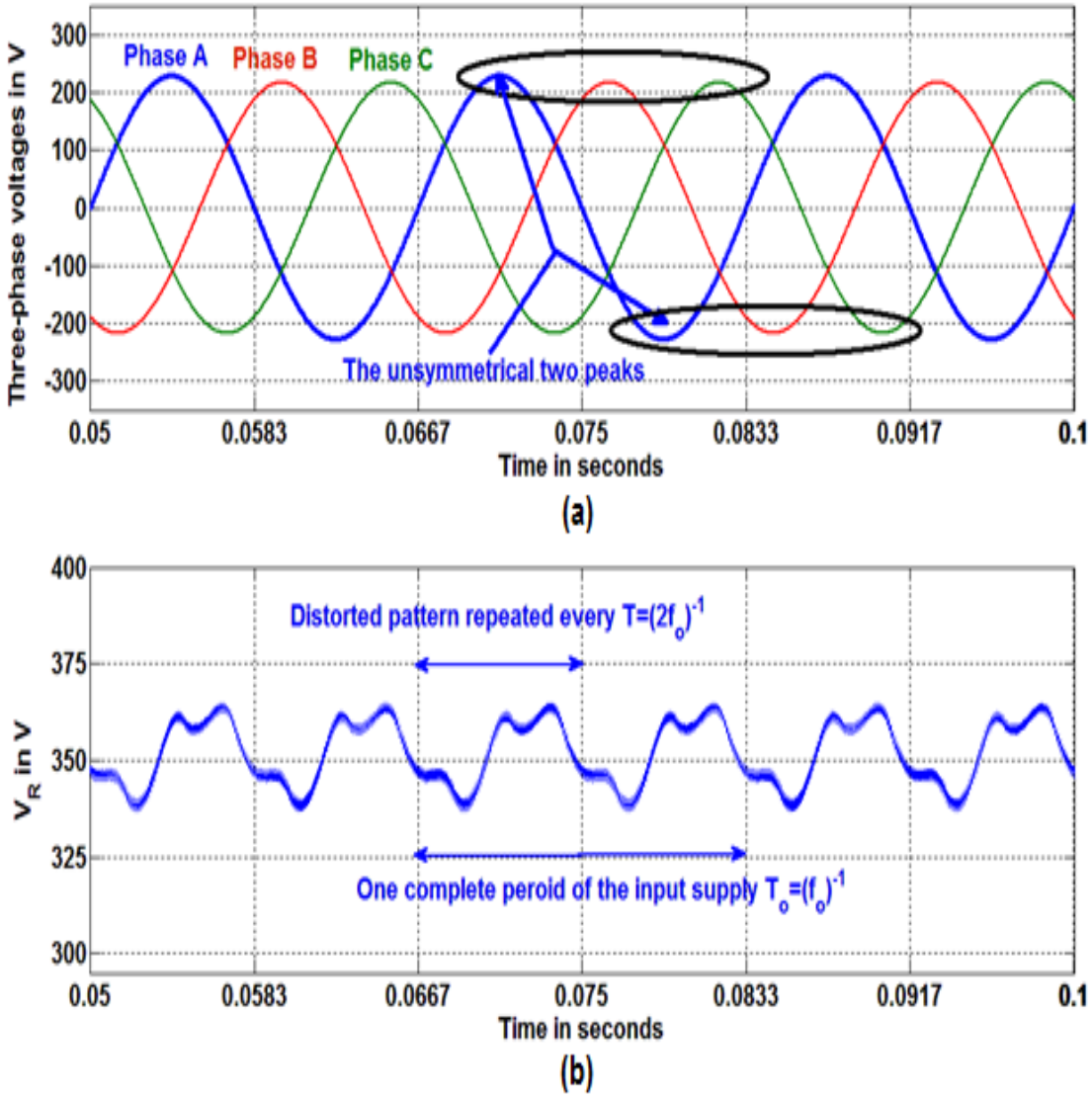


Figure 3-3 10% unbalance input voltage for phase A at f_o = 60Hz

(a) The three-phase voltages waveforms (b) V_R waveform

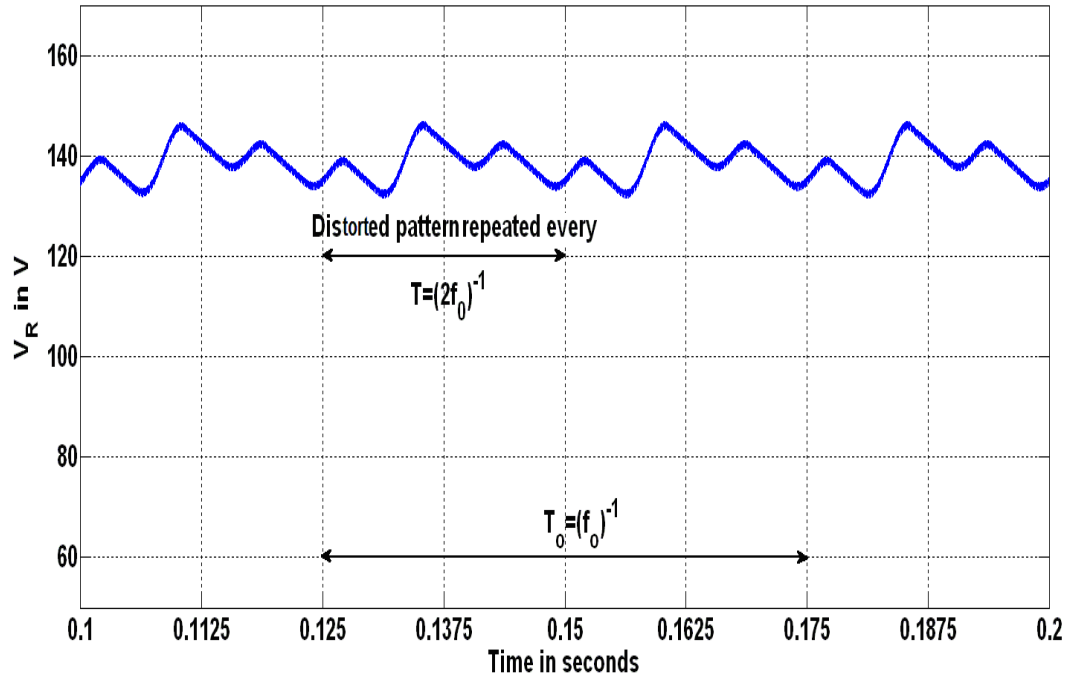


Figure 3-4 10% Unbalance input voltage at f_o =20 Hz

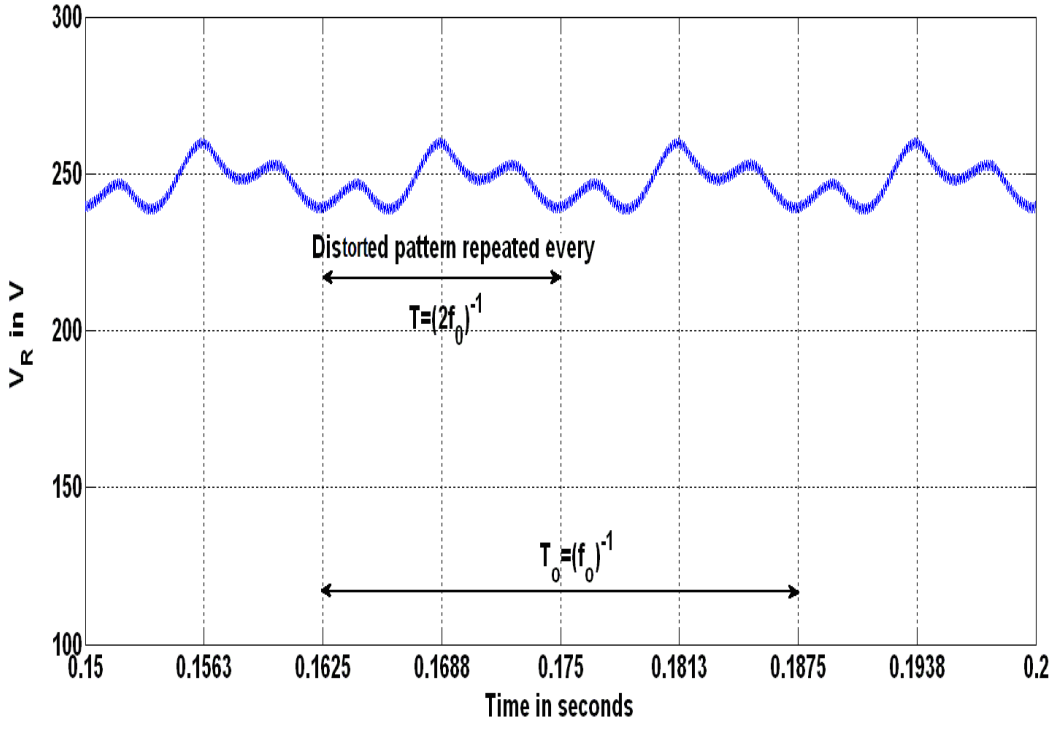


Figure 3-5 10% Unbalance input voltage at f_o =40 Hz

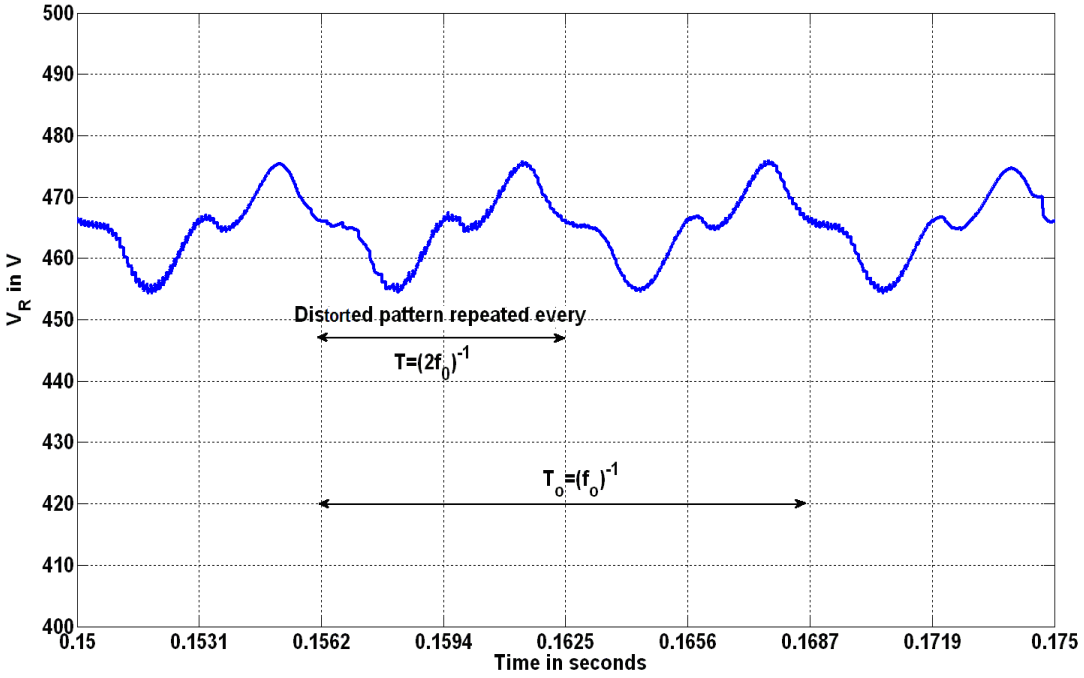


Figure 3-6 10% Unbalance input voltage at f_o =80 Hz

From these four figures, it is seen that the 2nd harmonic component of three-phase voltage is reflected on the rectifier output voltage as the V_R waveform. During the unbalanced condition, the 2nd harmonic component has a distorted pattern repeated with frequency double the input voltage frequency f_o regardless of its value. This observation as well as Table 3-1 indicate that the 2nd harmonic component of the rectifier output voltage (V_{R2}) can be used to represent the negative sequence component of three-phase input voltage, so that, V_{R2} is utilized to identify both the unbalanced input voltage condition as well as rectifier faults.

In order to make the threshold criterion independent from the input and load conditions, a normalized form of V_{R2} is used in the diagnosis by dividing the V_{R2} by the average value of the rectifier output voltage V_{RAVG}.

V_{R2} at normal operation conditions equals to zero. This value can be selected in order to differentiate between normal and fault conditions. However, due to the interference of the signals inside the converter and the measuring errors of the converter sensors, it could be slightly greater than zero. As a result, the threshold value is marginally increased above zero to 1% in order to include these non-ideal conditions in the converter operation. As a consequence, the unbalance and rectifier fault diagnoses can be proposed as shown in Figure 3-7. Table 3-2 provides all the possible classes of rectifier O-C faults with the normal condition.

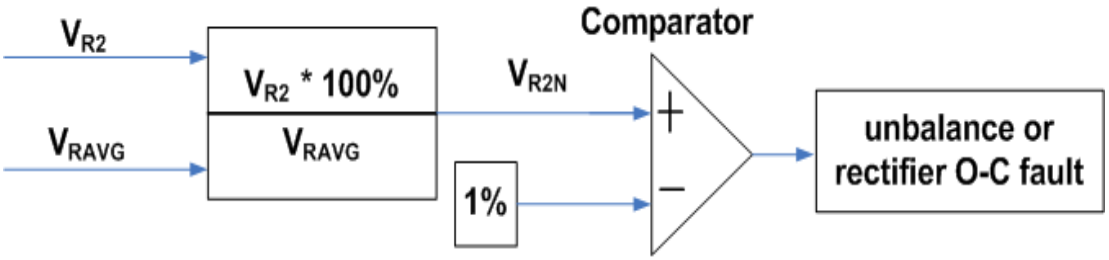


Figure 3-7 Proposed fault diagnosis for unbalance and rectifier faults

3.2.2. Inverter fault diagnosis

In three-phase inverter (Figure 3-8), the Insulated Gate Bipolar Transistor IGBT O-C fault can be detected and localized by the Park Method. In this method, the phase currents (I_A, I_B, I_C) are measured and then transformed into space vector I_{park} according to (3.2.5) [5-8]:

$$I_{park} = \frac{3}{2}(I_A + a^2 \cdot I_B + a \cdot I_C) \qquad (3.2.5)$$

Table 3-2 Classes indices for the rectifier circuit

Symbol	Class
C0	Normal Situation
C1	One Diode Open Circuited
C2	Two Diodes Open Circuited “different branch”
C3	Three Diodes Open Circuited “different branch”
C4	Two Diodes Open Circuited “same branch”
C5	Three Diodes Open Circuited “two in the same branch and one different”
C6	Two Diodes Open Circuited “Up or Down”
C7	Three Diodes Open Circuited “Up or Down”

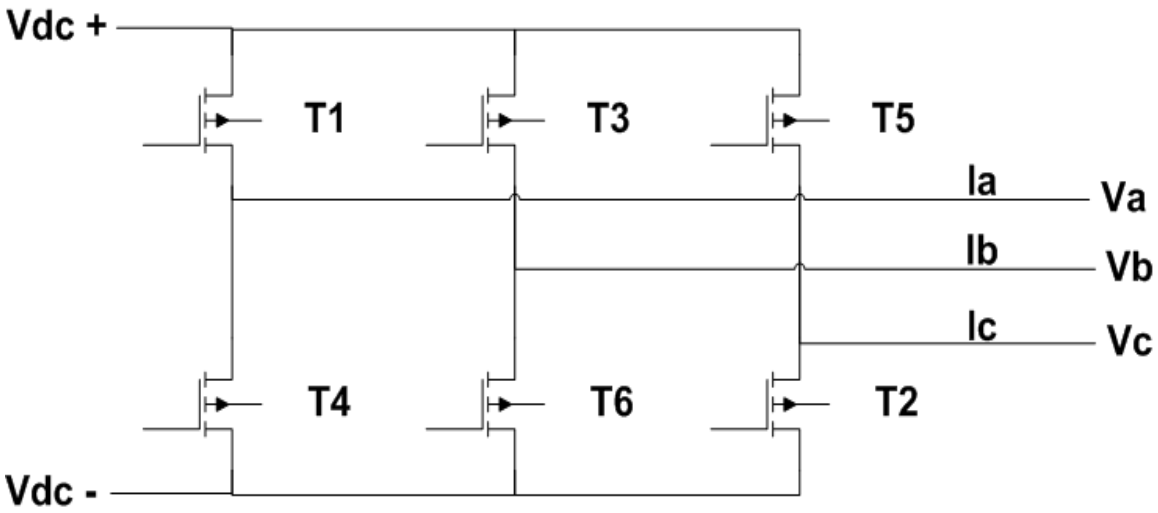


Figure 3-8 Three-phase inverter circuit

The inverter used in the present research is a single-phase inverter, where fault detection methods based on Park vector calculation, are inapplicable in this study. From (3.2.1) and (3.2.5), it is seen that the I_{park} is corresponding to the positive sequence component of the three-phase currents. Moreover, from Table 3-1, the 1^{st} harmonic component can be used as an estimator for the positive sequence in the three-phase system. This can lead to using the 1^{st} harmonic component of the three-phase system to represent the I_{park} in order to identify the O-C faults in the three-phase inverter. Similarly in single-phase inverter, the 1^{st} harmonic component of the inverter output current I_a can be utilized to identify the faults in the single-phase inverters.

In inverter circuits, there are two different types of O-C faults: (1) Gate-Drive O-C and (2) switching element (IGBT) O-C faults. The main difference between the two cases is the presence of the anti-parallel diode (APD) in the switching element package. This diode allows the output current in the first case to flow in the reverse direction of the switching element conduction. This current path is not available in the latter case, where the entire switching element package is disconnected from the inverter circuit. A single-phase inverter circuit is shown in Figure 3-9.

I_{a1} decreases significantly when there is inverter O-C fault comparing to its value in the normal condition at the same load. Moreover, I_{a1} in switching element O-C fault is significantly reduced from its normal value, and it is also much less than its value at Gate-Drive O-C faults. The sign of the DC offset of the output current, I_{a0} can be used to determine which path of the current is open either the positive current path, i.e. T1 or T4 fault, or the negative current path, i.e. T2 or T3 fault, has been blocked.

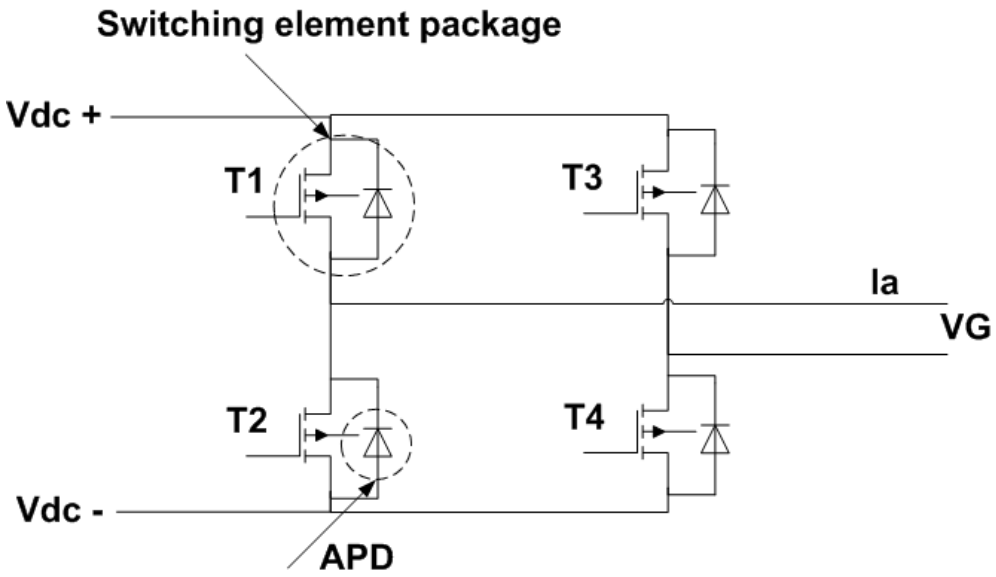


Figure 3-9 Inverter circuit under the study

I_{a1} is normalized to value of the inverter output current at the normal condition I_{an} in order to establish the inverter fault diagnosis independent of the input and load conditions, as well as including the non-ideal conditions in the converter operation. An estimated value for I_{an} can be calculated by the knowledge of the required converter output power $P_{required}$ depending on the measured value of the input frequency, as well as the RMS value of the measured grid voltage V_{Grms}.:

$$I_{an} = \frac{P_{required}}{V_{Grms} * P.F} \tag{3.2.6}$$

where P.F. is the inverter output power factor which is controlled to be equal to one in this system. Therefore a normalized value (I_{a1N}) of I_{a1} can be calculated as follows:

$$I_{a1N} = \frac{I_{a1}}{I_{an}} \tag{3.2.7}$$

Finally, the proposed diagnosis for the inverter O-C faults can be expressed as shown in Figure 3-10 where the threshold values are chosen in order to include these non-ideal conditions in the converter operation.

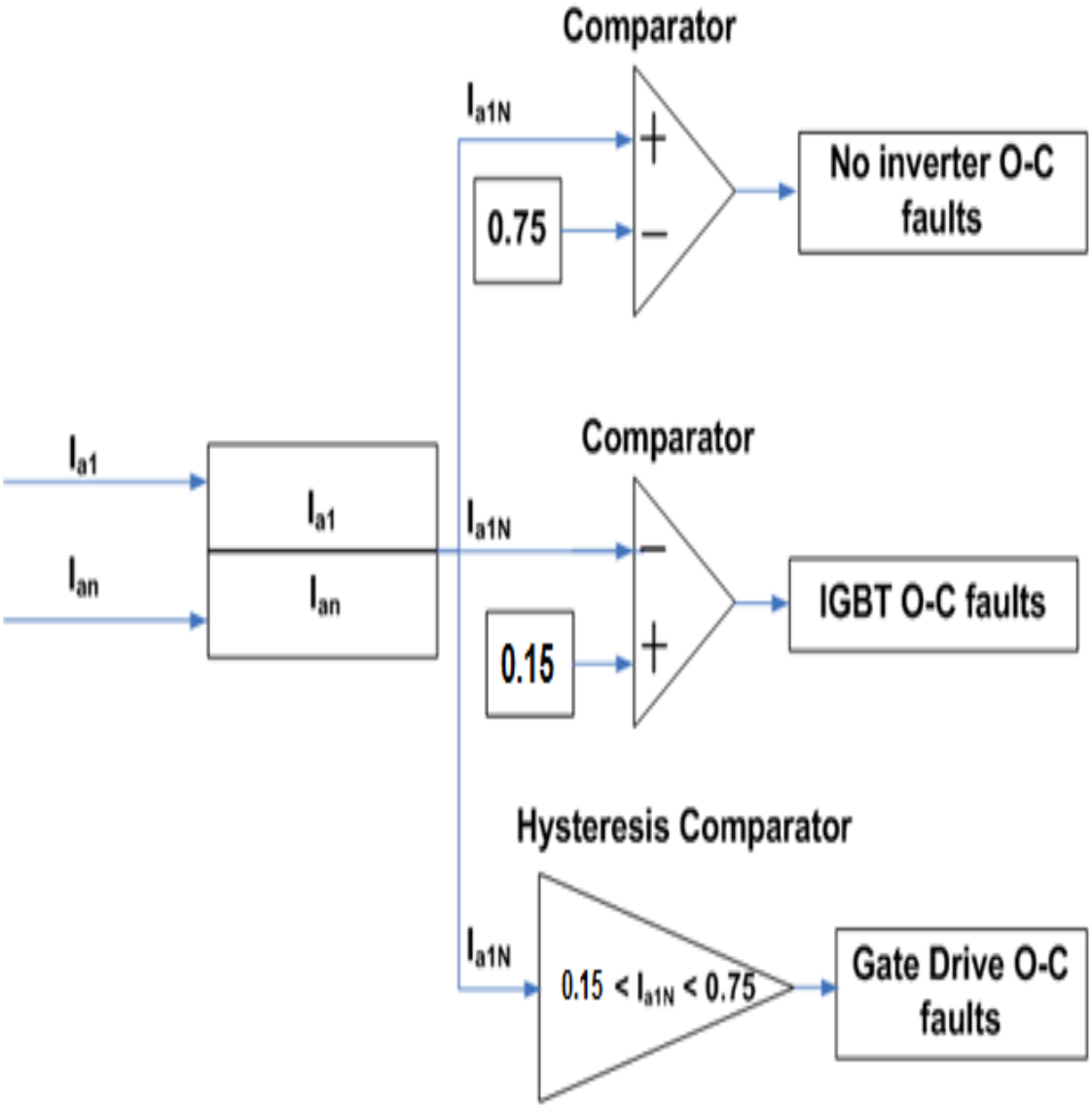


Figure 3-10 Proposed fault diagnosis for Inverter O-C faults

3.2.3. Boost chopper fault diagnosis

The boost chopper circuit under study, as shown in Figure 3-11, is the intermediate stage between the rectifier and inverter circuits. Its function is to control the conduction periods of the IGBT switch T, as well as the diode D to boost the dc voltage. If an O-C fault occurs in switch T, k becomes zero in (2.3.1), so:

$$V_{BAVG} = V_{RAVG} \tag{3.2.8}$$

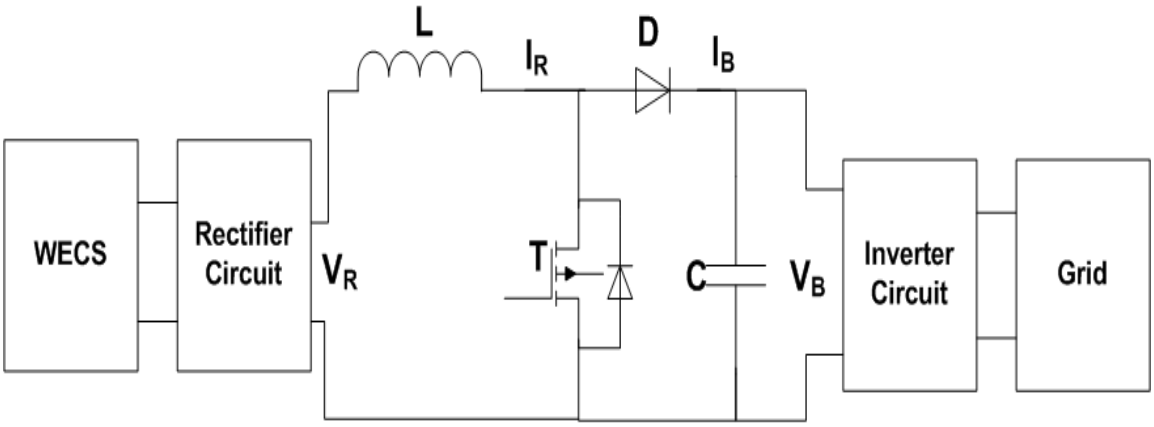


Figure 3-11 Boost chopper circuit within the system under the study

However, V_{BAVG} is controlled in this system to be equal to a desired value $V_{Bdesired}$ by managing the PWM of the inverter circuit. On the other hand, V_{RAVG} is totally dependent on the input rectifier voltage V_S as given in (3.2.8) for a resistive load:

$$V_{RAVG} = \frac{3 * V_{S\max}}{\pi} \tag{3.2.9}$$

At relatively small input power to the converter V_S, it is found that V_{RAVG} becomes less than $V_{Bdesired}$; where, the diode D becomes reverse biased, and V_{RAVG} becomes not different form V_{BAVG}. Such a condition implies that the average values of the output and input currents of the chopper circuit (I_{BAVG} and I_{RAVG} respectively) become zero due to the off condition of the diode D. Therefore:

$$I_{BAVG} = I_{RAVG} = 0 \tag{3.2.10}$$

At relatively high input power to converter, as well as high V_S, V_{RAVG} becomes more than or equal to $V_{Bdesired}$, and the diode D becomes forward biased causing V_{RAVG} equal V_{BAVG}. Thus, due to the on condition of the diode D, I_{BAVG} and I_{RAVG} become equal as follows:

$$I_{BAVG} = I_{RAVG} \neq 0 \tag{3.2.11}$$

In general, if switch T has O-C fault, or in other words k = 0, I_{BAVG} equal to I_{RAVG} regardless of the input power and supply voltage conditions.

$$I_{BR} = I_{RAVG} - I_{BAVG} = 0 \tag{3.2.12}$$

Alternatively, if diode D has O-C fault, there is the possibility of building up the stored magnetic energy in the inductor L during the “on” condition of the switch T. Therefore, there is a certain value for I_{RAVG} greater than zero in this fault case. However,

I_{BAVG} becomes zero due to the detachment of the diode D. So, at the diode D, O-C fault:

$$I_{BAVG} = 0 \; but \; I_{RAVG} \neq 0 \tag{3.2.13}$$

Figure 3-12 illustrates the O-C fault for the boost chopper circuit at the switch T and the diode D respectively, where VDC stands for variable DC supply and NLL stands for nonlinear load. From (3.2.12) and (3.2.13), a fault diagnosis for the boost chopper circuit can be proposed as shown in Figure 3-13, where the threshold values are chosen in order to include non-ideal conditions of the power converter during the normal operation.

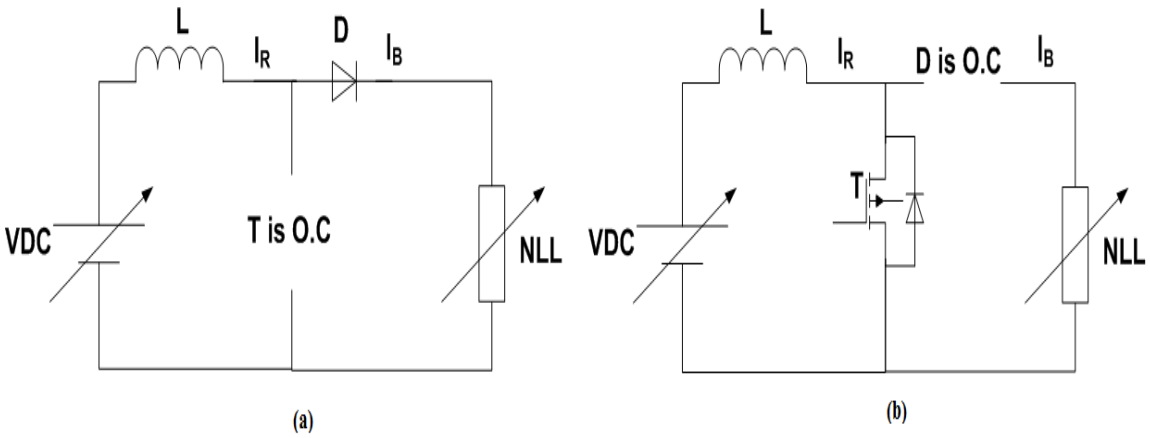


Figure 3-12 O-C fault for the boost chopper circuit at

a) The switch T b) the switch D

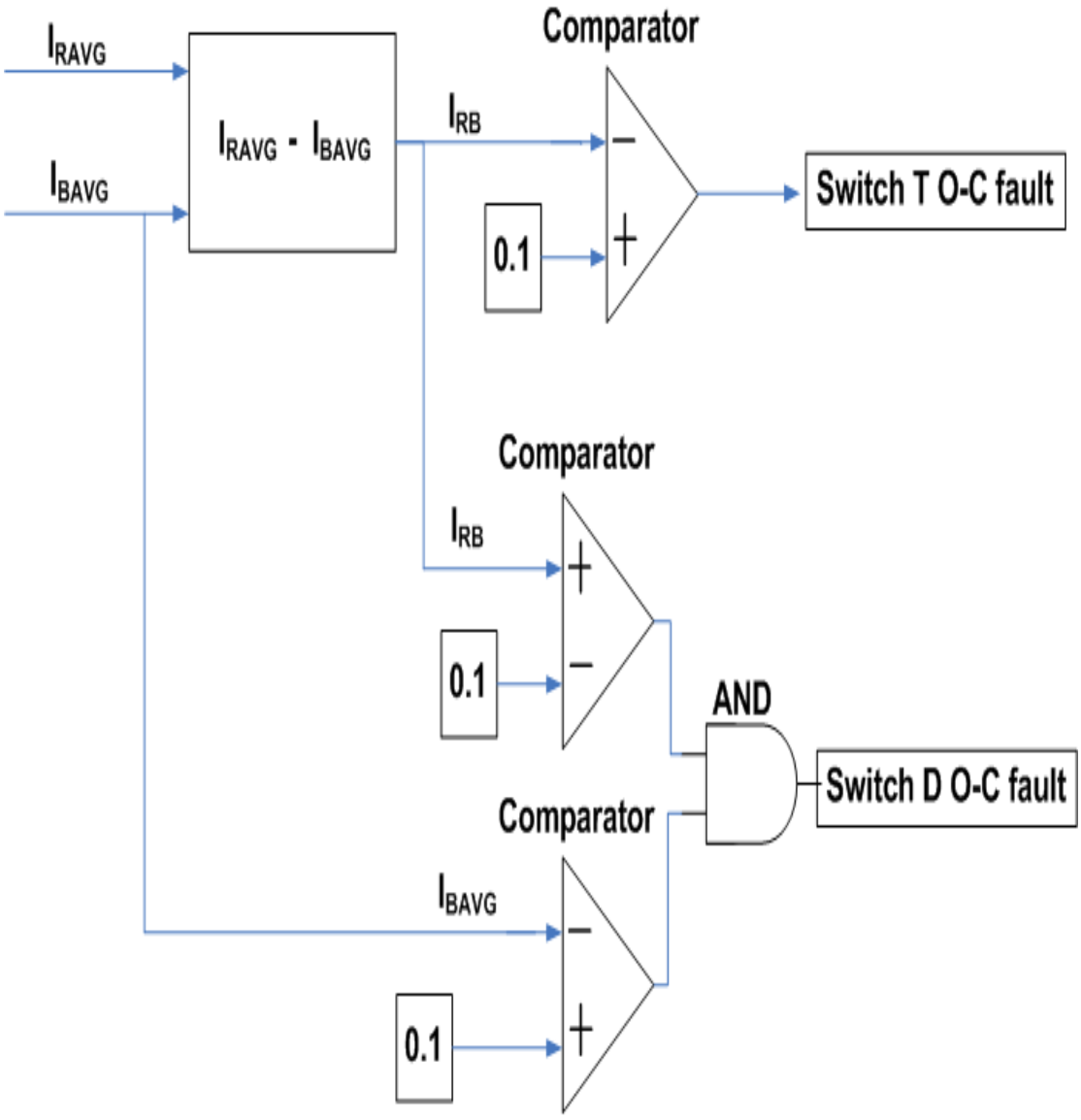


Figure 3-13 Proposed fault diagnosis for boost chopper circuit

Factors Influencing Fault Diagnosis

In this Section, the factors that affect the fault diagnosis in the power converters are presented. This Section also describes how the proposed methodologies overcome these challenges.

3.3 Variations in the input supply voltage

The system under study operates from input frequency 20 Hz to 80 Hz and from input voltage 100 V to 350 V line-to-line RMS value depending on the wind turbine speed. The proposed fault diagnostic algorithms take these variations into consideration by normalizing the threshold criteria used to identify the faults. Accordingly, the proposed diagnostic algorithms provide an accurate determination of fault and normal conditions independent of the input supply situations.

3.3.1. Variations in the output power

The MPPT technique is utilized in the system under study, where the desired output power is a function of the input frequency. The function is implemented as a lookup table stored in the controller of the power converter. This look-up table maps the variations of the output power with the variations of the input condition. Furthermore, the variations of the input conditions are already covered in the proposed fault diagnostic algorithms by normalizing the threshold criteria in the fault diagnosis of the rectifier, inverter, and unbalance input voltage as demonstrated in figures (3-7) and (3-10). Regarding the fault diagnosis of the boost chopper, the variations of the input conditions are considered in detail as provided in (3.2.9) to (3.2.13).

3.3.2. Variations in the system parameters

The non-ideal behavior of the system parameters can be recognized in the internal impedance of the synchronous generator as well as the finite value for the switch resistances during their O-C faults. These parameters can vary depending on the system ratings and its applications. These variations can affect the decision-making process of

the fault diagnostics. Therefore, the threshold criteria in the proposed fault diagnostic algorithms are adjusted as mentioned in subsections 3.2.1 to 3.2.3 in order to include these variations to differentiate the system behavior under normal conditions and under fault conditions.

3.3.4 Measurement errors

Measurement errors are inherent in the measuring sensors, as well as the signal conditioners within the converter. These errors can influence the fault diagnosis results. The proposed algorithms are verified under such conditions.

In the evaluation section, the proposed algorithm for the rectifier fault diagnosis is verified at different input frequencies which are altered with $\pm$ 10% of their value in order to imitate the effect of the measurement errors. It is shown that the proposed algorithm provides accurate decisions even in the presence of such errors.

3.3.5. The effect of the faults on diagnostic algorithms

3.3.5.i. The effect of the rectifier faults

The ripple value of V_R is mainly changed during rectifier faults. This ripple value has a small effect on the average values of I_B and I_R, which are the inputs for the chopper fault diagnosis, so it does not mislead its decision-making process. Similarly, for the inverter fault diagnosis, its input I_a is mostly independent of the ripple value of V_R.

3.3.5.ii. The effect of the inverter faults

During the inverter O-C faults, the value of I_{a1} decreases from its normal value. Although the values of I_{BAVG} and I_{RAVG} are affected by these faults, the chopper fault

diagnosis is not. The fault decisions in the chopper fault diagnosis are made when I_{BAVG} or I_{BR} is equal to zero based on (3.2.12) and (3.2.13). These two conditions are not achieved in inverter faults. Therefore, the chopper fault diagnosis is not affected by these faults. Regarding the rectifier fault diagnosis, the reduction of I_{a1} value results in a slight reduction of the ripple value of V_R. Since the rectifier fault diagnosis detects the fault when this ripple increases to a certain value, it is not influenced by inverter faults.

3.3.5.iii. The effect of the boost chopper faults

During the chopper faults, the variations of I_{BAVG} and I_{RAVG} affect the value of I_a. This could mislead inverter fault diagnosis in its fault detection functions. In the event of an O-C fault in diode D in the chopper circuit, there is no output current I_{BAVG} feeding to the inverter circuit as given in (3.2.13). This leads to zero output current from the inverter, so the first harmonic component of the I_a, as well as its DC value, I_{a0}, become zero which misleads the inverter fault diagnosis. Therefore, in order to avoid misdiagnosis, the chopper fault diagnosis is checked before the inverter diagnosis.

Figure 3-14 provides a flow chart defining the processing cycle for the proposed diagnostic system. It also indicates the inputs of each algorithm, as well as the order of execution of each of the proposed algorithms in order to avoid any false alarms from the proposed methodologies.

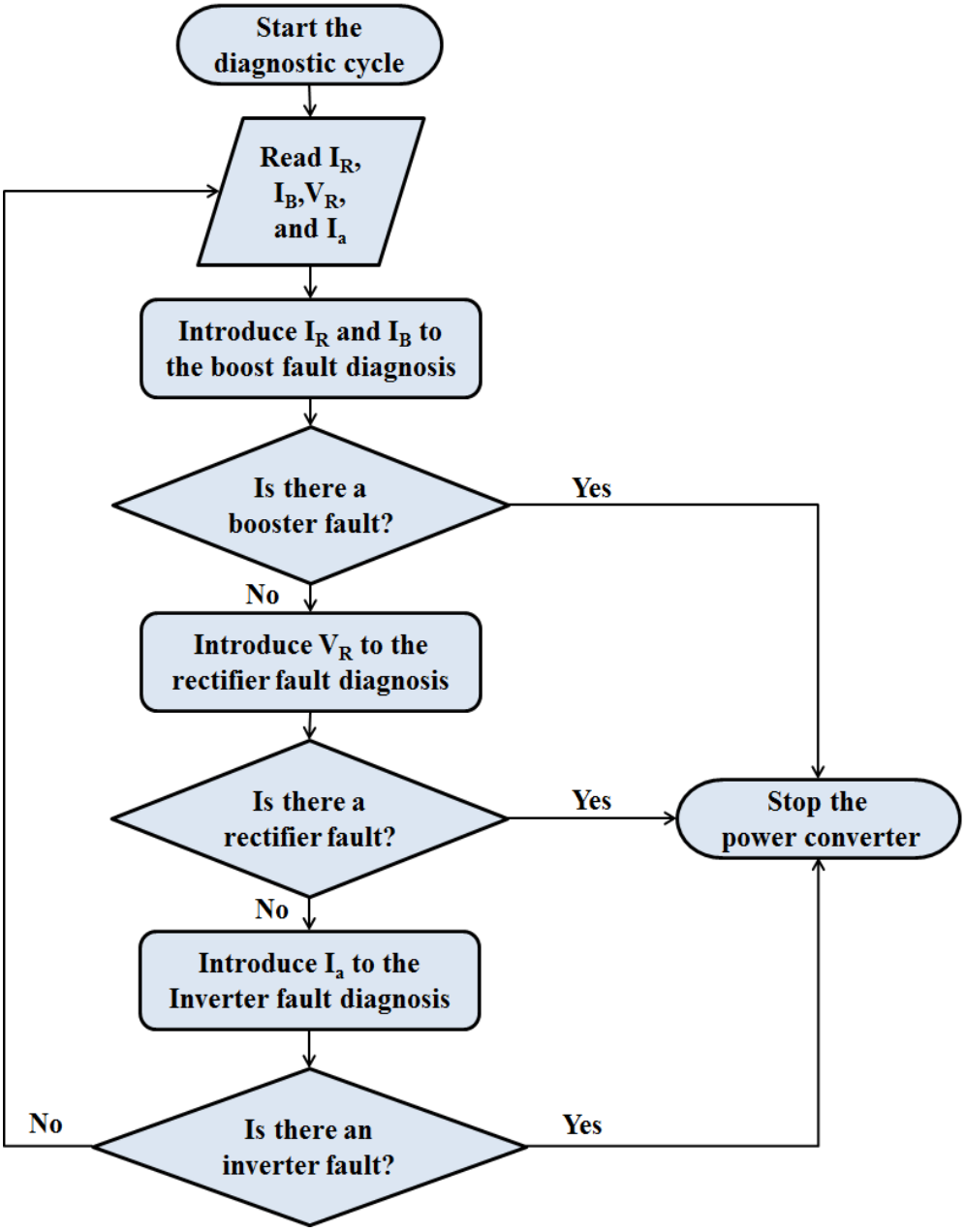


Figure 3-14 Flow chart diagram for the proposed fault diagnoses in power converter

3.4 Comparison between the Proposed and the Previous Fault Diagnostic Algorithms

Table 3-3 provides a comparison between the earlier fault diagnosis research methods and the proposed fault diagnosis in this dissertation. The table states the required inputs for each fault diagnosis method as well as its fault detection time. It is shown that from Table 3-3 the earlier methods require either the measurements of the three-phase currents or voltages as well as additional sensor and hardware which are not available in the typical commercial power converters connected to small wind turbines. These additional hardware and sensors include additional costs and expenses which are critical for such commercial systems. However, the proposed fault diagnostic algorithms in this dissertation for rectifier O-C faults as well as the unbalance input voltages require solely the measurement of the output DC-link voltage V_R in order to identify the fault in both faulty cases, where the minimization of the required sensors and hardware is very significant especially for the low or medium-size commercial power converters.

On the other hand, some of the earlier methods provide fault detection methods whose detection time is less than that in the proposed fault diagnoses in this dissertation. However, this advantageous gain requires additional hardware or/and sensors which leads to increase the system cost and complexity as mentioned previously. Moreover, the time difference between the fault detection time in the former and proposed fault diagnoses are not critical for the O-C faults where the produced voltages and currents during these faults are not as high as those in S-C faults but rather their values are relatively close to their values at normal conditions but in distorted patterns as demonstrated in Section 3-2.

Table 3-3 Comparison between the former and proposed fault diagnostic methods

Fault Detection Method	Required Inputs for the Detection Method	Fault Detection time
Park Vector Method [6-8],[18-19]	Measurements of three-phase currents	Around one fundamental period
Enhanced Park Vector Method [4]	Measurements of three-phase currents	20-50% of the fundamental period
Sliding Mode Observer (SMO) [9]	Measurements of arm currents and voltages	Several fundamental period
Model Reference Adaptive System (MRAS) [20]	Measurements of three-phase currents	5% of the fundamental period
Comparing the voltages measurements to their respective references [21]	Measurements of three-phase voltages	Around one fundamental period
Discrete Wavelet Transform Approach [22]	Measurements of three-phase currents	Around one fundamental period
Gate-Voltage Behavior Method [23]	Measurements of the gate drive voltages of all IGBT	Micro seconds
Voltage Based Approach [24]	Measurements of three-phase currents and the DC-link voltage	5-65% of the fundamental period
Switching-state estimation algorithm [25]	Measurements of three-phase input currents as well as the output currents	Around one fundamental period
Current-Based Approach [26]	Additional current sensors are required in particular positions in the converter	Micro seconds
Comparing the current measurements to their respective references [27]	Measurements of three-phase currents	5% of the fundamental period
Proposed Fault Diagnosis for rectifier O-C faults and unbalance input voltage	Measurements of the DC-link output voltage	Around one fundamental period

Other research works presented in [28-29] use the principal component analysis (PCA) and S-transform, as well as the Support Vector Machines (SVM) to detect the faults in the three-phase rectifiers. The input to the decision-making unit is the output voltage of the rectifier. The proposed method detects the faults taking place solely in one switch either short or open circuited. The procedure extracts the features corresponding to various faults using either PCA or S-transform. Then, the fault types are identified through 13 SVM classifiers corresponding to the 12 fault conditions and the normal state. Beside the complexity of the methodology presented in [28-29] and the requirement to establish an entire classifier for each fault condition, the method is used to analyze only one fault class of the all-possible seven fault classes, which are fully investigated in the proposed fault diagnosis methodology in this thesis research. The proposed methodology identifies a total of 129 open circuit fault conditions with the normal state including in all seven fault classes mentioned in Table 3-2.

Finally, research presented in [30] uses the output rectifier voltage to detect the faults in the rectifier circuit. The output rectifier voltage is compared to a reference signal in order to obtain the residual error, which is utilized to diagnose the switch failure. The adopted reference voltage signal in [30] is evaluated by measuring the three phase input voltages, so its methodology requires the measurements of the input and output voltages in order to detect the fault. On the contrast, the proposed diagnostics in this research requires only the rectifier output voltage to identify the faults.

For the single-phase inverters, research [31] uses a magnetic field probe in order to detect the magnetic field near the output inductor of the single-phase inverter. The measured waveform is processed by the peak detector and comparators and is utilized as

the diagnostic criterion for the inverter faults. Furthermore, fault diagnosis based on D-S evidential theory and fuzzy logical theory is presented in [32] for fault diagnosis of the single-phase inverter. The inputs to the diagnosis module are the output voltage, the input voltage and the temperature of MOSFET. However, the proposed fault diagnosis methodology for the single-phase inverter in this research is based solely on the measurement of the output inverter current, so there is no need to add more sensors as employed in the previous two researches.

Finally for the DC-DC converters, Research [33-35] requires an additional auxiliary winding in order to measure the magnetic component of the voltage which is used in diagnostic criterion for the O-C faults in the DC-DC circuits. However, the proposed DC-DC fault diagnosis in this research does not require any additional hardware or/and sensors for the fault detection of O-C faults in the boost chopper circuit. The proposed fault diagnostic algorithm requires only the input and the output currents in order to identify the O-C faults.

Moreover, Fault detection in the DC-DC converters is provided in [36-37] depending on the determination of the sign variations of the slope of the current of the converter. However, the provided algorithms are subjected to non-ideal behavior of the power switches, as it is very sensitive to the delays and dead times of the switching process which could lead to either false alarm or un-fault detections.

On the other hand, the proposed fault diagnostic algorithm for the DC-DC converter in this research is more generalized as well as more reliable and robust as it depends on the average values of the currents of the DC-DC converter which are less influenced by the fast transients and noise than the sign variations of their slope.

3.5 Fault Diagnosis Evaluation in the Simulation Environment

The proposed fault diagnostic methodologies are investigated and verified in MATLAB/Simulink environment, where the power converter under study is modeled with its three main circuits: rectifier, boost chopper, and inverter circuits. However the WECS is replaced with a variable three-phase voltage to model the VVVF behavior of the WECS.

3.5.1. Rectifier fault diagnosis evaluation

Figure 3-15 presents simulated results for balanced and 10% unbalanced input voltage at several input frequencies. The proposed algorithm is tested at 20, 40, 60, and 80 Hz for both balanced and unbalanced conditions. Figure 3-15 shows simulated results for the fault detection in the rectifier circuit at different classes of O-C faults whose indices are provided in Table 3-2. In both figures, V_{R2N} is used to identify either the unbalanced or rectifier fault conditions by threshold line 1% based on Figure 3-7.

In Figure 3-16, $\pm$10% variations in the input frequency are included in simulation to represent the measurement errors in order to evaluate the proposed diagnostic algorithm under these conditions.

It is shown that the proposed algorithm provides a correct decision for the rectifier and unbalanced fault conditions under variety of situations of normal and fault conditions.

A log-scale for Y-axis is chosen for Figure 3-16 in order to clearly indicate the range of the variation of V_{R2N} % value during the normal and fault conditions in one plot. V_{R2N} % is less than 1% at normal conditions. However, it becomes around 10% to 50% in the fault conditions.

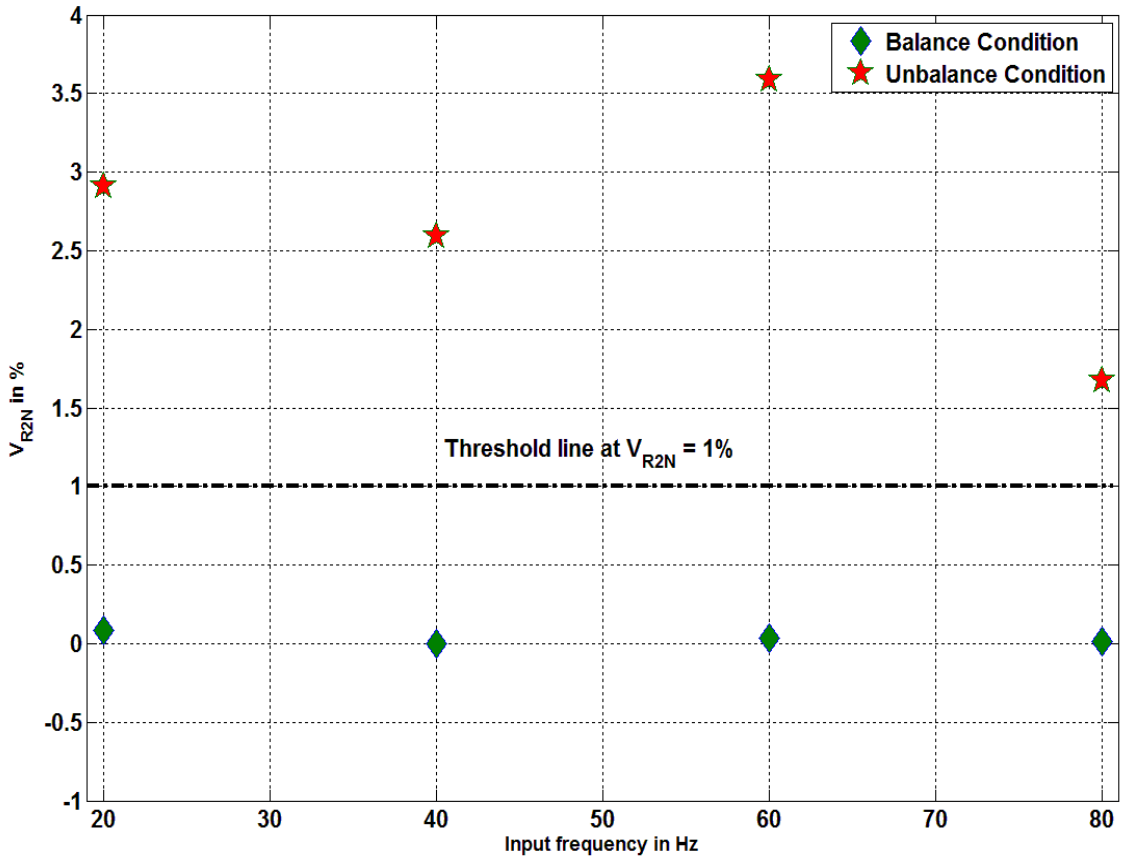


Figure 3-15 Simulated results for the proposed unbalance fault diagnosis

3.5.1. Inverter fault diagnosis evaluation

Figure 3-17 provides simulated results for the proposed inverter fault diagnosis based on Figure 3-10 at different supply and loading conditions. Threshold Line 2 is used to differentiate between the fault and normal conditions, while threshold Line 1 is used to classify the fault type either IGBT O-C fault or gate drive O-C fault. On the other hand, threshold Lines 3 and 4 are used to determine the blocked current path during the fault. It is shown that the proposed technique presents an accurate fault detection and classification for the inverter O-C faults.

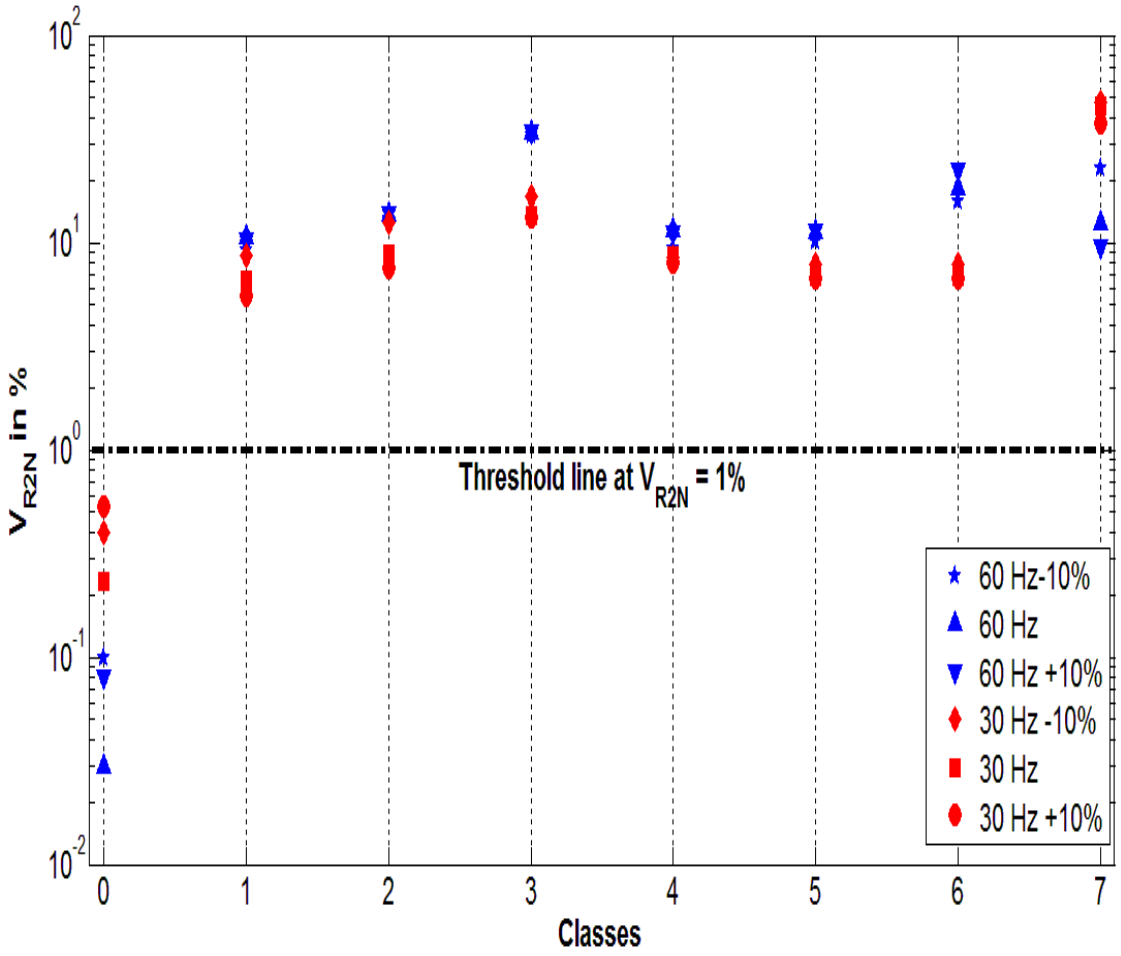


Figure 3-16 Simulated results for the proposed rectifier O-C fault diagnosis

3.5.1. Boost chopper fault diagnosis evaluation

Figure 3-18 presents simulated results for the fault detection and classification in the boost chopper circuit dependent on the fault diagnosis scheme in Figure 3-13. It is shown that the proposed technique establishes a robust diagnostic algorithm for the O-C faults in the boost chopper circuit.

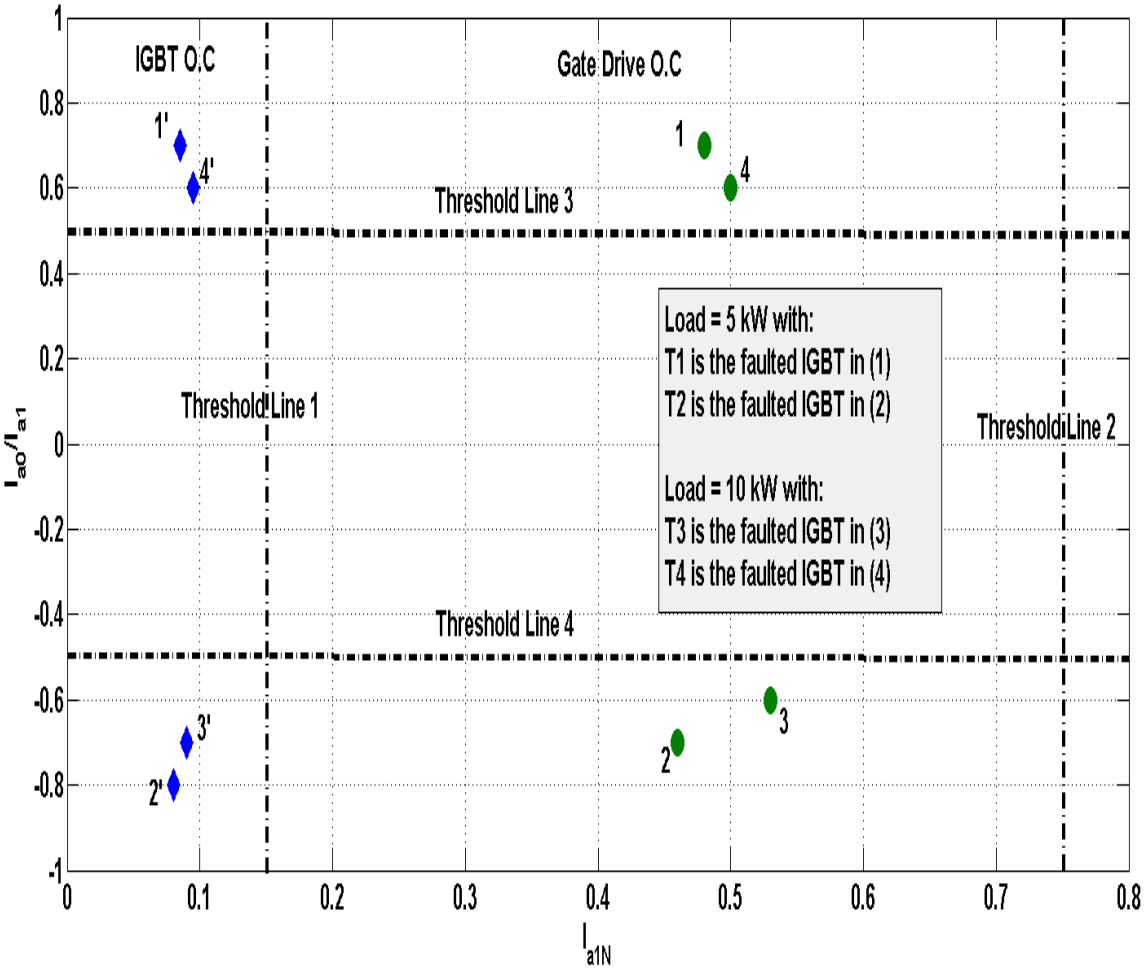


Figure 3-17 Simulated results for the inverter fault diagnosis

3.6 Summary

This chapter has provided fault detection, classification and localization for the three main circuits of the grid-connected power converter, as well as the detection of the unbalanced input voltage to the converter by using fewer inputs than those used in previous research.

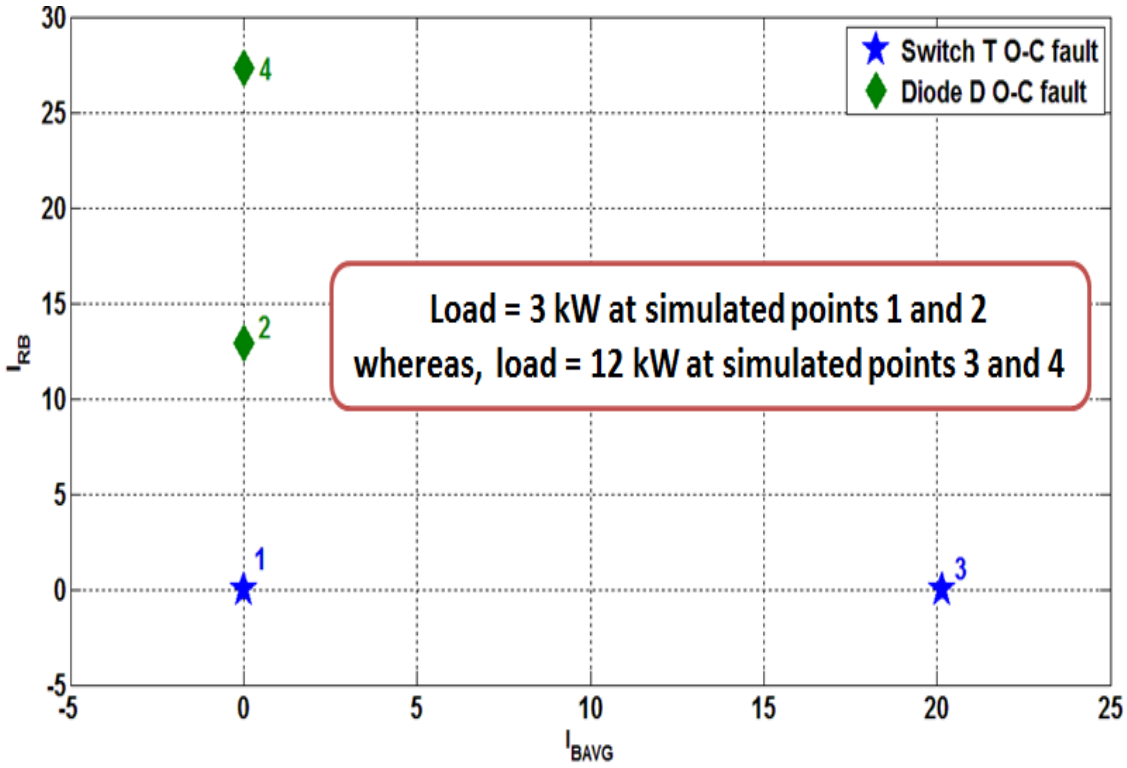


Figure 3-18 Simulated results for the boost chopper fault diagnosis

These inputs depend on the available number of measuring sensors in the system under study. The proposed algorithms have been implemented by utilizing the relationship between the sequence components of the electrical signals with their harmonic components.

The minimization of the required sensors and hardware is important in reducing the system expenses. Therefore, it becomes very significant particularly for small and medium-size commercial power converters implemented in distributed generation systems. The ability of the proposed fault diagnostic algorithms to identify faults has been verified at different normal and fault conditions in simulation environment under several supplying and loading situations.

Chapter 4: Fault Diagnoses in Experimental Environment

4.1 Preface

This chapter provides the experimental implementation and validation of the proposed fault diagnoses of the power converter system under study. The proposed algorithms are implemented in the digital signal processor (DSP) TMS320LF2407 of the power converter system. The objective of this stage is to provide a real-time detection, classification, and localization of O-C faults of the power switching elements in the power converter. Moreover, the proposed diagnostic methodologies are modified and simplified in the experimental environment in order to achieve the required diagnostic tasks without disturbing or interfering with the controlling processes of the converter implemented in the DSP of the converter.

Fast Fourier Transform (FFT) is used as the main signal processing algorithm for the inputs of the most of the proposed fault diagnosis in this research as described in Chapter 2. However, the FFT function used in the MATLAB program is more powerful than the FFT subroutine that is implemented in the DSP of the converter. The length of the input buffer for the FFT function in MATLAB is variable which can be chosen to be exactly equal to the period of the input signal. On the other hand, the input buffer to the FFT subroutine in the DSP of the converter has fixed length (512) regardless of the period of the input signal, and as a result, some errors are introduced on the estimated output features of the FFT of the DSP. Therefore, the proposed diagnostic algorithms are adjusted in the experimental implementation of the diagnostic algorithms in order to overcome the drawbacks of the FFT subroutine in the converter DSP.

Section 4.2 introduces the implementation of the FFT algorithm in the converter DSP. The modified fault diagnostic methodologies are developed in Section 4.3. Section 4.4 provides the evaluation of the fault diagnoses methodologies in the experimental environment. Finally, the summary of the proposed diagnostic algorithms of this chapter is given in Section 4.5.

4.2 Implementation of the FFT algorithm in the converter DSP

The Fast Fourier Transform (FFT) algorithm is used as the main signal-processing tool for the input signals for the fault diagnoses that are implemented in this research. The utilized FFT algorithm in the converter DSP has a fixed point of 512 buffer length for its input and output buffers.

The sampling frequency f_s in the present research is 10 kHz. As a result, the available time range for the input signal to the FFT algorithm in DSP is T_1 where;

$$T_1 = Buffer\ \ length * T_s = 512 * \frac{1}{fs} = \frac{512}{10000} = 51.2\ ms \tag{4.2.1}$$

where, T_s is the sampling time. Consequently the corresponding fundamental frequency f_1 for the input signal becomes:

$$f_1 = \frac{Sampling\ \ frequency}{Buffer\ \ length} = \frac{10000}{512} = 19.53\ Hz \approx 20\ Hz \tag{4.2.2}$$

On the other hand, the range of the supply input frequency for the power converter under study is from 20 to 80 Hz depending on the wind speeds.

In order to achieve more accurate results from the FFT algorithm in the DSP, more than one period of the supply signal should be introduced to the FFT buffer. As a result, the sampling frequency is alternated dependent on the supply input frequency so that more than one period of the supply signal can be provided to the input buffer of the FFT algorithm at all supply frequency range. Table 4-1 indicates such variation in the sampling frequency according to the supply input frequency and it also provides the range of the number of periods of the input signal at each case.

For instance, in the case of the input frequency ranges from 20 Hz to 25 Hz, the sampling frequency is selected to be $f_s/3 \approx 3.33$ kHz. As a consequence, f_1 becomes equal to $3333/512 \approx 6.5$ Hz in such condition. Therefore, the number of the periods becomes varied form (20/6.5 = 3.5) to (25/6.5 =3.8) dependent on the supply input frequency as given in the last row of Table 4-1.

Table 4-1 Relationship between the input frequency and the sampling frequency

Input Frequency	20 → 25 Hz	26 → 45 Hz	46→ 80 Hz
Sampling Frequency	$f_s/3$	$f_s/2$	f_s
Fundamental frequency for FFT	6.5 Hz	9.7 Hz	19.5 Hz
Number of the input periods of the signal to the FFT algorithm	3 → 3.8	2.7 → 4.6	2.3→ 4

4.3 Fault Diagnoses Methodologies

The modified diagnostic methodologies for the faults in the power converter are provided in the following subsections.

4.3.1. Diagnosis methodology for the rectifier O-C faults

The ripple of the output rectifier voltage V_R is used to detect the rectifier Open Circuit faults in this research. These ripples are undergoing an amplification process in order to have more precise results in the proposed diagnosis. The amplification process consists of two steps. The first step is the use of the band pass filter from 10 to 600 Hz with gain 15 as presented in Figure 4-1. The band pass filter is also implemented in order to eliminate the DC component of V_R as well as its high frequency noises in order to achieve more accurate results from the FFT algorithm in DSP. The second step includes a software subroutine where the gain is varying, so that the ripple can magnify to the maximum limit allowable by the DSP data memory size.

The output voltage of a three-phase rectifier in the normal condition with the filtering capacitor is shown in Figure 4-2. There are six peaks in the V_R waveform over one complete period of the input three-phase supply during the normal conditions.

These six peaks are caused by the conduction of the six diodes of the rectifier in a sequential manner. Consequently, if one diode is open-circuited in the 3-phase rectifier circuit, a distorted pattern is produced in the V_R waveform due to the missing of one peak of the six peaks in the V_R waveform over one complete period. Furthermore, this distorted pattern is repeated with a frequency equal to the input voltage frequency f_o, which is inverse of the input time period T_o, as presented in Figure 4-3. Therefore, this distorted pattern repeated once every one complete T_o period.

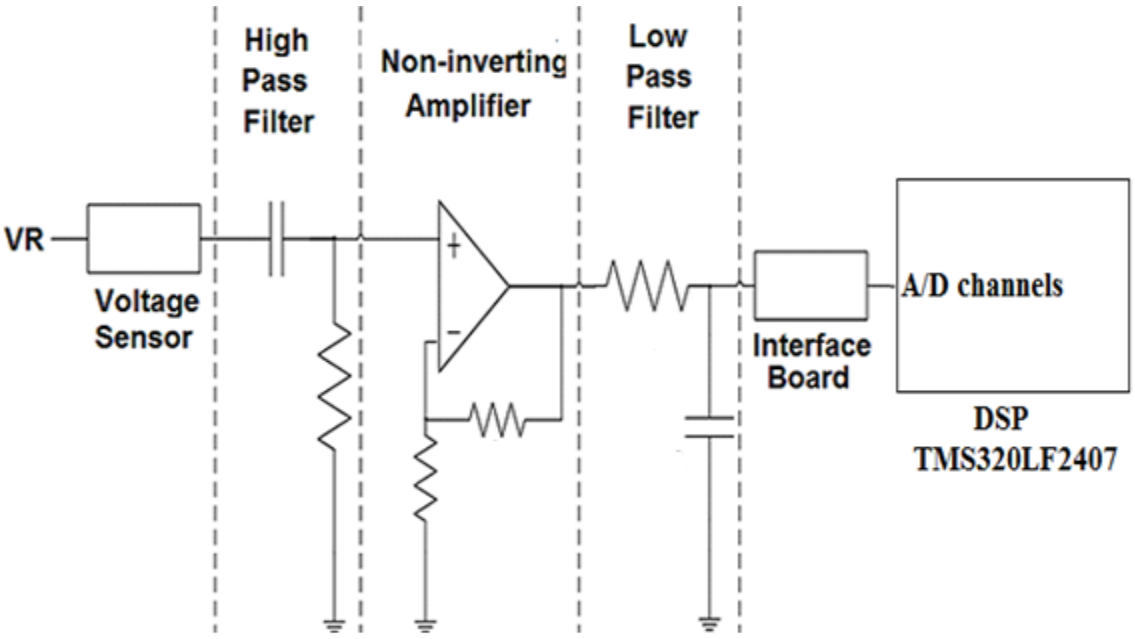


Figure 4-1 Band pass filter

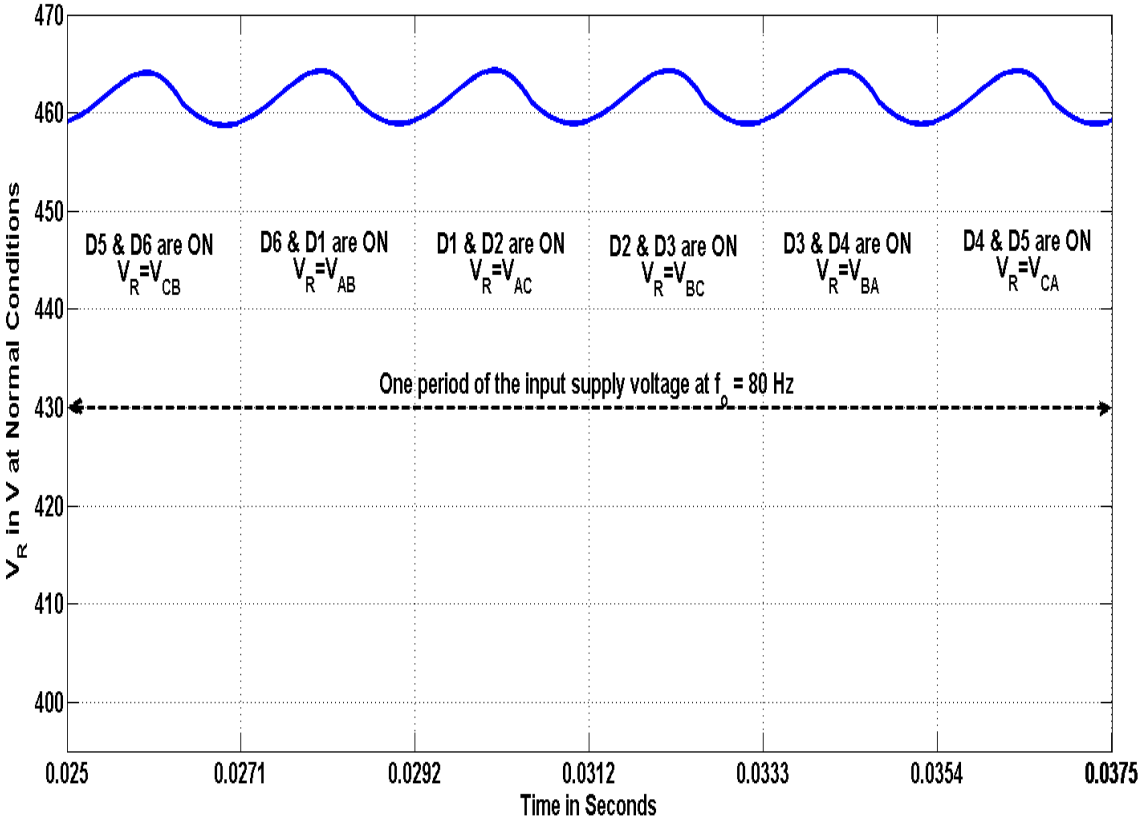


Figure 4-2 Rectifier output voltage at normal conditions

The Fourier series expansion of the rectifier output voltage with one diode open circuited can be deduced, as given in Appendix A, as follows:

$$V_R\big|_{One\ diode O\text{-}C}(t) = \frac{5\,V_{S\,MAX}}{2\,\pi} + \sum_{k=1}^{\infty} A_k \cos\left(\boldsymbol{k}\omega_o t + \theta_k\right) \qquad (4.3.1)$$

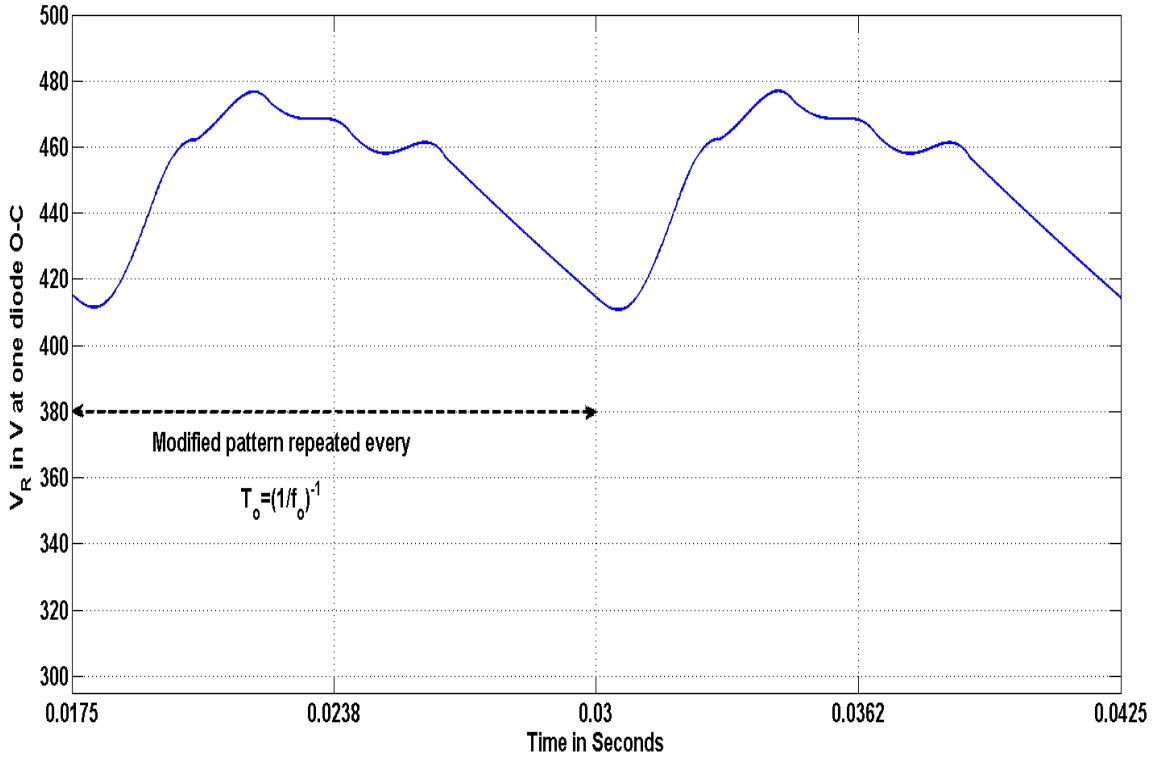
where Θ_k depends on the fault time and

$$A_k = \frac{V_{S\,MAX}}{2\sqrt{3}}, \qquad \text{for k=1} \qquad (4.3.2)$$

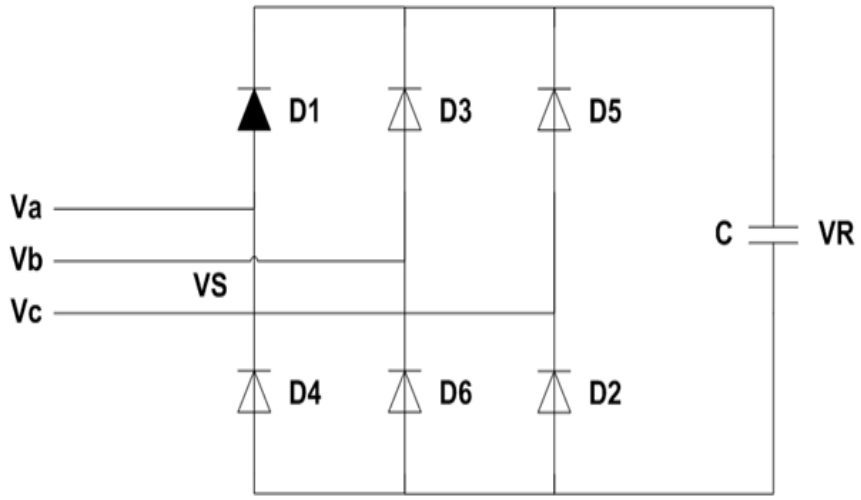
$$A_k = \frac{V_{S\,MAX}\left(1+2\cos\left(\pi k/3\right)\right)}{\pi\,(k^2\text{-}1)}, \text{ for k= 3,5,7,..} \qquad (4.3.3)$$

$$A_k = \frac{V_{S\,MAX}\left(3+2\cos\left(\pi k/3\right)\right)}{\pi\,(k^2\text{-}1)}, \text{ for k= 2,4,6,..} \qquad (4.3.4)$$

From Figure 4-3, it is demonstrated that the 1st harmonic component V_{R1} is the main component in the V_R during this fault type and it is verified in (4.3.1) in bold as well.



(a)



(b)

Figure 4-3 D1 O-C fault at f_o = 80 Hz

a) V_R waveform b) Rectifier circuit with faulted diode

On the other hand, if two diodes are open-circuited in the same branch, the distorted pattern is produced due to the missing of two peaks in the V_R waveform over one complete period, and the time between these two peaks will be half the period of the input three-phase supply. Therefore, this distorted pattern is repeated twice every one complete T_o period. This leads to having the distorted pattern repeated with frequency double of the f_o, as presented in Figure 4-4.

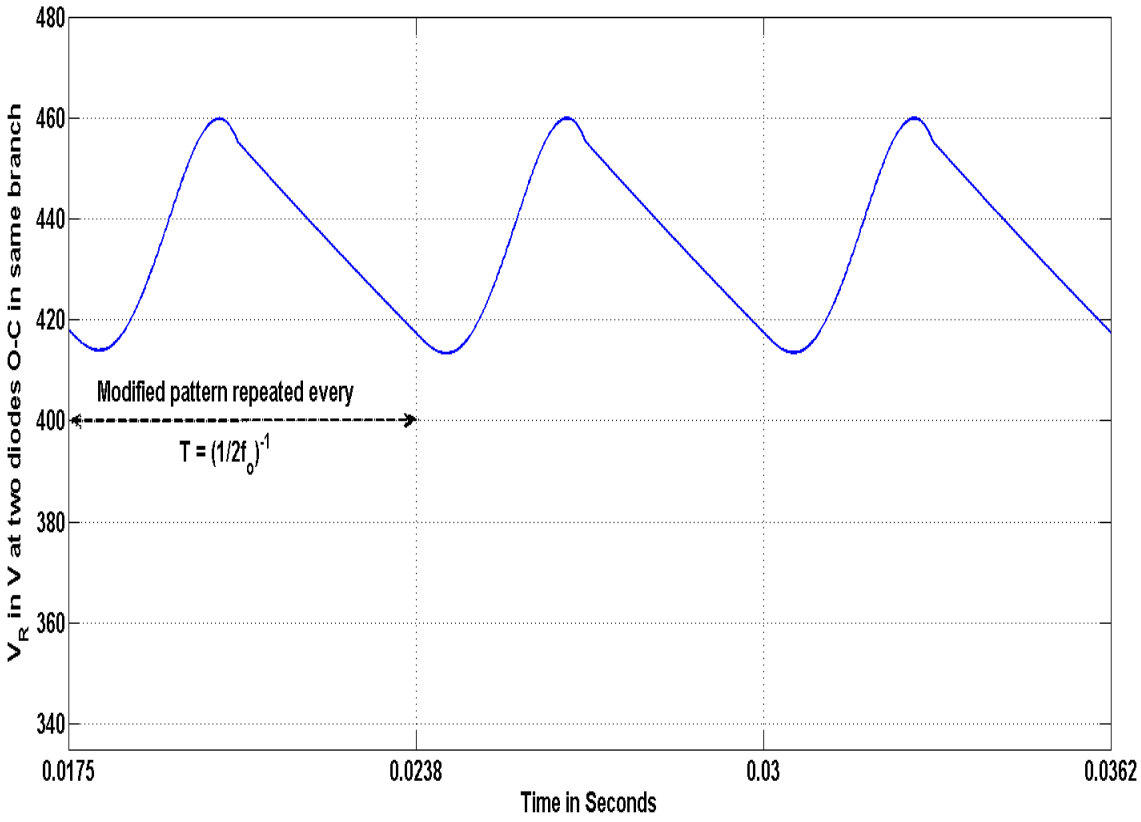
The Fourier series expansion of the rectifier output voltage at two diode open circuited in same branch can be calculated, as given in Appendix A, as follows:

$$V_R\big|_{Two\ diodesO\text{-}C}(t) = \frac{V_{S\,MAX}}{\pi} + \sum_{k=1}^{\infty} A_k \cos\left(2\boldsymbol{k}\omega_o t + \theta_k\right) \qquad (4.3.5)$$

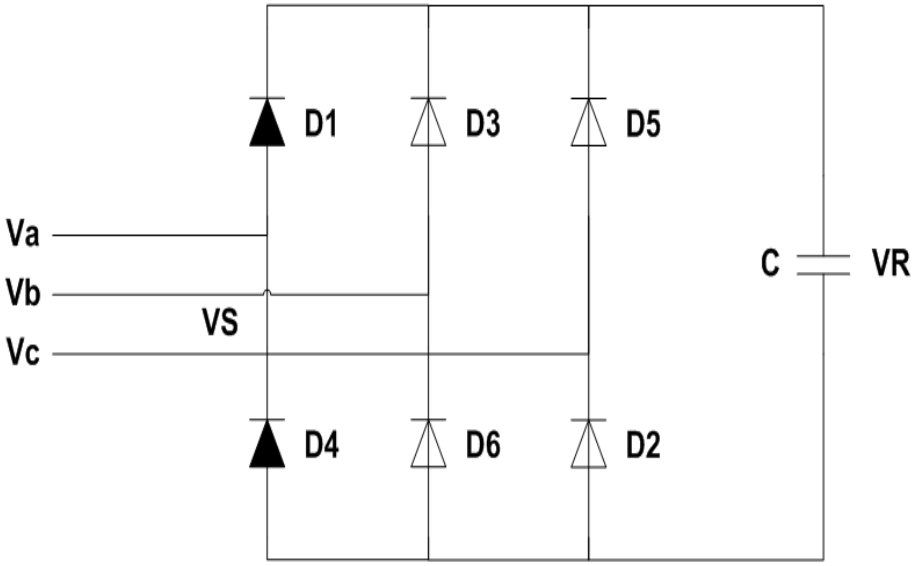
Where Θ_k depends on the fault time and

$$A_k = \frac{V_{S\,MAX}}{\pi\left(4k^2\text{-}1\right)} \qquad (4.3.6)$$

From Figure 4-4, it is demonstrated that the 2nd harmonic component V_{R2} is the main component in the V_R during this fault type and it is verified in (4.3.5) in bold as well.



(a)



(b)

Figure 4-4 D1 and D4 O-C fault at f_o = 80 Hz

a) V_R waveform b) Rectifier circuit with faulted diodes

By continuing the circuit analysis and examination of the V_R for the remainder of the O-C fault classes in the rectifier circuit, it is found that the main harmonic component will be a combination of the V_{R1} and V_{R2}. Therefore, the summation of V_{R1} and V_{R2} can be used to identify the rectifier O-C faults. However, for the last fault class C7 in Table 3-2, the average value V_{Ravg} of V_R goes to zero due to the total detachments between the output and the input of the rectifier circuit because of the three O-C faulted diodes either in the upper arms or lower arms. Therefore, this criterion is used to identify this fault class.

The FFT algorithm is implemented in the DSP in order to calculate the 1^{st} and the 2^{nd} harmonic components of V_R, where the indices of the FFT output buffer, which indicate the 1^{st} and the 2^{nd} harmonic components, vary depending on the number of the input periods of the input signal to the FFT algorithm.

Table 4-2 represents the indices of the FFT buffer that indicate the 1^{st} and the 2^{nd} harmonic components depending on the input frequency. Therefore, the spectra of the V_R over its 1^{st} and 2^{nd} harmonic are evaluated, so that it can be used to detect the rectifier O-C faults.

In order to calculate this spectrum, a summation process is applied to the FFT output indices representing 1^{st} and 2^{nd} harmonic components. However, these indices vary according to the input frequencies. Therefore, in order to develop a general rectifier fault diagnosis algorithm independent of the input frequencies, the required spectrum is evaluated over all the possible indices, which represent the desired harmonics according to Table 4-2. Therefore, the summation is carried out between the minimum and the maximum limits of the indices regardless of the input frequency. These limits are 2 and

10 respectively as provided in Table 4-2. So, the required spectrum, $Spect_1$, is evaluated as follows:

$$Spect_1 = \sum_{k=2}^{10} FFT_{output}(k) \tag{4.3.7}$$

Table 4-2 Relationship between the FFT output indices and the harmonic components

Input Frequency	20 → 25 Hz	26 → 45 Hz	46→ 80 Hz
Number of the input periods of the signal to the FFT algorithm	3 → 3.8	2.7 → 4.6	2.3→ 4
1st harmonic component of the input signal will be located at FFT index number	3 → 4	3 → 5	2 → 4
2nd harmonic component of the input signal will be located at FFT index number	6 → 8	6→ 10	4→ 8

Furthermore, the effect of the amplification process is eliminated by dividing $Spect_1$ by the square of the gains of the band pass filter G_{HW} and software subroutine G_{SW}. It is

divided by the square values due to the FFT output being implicitly squared in the FFT algorithm of the DSP program. Finally, a normalization process is implemented for $Spect_1$ in order to make the rectifier fault diagnosis algorithm independent of the input voltage amplitude. So, the variable $Spect_1$ is divided by the RMS value of the input voltage of the rectifier V_S and then multiplied by 100 to have the final value in percentage as follows:

$$Spect_{norm1} = \frac{Spect_1}{V_{S\,rms} * (G_{HW} * G_{SW})^2} * 100\% \qquad (4.3.8)$$

4.3.2. Diagnosis methodology for the input voltage unbalance

Subsection 3.2.1 in the previous chapter demonstrates that the 2nd harmonic components V_{R2} of V_R could be utilized in order to identify the unbalanced condition in the input voltage, where V_{R2} is greater than zero at the unbalanced conditions. However, the value of the V_{R2} is small in comparison with the RMS value of the input voltage to the rectifier V_S in the experimental environment. Therefore, the amplification process is considered in the experimental diagnosis in order to amplify the value of V_{R2} so that the unbalanced conditions could be recognized and detected using a normalized criterion with respect to the V_{Srms}. Therefore, the spectrum $Spect_2$, representing the 2nd harmonic component of the V_R is calculated based on Table 4-2 as follows:

$$Spect_2 = \sum_{k=4}^{10} FFT_{output}(k) \tag{4.3.9}$$

where $Spect_2$ is evaluated by a summation process over all the indices representing the 2^{nd} harmonic component of the V_R regardless of the input frequency f_o.

The variable $Spect_2$ in this diagnosis is not divided by the square value of G_{HW} in order to amplify the effect of the unbalance condition. However, $Spect_2$ is still divided by the square value of G_{SW} which is totally dependent on the V_R ripple value but G_{HW} is fixed regardless of the V_R ripple. Finally, the threshold criterion $Spect_{norm2}$ for the unbalance input diagnosis is generalized and normalized as follows:

$$Spect_{norm2} = \frac{Spect_2}{V_{S\,rms} * G_{SW}{}^2} * 100\% \tag{4.3.10}$$

4.3.3. Diagnosis methodology for the boost chopper O-C faults

Subsection 3.2.3 provides the diagnostic algorithm to identify the O-C faults in the boost chopper circuit based on (3.2.11) and (3.2.12). This algorithm is also adopted here in the experimental environment with little modification in order to take into account the slight difference between the gains of the current sensors measuring the input and output currents of the chopper circuit. This difference affects the proposed algorithm in the subsection 3.2.3, so it is modified in the experimental environment and is provided in detail in the evaluation section of this chapter.

4.3.4. Diagnosis methodology for the inverter O-C faults

The waveform of the output current I_a of the single-phase inverter (Figure 4-5) has a regular sinusoidal AC pattern at the normal conditions as shown in Figure 4-6. However, for the T1 or T4 O-C faults, the positive halves of this sinusoidal waveform are eliminated because the positive path of the current I_a is blocked due to the fault. On the other hand, at the T2 or T3 O-C faults, the negative halves of the sinusoidal waveform of I_a vanish because the negative path of the current is blocked due to the fault. Figure 4-7 and Figure 4-8 present the I_a waveforms during the T1 and T2 O-C faults respectively.

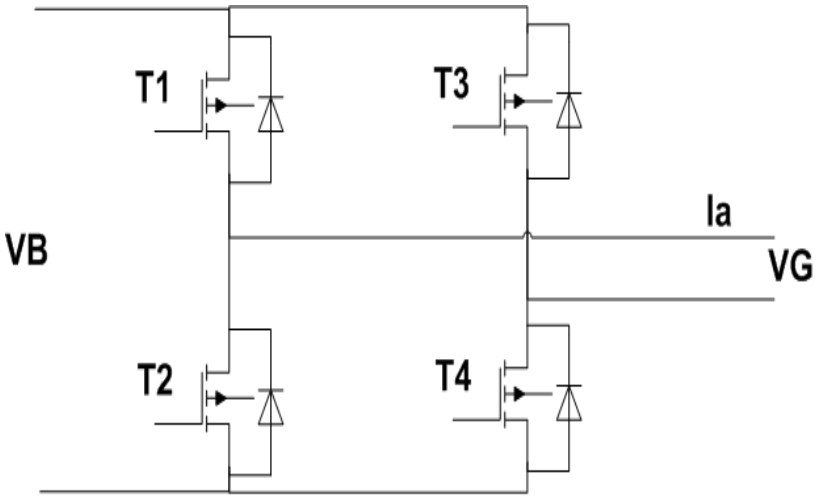


Figure 4-5 Single-phase inverter under the study

Therefore, the average value I_{aAVG} of I_a can be used to identify the O-C faults in the inverter circuit, where I_{aAVG} is calculated as follows:

$$I_{aAVG} = \frac{1}{2\pi}\int_{0}^{2\pi} I_{aMax} \sin\varphi \; d\varphi \qquad (4.3.11)$$

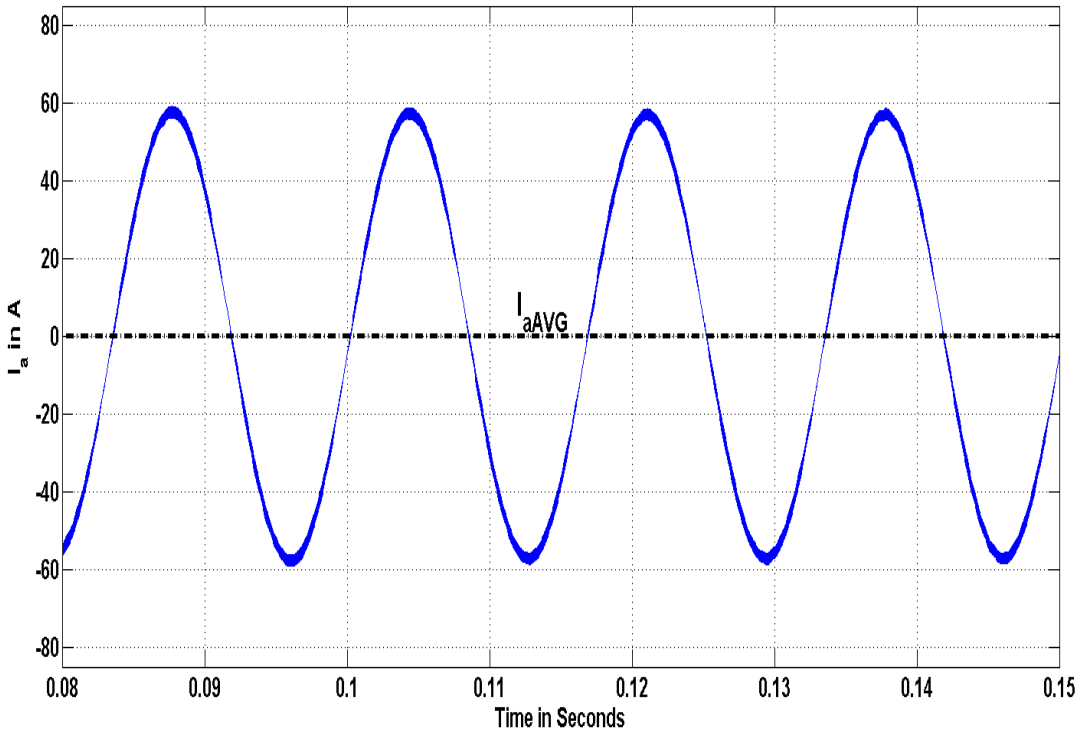


Figure 4-6 I_a waveform at normal condition

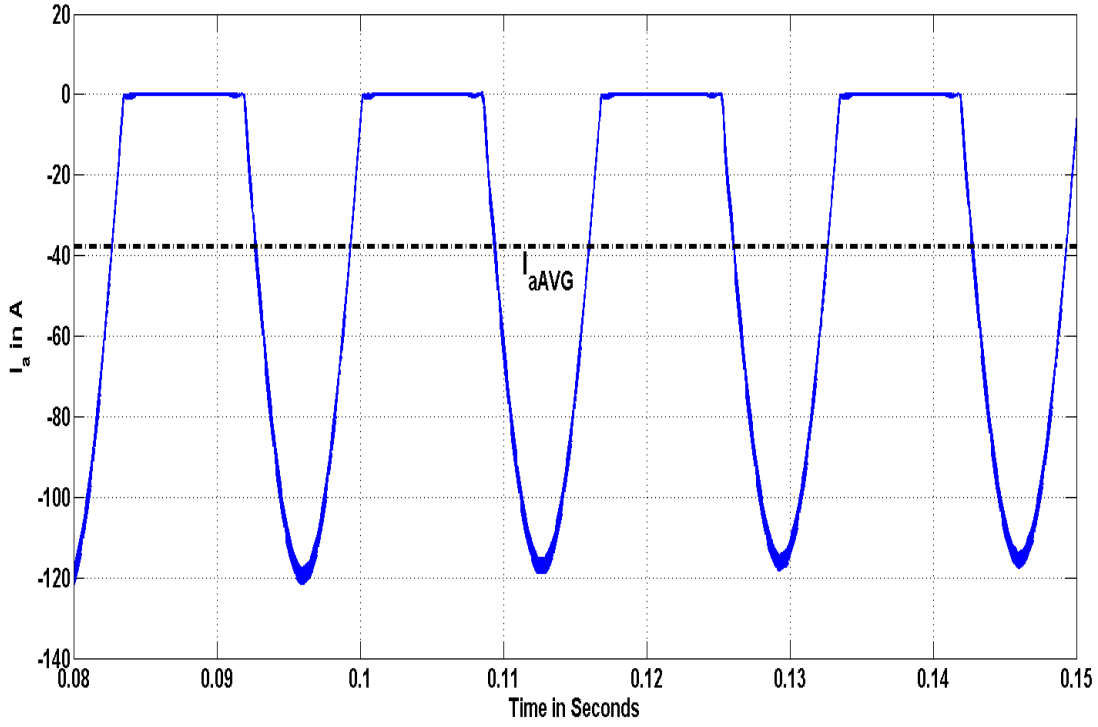


Figure 4-7 I_a waveform at T1 or T4 O-C fault conditions

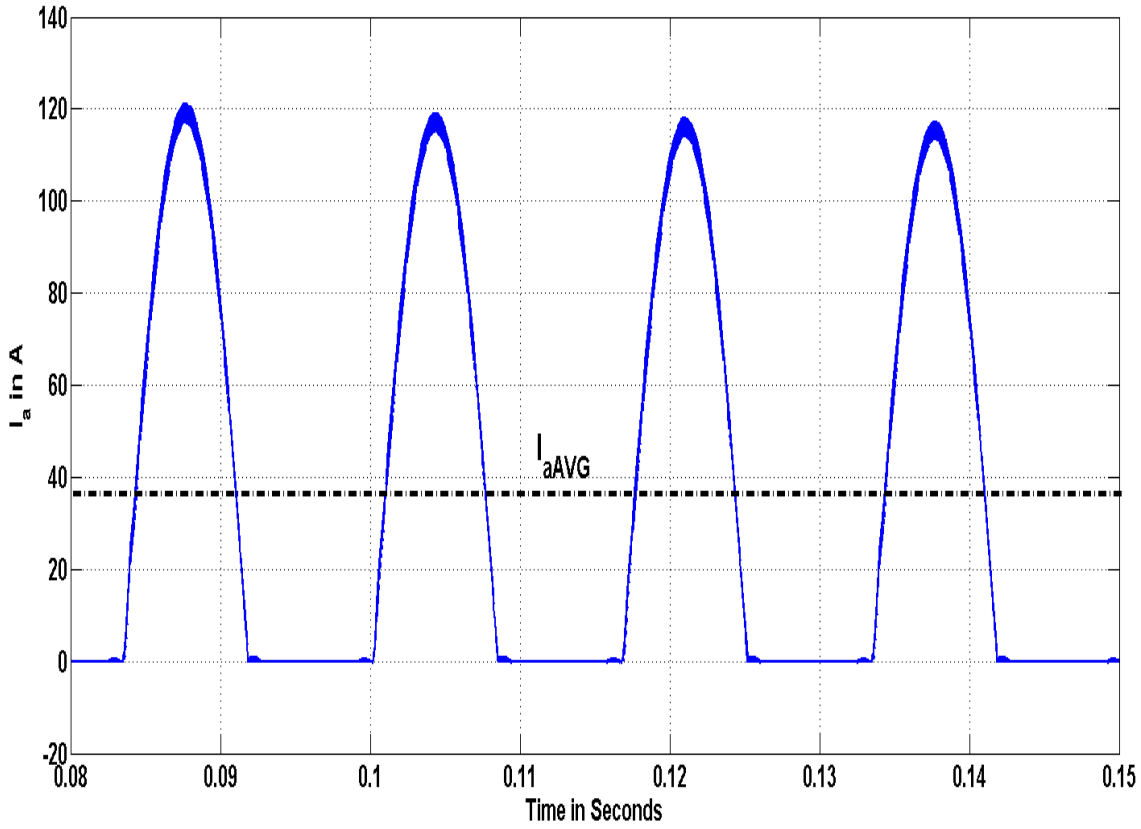


Figure 4-8 I_a waveform at T2 or T3 O-C fault conditions

During normal conditions, I_{aAVG} equals to:

$$I_{aAVG} = \frac{1}{2\pi}\int_{0}^{2\pi} I_{aMax}\sin\varphi \; d\varphi = 0 \tag{4.3.12}$$

However during T1 or T4 O-C faults, I_{aAVG} equals to:

$$I_{aAVG} = \frac{1}{2\pi}\int_{\pi}^{2\pi} I_{aMax}\sin\varphi \; d\varphi = -\frac{I_{aMax}}{\pi} \tag{4.3.13}$$

On the other hand, at T2 or T3 O-C faults, I_{aAVG} equals to:

$$I_{aAVG} = \frac{1}{2\pi}\int_{0}^{\pi} I_{aMax} \sin\varphi \; d\varphi = \frac{I_{aMax}}{\pi} \tag{4.3.14}$$

Therefore, the absolute value I_{aAbs} of I_{aAVG} can be used to detect the inverter O-C faults, in which I_{aAbs} goes to zero under normal conditions, but it is greater than zero during fault conditions, independent of the supply and loading conditions. Subsequently, at normal conditions:

$$I_{aAbS} = \left| I_{aAVG} \right| = 0 \tag{4.3.15}$$

However, under O-C fault conditions:

$$I_{aAbS} = \left| I_{aAVG} \right| \neq 0 \tag{4.3.16}$$

4.4 Fault Diagnoses Evaluation in the Experimental Environment

The validation of the proposed fault diagnostic methodologies in the experimental environment is implemented in this section. Figure 4-9 illustrates the experimental setup utilized for this research, where a DC motor replaces the wind turbine. The DC motor is

supplied by a variable DC source to vary its speed in order to represent the variations of the wind speed. The utilized DSP board in this research is TMS320LF2407 from Texas Instruments Incorporated, with implemented switching frequency 10 kHz.

4.4.1 Evaluation of the rectifier O-C fault diagnosis

The classes C0 to C6, which are listed in Table 3-2, are experimentally tested from input frequency f_o equal to 20 to 80 Hz in steps of 5 Hz. In each testing point, $Spect_{norm1}$ is calculated as presented in Figure 4-10. In the experimental testing, it is observed that classes C3 and C6 have the same behavior due to the fact that the diode in the third branch in the class C6 (Figure 4-11) is never conducting even if it is not faulted due to the natural commutation of three phase uncontrolled rectifier. Therefore, C6 becomes the same as C3 at the fault condition.

From the Figure 4-10, it is demonstrated that $Spect_{norm1}$ is approximately zero at the normal condition C0. However, at the O-C fault conditions, it goes from 3% to almost 85% depending on the fault class. Subsequently, the proposed diagnosis, as presented in Figure 4-12, can be utilized to identify the rectifier O-C faults, where the fault class C7 is detected individually by measuring the average value V_{Ravg} of V_R, which goes to zero at this fault class due to the total detachment between the output and the input of the rectifier circuit.

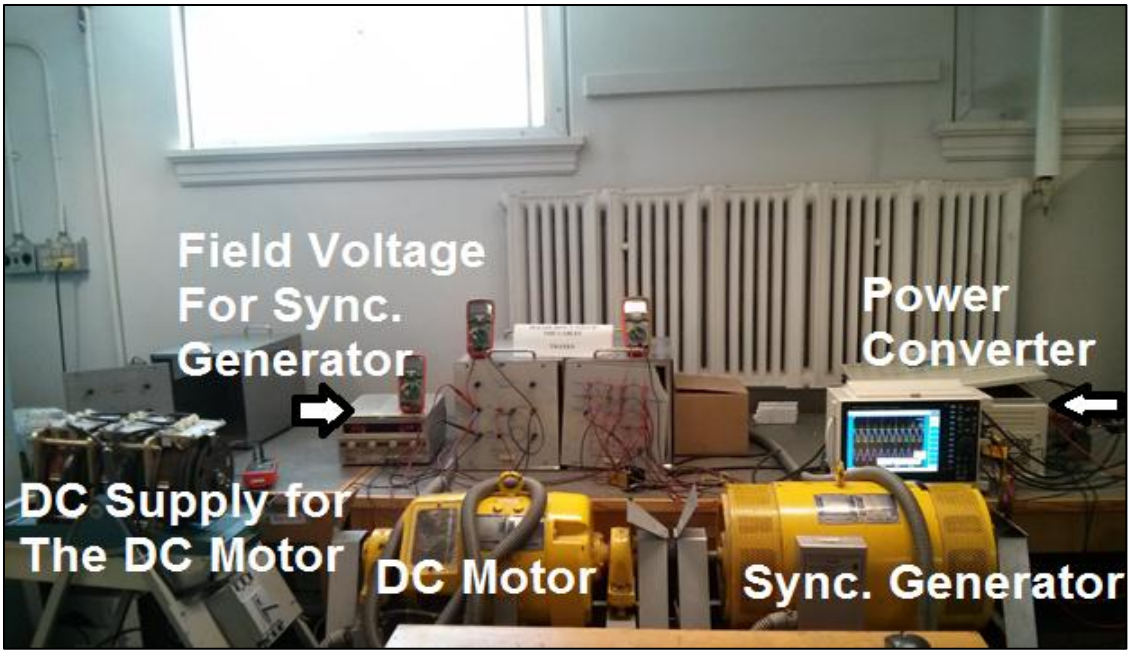


Figure 4-9 The experimental setup for the system under the study

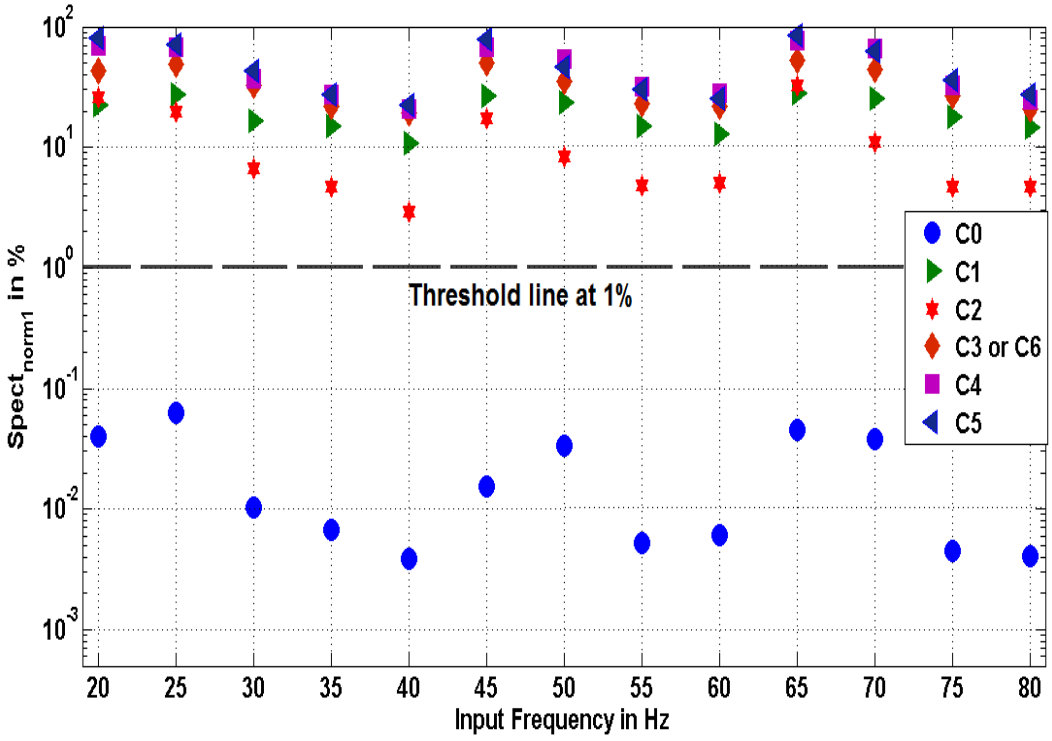


Figure 4-10 $Spect_{norm1}$ at normal and rectifier O-C fault conditions

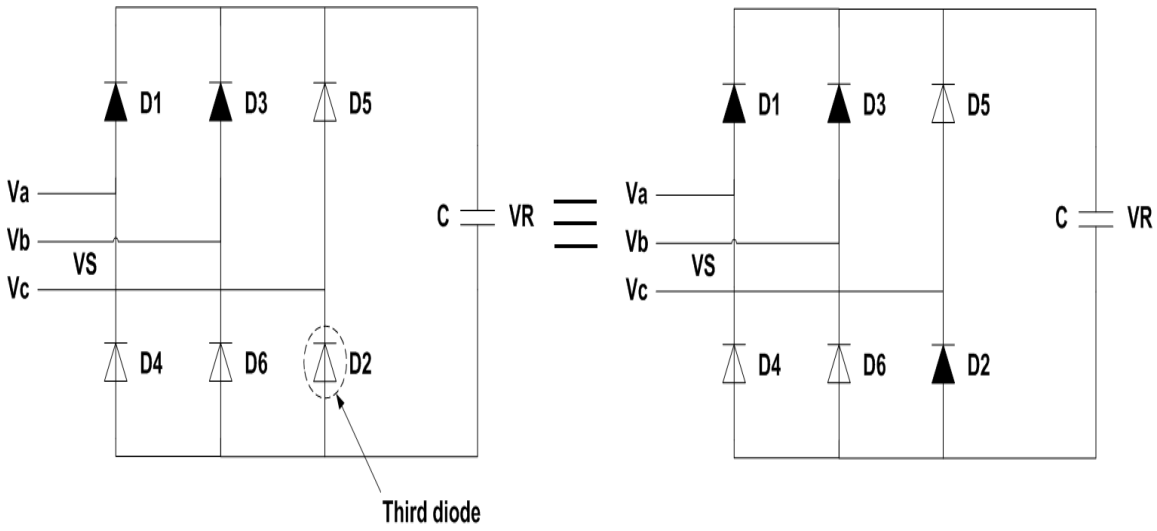


Figure 4-11 Rectifier O-C faults a) Class C6 b) Class C3

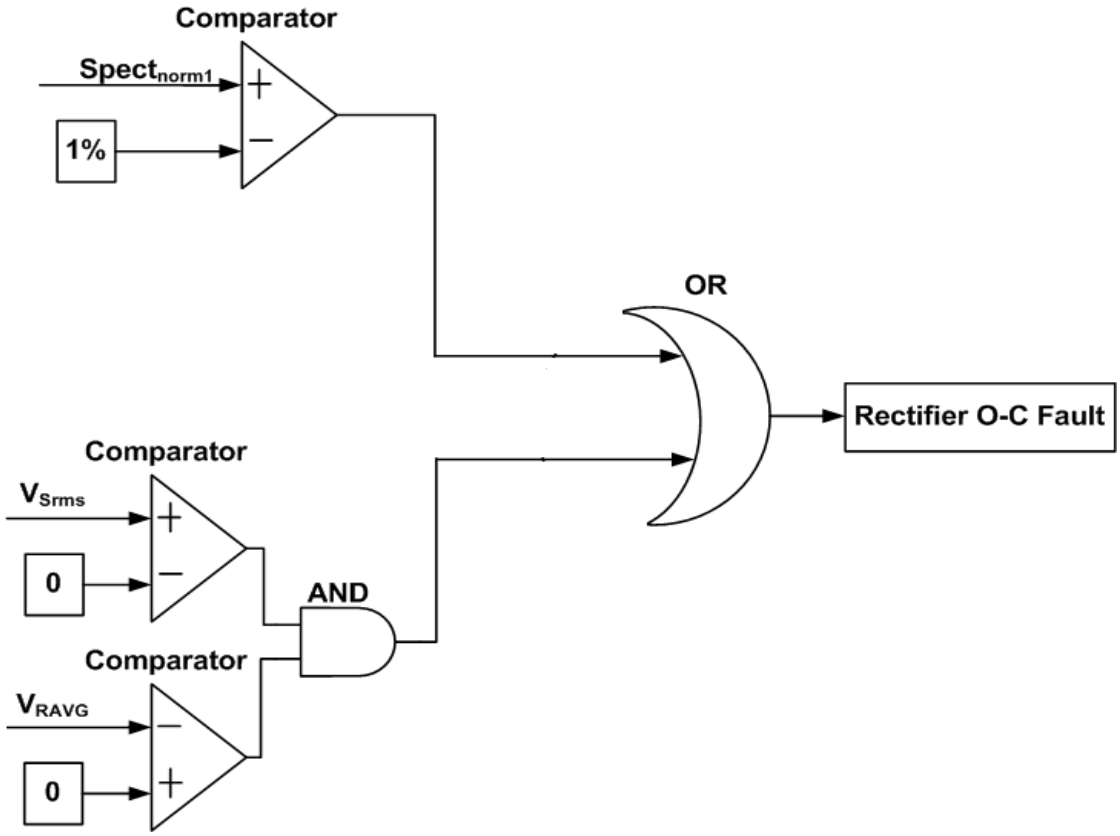


Figure 4-12 Proposed rectifier O-C fault diagnosis module

4.4.2 Evaluation of the input voltage unbalance diagnosis

The same experimental setup for the rectifier fault diagnosis is used to evaluate the proposed diagnosis for the input voltage unbalance. The unbalance occurs by adding a small variable resistance R_s in the path of one phase of the three input phases to the rectifier. This variable resistance is changed to 1, 1.5, and 2 ohms in order to have un unbalance ratio (UN) varying from 7% to 17% depending on the input voltage V_S. UN ratio is calculated as follows:

$$UN\% = \frac{I_{rms} * R_S}{V_{S\,rms}} * 100\% \tag{4.4.1}$$

where I_{rms} is the RMS value of the input phase current. Table 4-3 provides the unbalance ratios at these resistance values over the input frequency range from 20 Hz to 80 Hz in steps of 5 Hz. These unbalance conditions are experimentally implemented, as well as the normal conditions. The variable $Spect_{norm2}$ is calculated under these conditions as illustrated in Figure 4-13.

From the experimental testing, it is demonstrated that $Spect_{norm2}$ is smaller than 10% in normal conditions. However, $Spect_{norm2}$ is not equal to zero under normal conditions due to the non-ideal behaviour of the power converter operation, as well as the measuring errors of the converter sensors. On the other hand, it is more than 10% in the unbalanced conditions. Moreover, its value increases as the UN increases by raising the value of R_S.

Table 4-3 The UN classes at different input frequencies at R_s = 1, 1.5, and 2 ohms

Input frequency	UN1 in % at R_s = 1 Ω	UN2 in % at R_s = 1.5 Ω	UN3 in % at R_s = 2 Ω
20.00	7.29	9.97	12.81
25.00	7.42	10.34	13.16
30.00	7.71	10.85	13.76
35.00	7.89	11.15	14.18
40.00	8.07	11.51	14.34
45.00	8.22	11.76	14.76
50.00	8.49	12.10	15.26
55.00	8.75	12.43	15.65
60.00	8.76	12.59	16.25
65.00	8.90	12.73	16.25
70.00	8.95	12.99	16.55
75.00	9.08	13.21	16.71
80.00	9.24	13.17	17.16

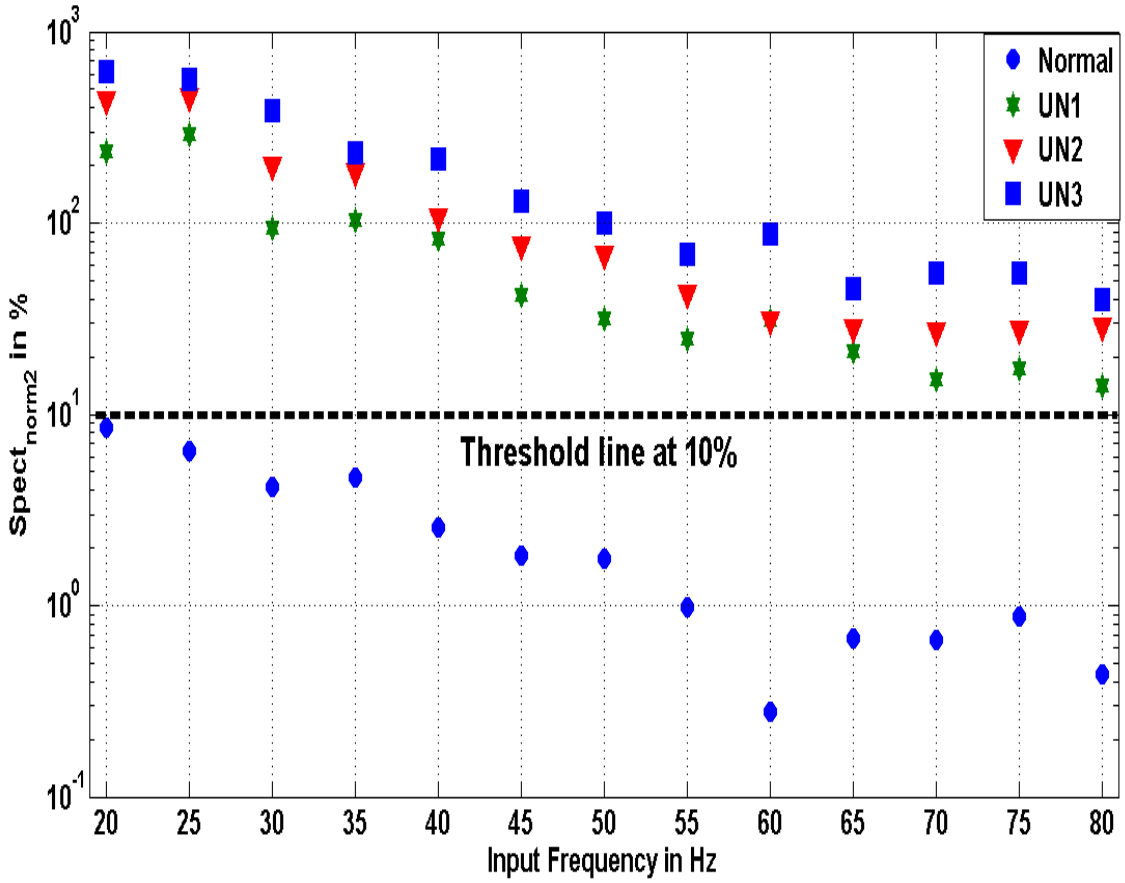


Figure 4-13 $Spect_{norm2}$ under normal and input voltage unbalance conditions

Consequently, the proposed diagnosis, as presented in Figure 4-14, can be utilized to identify the input voltage unbalanced conditions where the threshold criterion is chosen to be equal to 10% in order to include the non–ideal behaviour of the power converter and the measurement errors of the converter sensors.

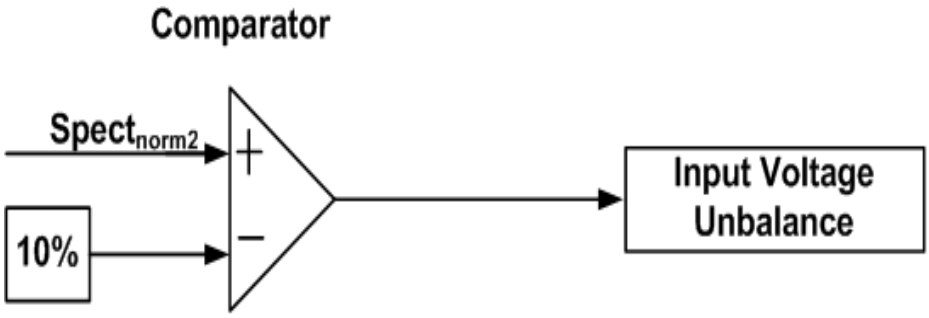


Figure 4-14 Proposed input unbalance voltage diagnosis

4.4.3 Evaluation of the boost chopper O-C fault diagnosis

The boost chopper O-C fault diagnosis is dependent on the voltage of the three-phase input supply V_S as presented in (3.2.10) and (3.2.11). However, the available range for V_S generated from the synchronous generator and utilized in the experimental setup (Figure 4-9) is up to 240V, which is insufficient to evaluate the proposed boost chopper O-C fault diagnosis over a wider range of the input voltage V_S. A wider range of V_S is required in order to validate equation (3.2.11). Therefore, the synchronous generator, as well as the DC motor and DC supply, are replaced with another AC power supply with available range for V_S up to 300 V, which is adequate for the experimental evaluation of the diagnosis. The AC power supply shown in Figure 4-15 has fixed frequency f_o at 60 Hz, and this does not affect the evaluation procedure of the proposed diagnosis because boost chopper diagnosis is independent of the frequency of the three-phase input supply and only depends on the average values of I_B and I_R as provided in (3.2.12) and (3.2.13).

Experimental tests are implemented at normal and switch T O-C fault conditions in a range of V_{Srms} from 50 to 300 V in steps of 25V. At each testing point, I_{BR} of (3.2.12) is calculated and illustrated in Figure 4-16.



Figure 4-15 The AC power supply

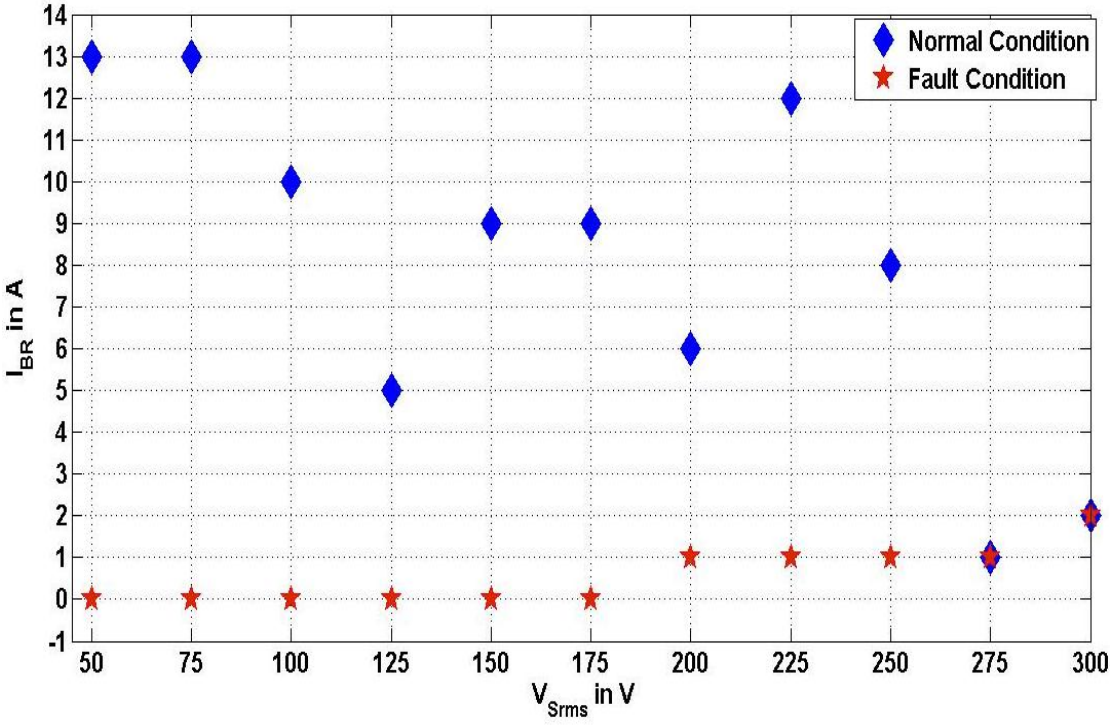


Figure 4-16 I_{BR} under normal and switch T O-C fault conditions

It is observed from Figure 4-16 that I_{BR} under normal conditions equals I_{BR} under fault condition when V_{Srms} equals to 275 and 300. This is because the duty factor k goes to zero under the normal condition at V_{Srms} greater than 270V, which makes the switch T open circuited without a fault, so the circuit exhibits the same behavior as if the switch T had the O-C fault. Moreover, it is found that I_{BR} goes to 1 or 2 A, but not to zero under some fault situations. This is due to measurement errors caused by the gains of the two current sensors of I_R and I_B, which leads to a non-zero calculated value for I_{BR} under these fault conditions.

Furthermore, experimental tests are carried out at the diode D O-C fault conditions in a range of V_{Srms} from 50 to 300 V in steps of 25V. In each testing point, I_{BAVG} is calculated and is compared to its value under normal conditions as shown in Figure 4-17. It is observed that I_{BAVG} is greater than zero at the normal conditions, but it goes to zero at the diode D fault conditions as demonstrated previously in (3.2.13).

Subsequently, the proposed diagnosis module (Figure 4-18) can be utilized to detect the boost chopper O-C faults, where the alarm for T O-C fault is not triggered at V_{Srms} greater than 270 as the switch T is normally open circuited at this condition. However, as soon as V_{Srms} becomes less than 270, the alarm operates immediately once I_{BR} becomes less than 2 A. Finally, the threshold values of 2 A for I_{BR} and 1 A for I_{BAVG} are selected in order to include the measurement errors caused by the gains of the current sensors of I_B and I_R.

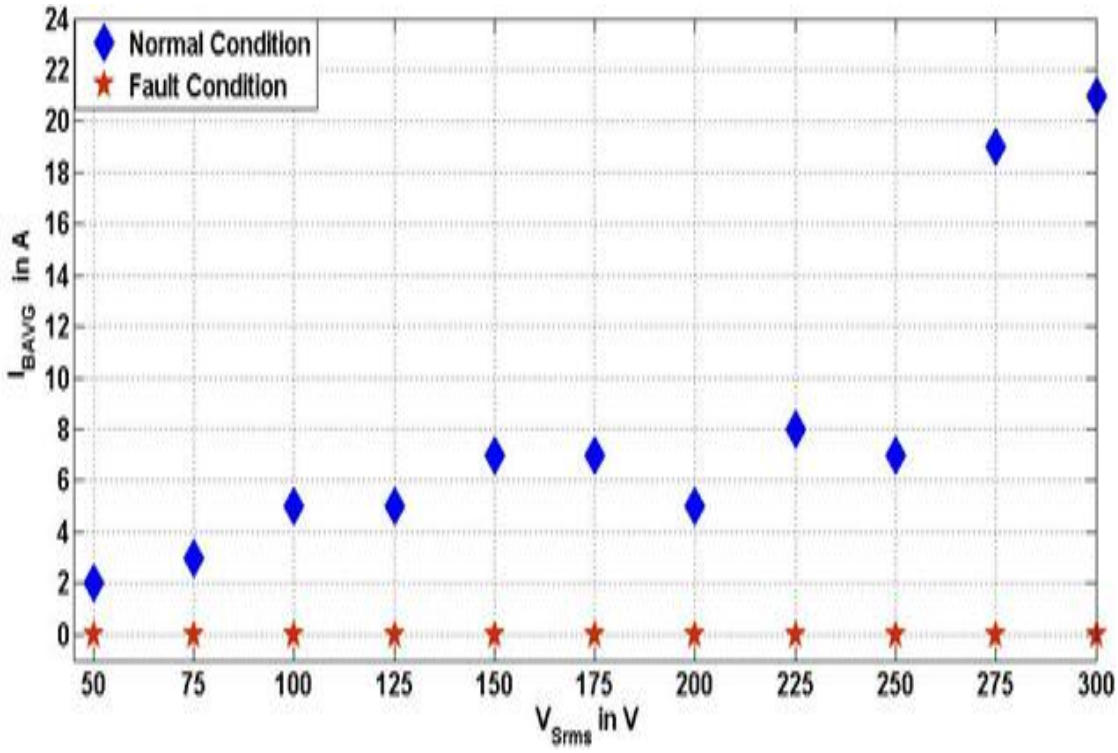


Figure 4-17 I_{BAVG} under normal and diode D O-C fault conditions

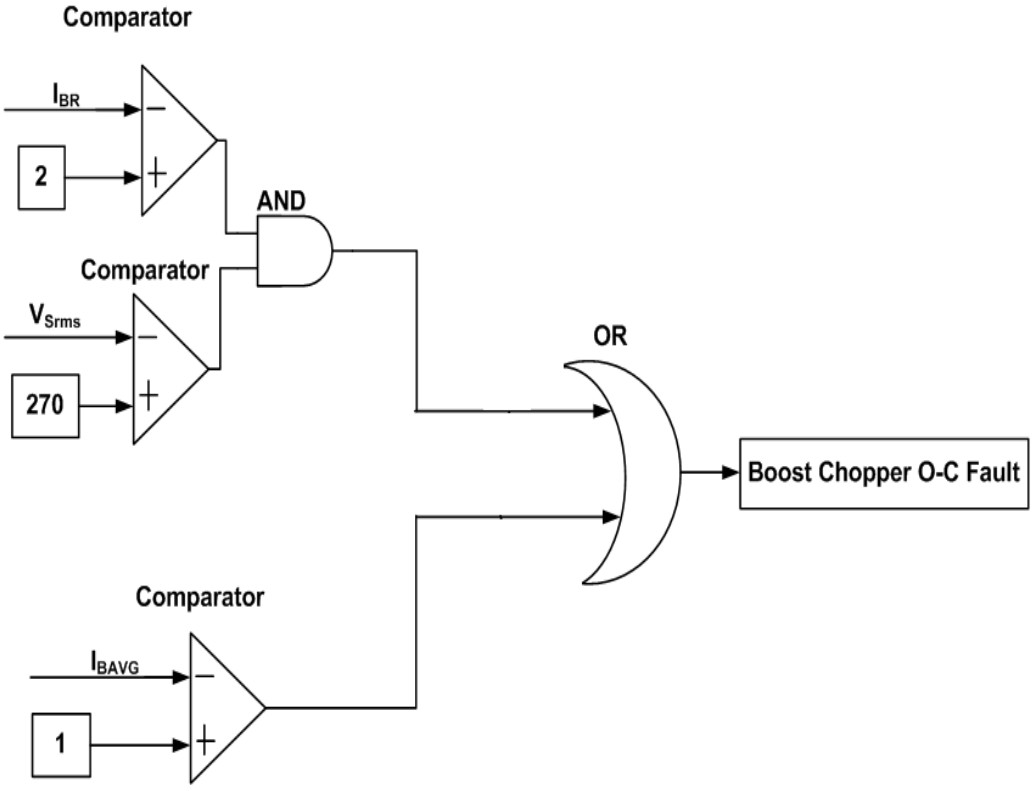


Figure 4-18 Proposed boost chopper O-C fault diagnosis

4.4.4 Evaluation of the inverter O-C fault diagnosis

I_{aAbs}, which is utilized in this research to identify the inverter O-C fault (4.3.15) (4.3.16), is totally independent on the input frequency f_o of the supply voltage. Therefore, the same experimental setup for the boost chopper fault diagnosis is used to evaluate the proposed diagnosis for the inverter fault diagnosis. Experimental tests are carried out at normal and switch T1 and T2 O-C fault conditions in a range of V_{Srms} from 50 to 300 V in steps of 25V. In each testing point, I_{aAVG} of (13) is calculated and shown in Figure 4-19.

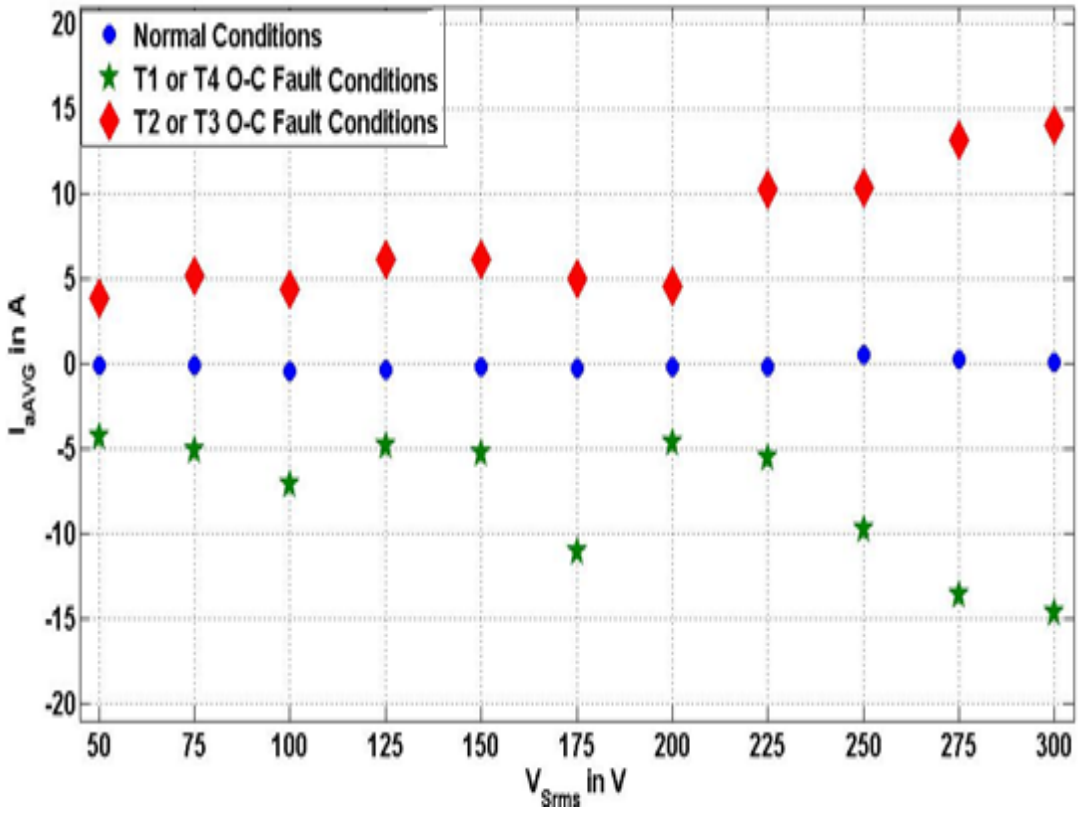


Figure 4-19 I_{aAVG} at normal and inverter O-C fault conditions

It is demonstrated in Figure 4-19 that I_{aAVG} at normal conditions goes to zero. However, its value is greater than zero in the T1 or T4 O-C fault conditions and it is less than zero in the T2 or T3 O-C fault conditions as verified before in (4.3.6), (4.3.7), and (4.3.8). Accordingly, the proposed diagnosis, as shown in Figure 4-20, can be utilized to detect the inverter O-C faults, where the threshold values are chosen in order to include the non-ideal operating conditions of the power converter.

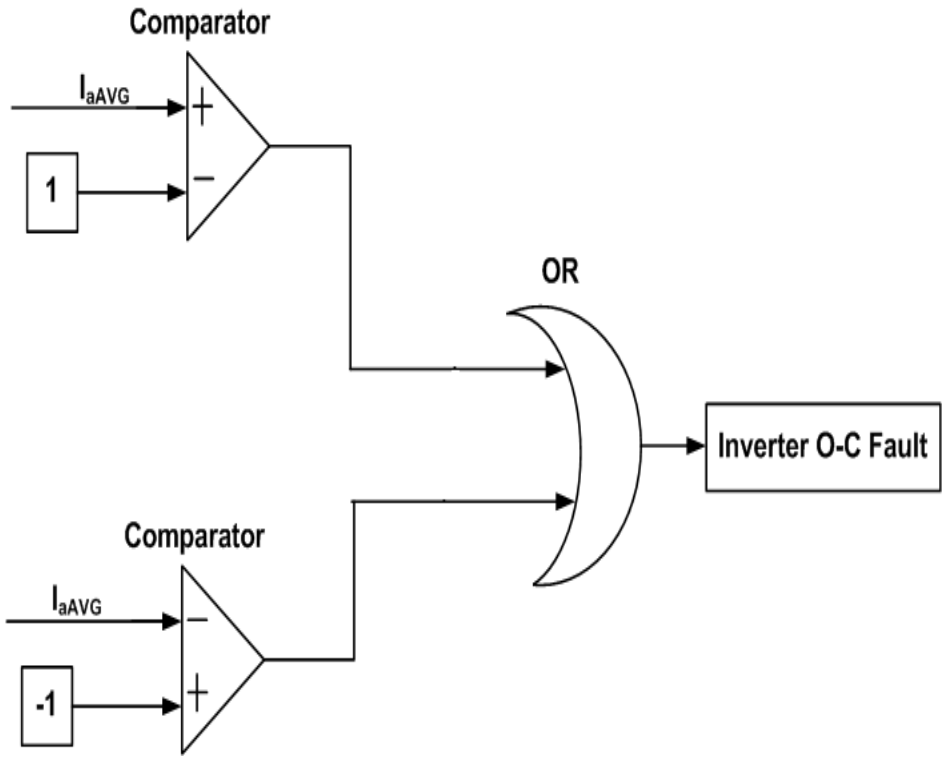


Figure 4-20 Proposed inverter O-C fault diagnosis

4.4.5 On-line testing for the proposed Fault diagnostic algorithms

The previous testing procedures are implemented in off-line testing situations where the measurements of the electrical signals are collected at normal and fault conditions, then, they are analyzed in order to develop the required fault diagnostic algorithms. In this subsection, on-line testing procedures are carried out at several normal and fault conditions in order to validate the proposed diagnostic algorithms after they are implemented in the converter DSP module. A variable (X_{FD}) is created in the DSP program so that it can be utilized an index for identifying and classifying the fault conditions according to its value as given in Table 4-4.

Table 4-4 Fault diagnostic index at normal and fault conditions

Conditions	Fault diagnostic target index X_{FD}
Normal conditions	0
Unbalance input voltage conditions	1
Rectifier O-C fault conditions	2
Boost chopper O-C fault conditions	3
Inverter O-C fault conditions	4

Figure 4-21 demonstrates the on-line testing situations at four different input supply frequencies (20, 40, 60, and 80 Hz) for normal and O-C fault conditions in the

power converter under study. X_{FD} is acquired in each condition in order to verify the output of the proposed algorithms. Based on Table 4-4 and Figure 4-21, it is deduced that the proposed fault diagnostic algorithms achieve accurate and precise decisions regardless the testing condition or the input supply frequencies.

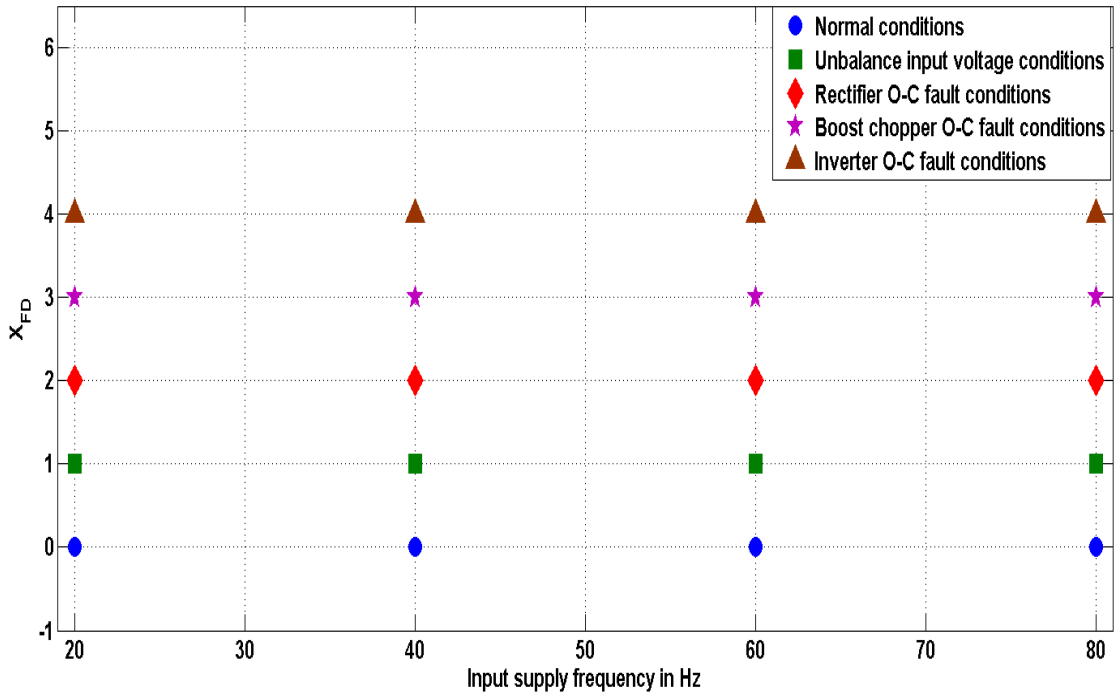


Figure 4-20 X_{FD} at different normal and fault conditions

4.5 Summary

The experimental evaluation Section of this chapter demonstrates that the proposed algorithms of O-C fault diagnoses achieve accurate fault detection, classification and localization for all three main subsystems of the power converter, as well as the detection of the input voltage unbalance. The proposed fault diagnostic algorithms has been

verified under normal and fault conditions in several supplying and loading situations.

The required inputs for the presented fault diagnostic methodologies are far fewer than those required by existing research. As a result, the proposed diagnostic algorithms are simple and practical in renewable energy and distributed generation systems for small and medium-size typical commercial power converters where the number of sensors and hardware is minimized in order to achieve optimal performance at lower costs.

Chapter 5: ANFIS-Based Diagnosis for O-C Faults in Power Converter

5.1 Preface

The conventional protection techniques for PECS are usually designed on the basis of fixed conventional relay settings. As a result, if the system parameters are altered or modified, the relay setting should be readjusted and improved. This is due to the total dependency of the conventional relay settings on the system configuration parameters as well as the fault conditions under study. Moreover, these protective schemes are deterministic computations assuming system modeling based on conventional mathematical models. Such system representations are not well suited for dealing with ill-defined and uncertain systems. As a consequence, if the system under study is not accurately modeled using the conventional mathematical equations, the developed protective relay could not work properly in such situations.

Alternatively, intelligent computational techniques such as Fuzzy Inference Systems (FIS), Artificial Neural Network (ANN), and Adaptive Neuro Fuzzy Inference System (ANFIS) can model qualitative aspects of human knowledge and restoring process without employing quantitative analysis. Thus, these approaches are receiving great attention nowadays, especially with the absence of a simple and well-defined mathematical model. These models are characterized by nonrandom uncertainties associated with vagueness and imprecision in real-time systems [46-47].

New researches implement the artificial intelligence techniques in the PECS applications. A monitoring system is designed in [22] to detect O-C faults in matrix converter topology, where a fuzzy expert system is used in order to ensure the effectiveness of the proposed method and its immunity to erroneous fault detections. A

fuzzy neural network with asymmetric membership function is proposed in [48] for the fault-tolerant control of a six-phase permanent-magnet synchronous motor drive system. Adaptive controllers for the induction machine drives are presented in [49-50] using a neural network reference system and expert fuzzy inference mechanism respectively. Finally, a fuzzy logic controller is utilized in [51-53] for the design and implementation of the energy management systems in the DC disturbed power generations.

This chapter presents an ANFIS-based diagnostic algorithm for O-C faults in the power converter under study. The ANFIS diagnostic unit becomes responsible for detecting, classifying and locating the O-C faults of the power converter in its three main circuits: three-phase rectifier, boost chopper and single-phase inverter circuits. Section 5.2 provides a brief description for the ANFIS structure. Then, Section 5.3 demonstrates the ANFIS-based diagnostic unit that is utilized for O-C faults in the converter. Following this, the evaluation for the proposed ANFIS diagnostic unit is illustrated in Section 5.4. Finally, Section 5.5 presents the summary of the proposed diagnostic algorithm in this chapter.

5.2 Adaptive Neuro Fuzzy Inference System (ANFIS) Structure

Fuzzy inference system is applied to model systems whose rule structure is essentially predetermined by the user's interpretation of the characteristics of the variables in the model. Fuzzy inference system considers only fixed membership functions that are chosen by the user. However, in some modeling situations, it becomes problematic to choose the membership functions solely from looking at the data. Rather than choosing the parameters associated with a given membership function, these parameters should be chosen to tailor the membership functions to the input/output data

in order to incorporate the variations in the data values. In such case the necessity of the ANFIS becomes obvious.

Neuro-adaptive learning techniques provide a method for the fuzzy modeling procedure to learn information about a data set. It computes the membership function parameters that best allow the associated fuzzy inference system to track the given input/output data. A network-type structure similar to that of a neural network can be used to interpret the input/output map so it maps inputs through input membership functions and associated parameters, and then through output membership functions and associated parameters to outputs.

The parameters associated with the membership functions change through the learning process. The computation of these parameters (or their adjustment) is facilitated by a gradient vector. This gradient vector provides a measure of how well the fuzzy inference system is modeling the input/output data for a given set of parameters. When the gradient vector is obtained, any of several optimization routines can be applied in order to adjust the parameters to reduce error measures. This error measure is usually defined by the sum of the squared difference between actual and desired outputs.

The ANFIS toolbox in the MATLAB program [43] uses a combination of least squares estimation and back propagation for membership function parameter estimation and also has several properties:

- It is first or zeroth-order Sugeno-type system;
- It has a single output, obtained using weighted average defuzzification;

- It has no rule sharing. Different rules do not share the same output membership function, namely the number of output membership functions must be equal to the number of rules;
- It has unity weight for each rule.

Figure 5-1 shows the architecture of the ANFIS, comprising fuzzification, inference mechanism, defuzzification, and output layers. The network can be visualized as consisting of inputs, N inputs and M input membership functions for each input, with F = M*N neurons in the fuzzification layer. There are $R = M^N$ rules and R neurons in the inference mechanism and defuzzification layers respectively. Finally, there is one neuron in the output layer.

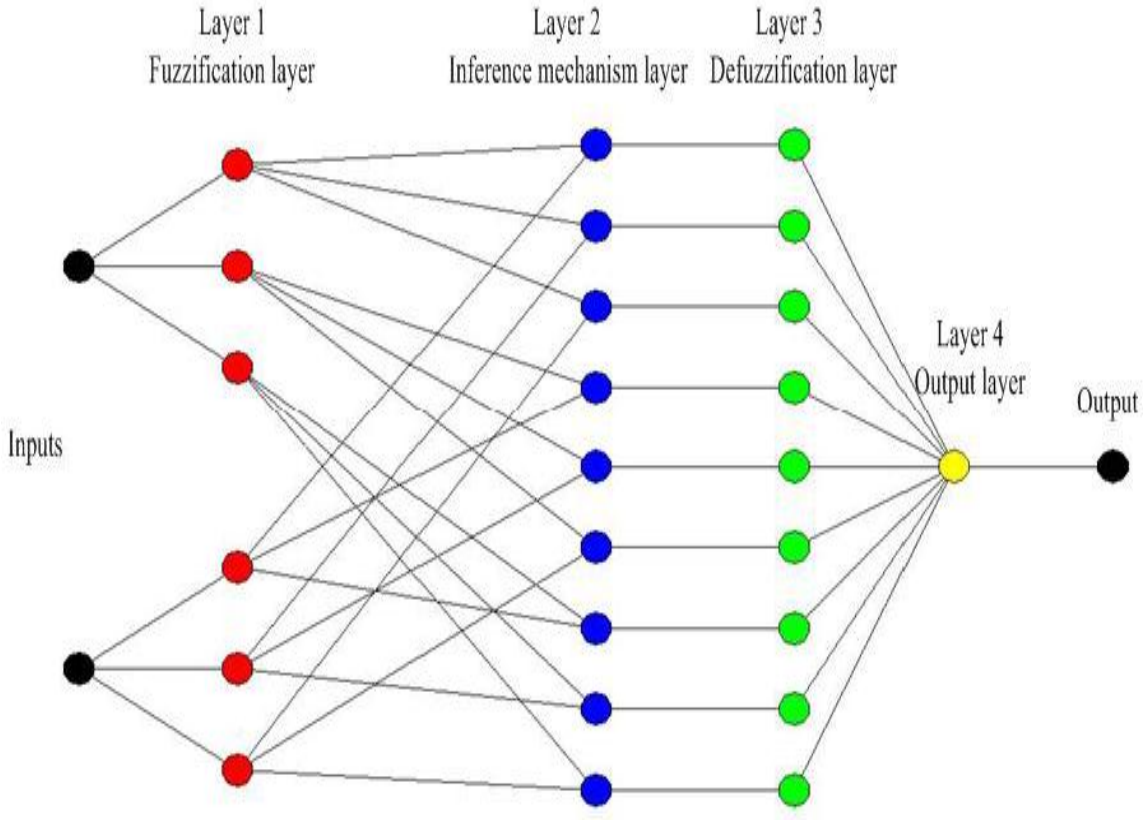


Figure 5-1 The architecture of the ANFIS

For simplicity, it is assumed that in Fig. 5-1 the fuzzy inference system has two inputs x and y with three input membership functions for each input and one output z. Therefore, N = 2, M = 3, and R = 3^2 = 9.

For first order Sugeno fuzzy model, two fuzzy if-then rules from the R rules are as following [50]:

$$Rule\ 1: if\ \ x\ is\ A_1\ and\ y\ is\ B_1\ then\ f_1 = p_1\ x + q_1\ y + r_1\ , \tag{5.2.1}$$

$$Rule\ 2: if\ \ x\ is\ A_2\ and\ y\ is\ B_2\ then\ f_2 = p_2\ x + q_2\ y + r_2\ . \tag{5.2.2}$$

The symbol $O_{n,j}$ is used to denote the output of the j^{th} node of layer n in the following subsections.

5.2.1 Layer 1: fuzzification layer

Every node j in this layer is an adaptive node with a node function:

$$O_{1,j}\ =\ \mu_{Ai}\ (x)\ \ for\ i\ =\ 1, 2, 3\ and\ j =\ 1, 2, 3\ , \tag{5.2.3}$$

$$O_{1,j}\ =\ \mu_{Bi}\ (y)\ \ for\ i\ =\ 1, 2, 3\ and\ j =\ 4, 5, 6\ , \tag{5.2.4}$$

where i is the index for the three input membership functions for each input. x (or y) is the input to nodes j = 1, 2, 3 (or 4, 5, 6), and A_i (or B_i) i =1, 2, 3 is a linguistic label

associated with these nodes. In other words, $O_{1,j}$ is the membership grade of a fuzzy set A_i (or B_i), and it specifies the degree to which the given input x (or y) satisfies the quantifier A (or B).

The commonly used membership functions μ_{Ai} (or μ_{Bi}) are the triangular, trapezoidal and Gaussian function. The triangular membership curve (Figure 5-2) is a function of an input vector x, and it depends on three scalar parameters a, b, and c, as given in (5.2.5).

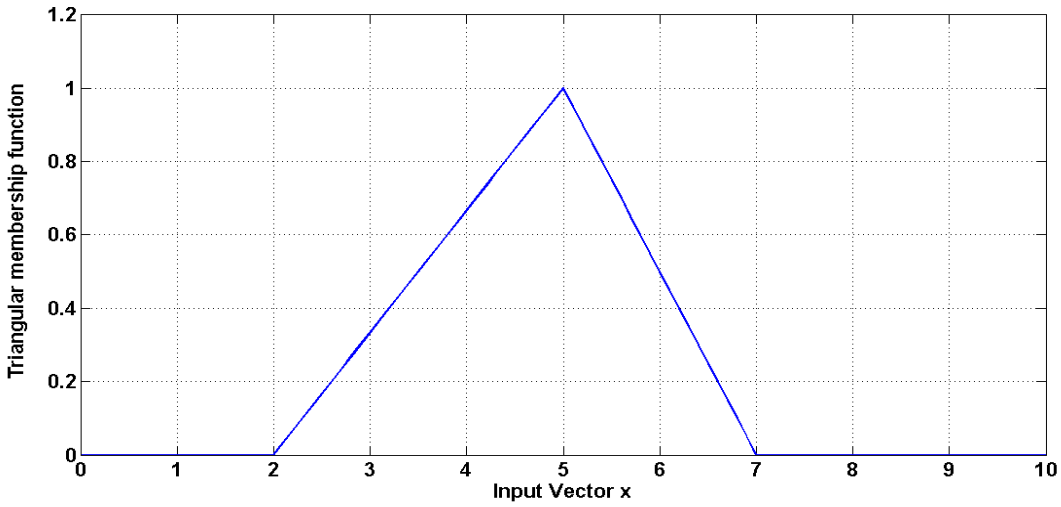


Figure 5-2 Triangular membership function at [a b c] = [2 5 7]

The trapezoidal membership curve (Figure 5-3) is a function of a vector x, and it depends on four scalar parameters a, b, c, and d, as given in (5.2.6). Finally, the Gaussian function (Figure 5-4) depends on two parameters a and b as given in (5.2.7):

$$\mu\,(x;a,b,c) = \begin{cases} 0, & x \le a \\ \dfrac{x-a}{b-a}, & a \le x \le b \\ \dfrac{c-x}{c-b}, & b \le x \le c \\ 0, & c \le x \end{cases}, \tag{5.2.5}$$

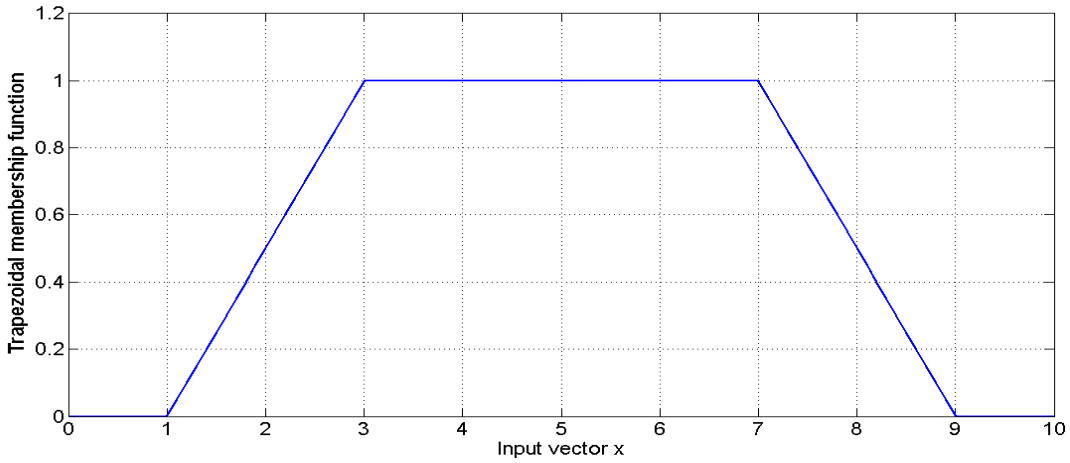


Figure 5-3 Trapezoidal membership function at [a b c d] = [1 3 7 9]

$$\mu\,(x;a,b,c,d) = \begin{cases} 0, & x \le a \\ \dfrac{x-a}{b-a}, & a \le x \le b \\ 1, & b \le x \le c \\ \dfrac{d-x}{d-c}, & c \le x \le d \\ 0, & c \le x \end{cases}. \tag{5.2.6}$$

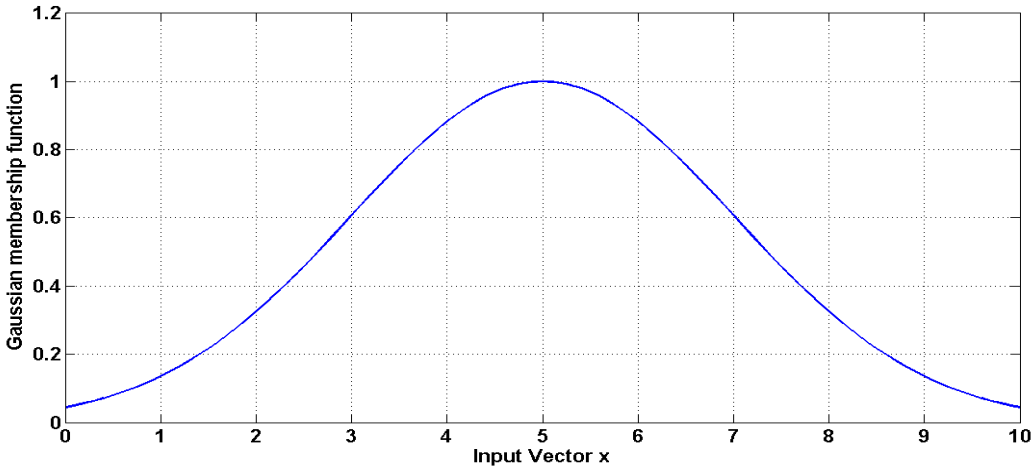


Figure 5-4 Gaussian membership function at [a b] = [5 2]

$$\mu\,(x;a,b) \;=\; e^{\frac{-(x-a)^2}{2b^2}} \qquad (5.2.7)$$

Parameters in this layer are referred to as premise parameters.

5.2.2 Layer 2: inference mechanism layer

Every node in this layer is a fixed node whose output is the product of all the incoming signals, and its output represents the firing strength of a rule where the AND operator is used as the node function in this layer:

$$O_{2,j} = w_j = \mu_{Ai}(x) \bullet \mu_{Bi}(y) \text{ for } i = 1,2,3 \text{ and } j = 1,2,....,R \quad . \qquad (5.2.8)$$

5.2.3 Layer 3: defuzzification layer

Every node j in this layer is an adaptive node with a node function as follows:

$$O_{3,j} = w_j \,.\, f_j \quad for\ j = 1,2,...R \quad , \tag{5.2.9}$$

where w_j is the output of layer 2, and f_j is the membership function of the output. There are two types of output membership functions in the ANFIS toolbox in the MATLAB program [42] as follows.

$$Linear\ membership\ fuction: \quad f_j = p_j\ x + q_j\ y + r_j \ . \tag{5.2.10}$$

$$Constant\ membership\ fuction: \quad f_j = r_j \ . \tag{5.2.11}$$

where p_j, q_j, and r_j are the coefficients of the output equations. Parameters in this layer will be referred to as consequent parameters.

5.2.4 Layer 4: output layer

The single node in this layer is a fixed node, which computes the overall output as the summation of all incoming signals as follows:

$$O_{4,j} = \frac{\sum_{j=1}^{R} w_j \ f_j}{\sum_{j=1}^{R} w_j} \ . \tag{5.2.12}$$

From the ANFIS architecture shown in Figure 4-1, it is observed that when the values of the premise parameters are fixed, the overall output can be expressed as a linear

combination of the consequent parameters. In symbols, the final output in Layer 4 can be rewritten as:

$$z = overall\ \ output\ \ = \frac{\sum_{j=1}^{R} w_j\ f_j}{\sum_{j=1}^{R} w_j} = \frac{w_1}{\sum_{j=1}^{R} w_j} f_1 + \frac{w_2}{\sum_{j=1}^{R} w_j} f_2 + ... + \frac{w_R}{\sum_{j=1}^{R} w_j} f_R\ , \qquad (5.2.13)$$

as w_1, w_2,…, and w_R are assumed to be constant. Therefore, (5.2.13) is considered to be linear in the consequent parameters f_1, f_2, ….., and f_R. From this observation, it can be concluded that:

$$S = S_1 \oplus S_2\ , \qquad (5.2.14)$$

where $\oplus$ represents direct sum, and S, S_1, and S_2 are as following:

- S = set of total parameters;
- S1 = set of premise (nonlinear) parameters; e.g. a, b, c, and d parameters of the input membership functions μ.
- S2 = set of consequent (linear) parameters; e.g. p, q and r parameters of the output membership functions f.

Therefore the overall output will be:

$$z = F(j, S)\ , \qquad (5.2.15)$$

where j is the vector of input variables, F is the overall function implemented by the adaptive network, and S is the set of all parameters which can be divided into two sets. Consequently, the hybrid-learning algorithm can be applied in two reversed passes. In the forward pass, node outputs go forward until Layer 3, and the consequent parameters are updated by the least-squares method. In the backward pass, the error signals propagate backward, and the premise parameters are updated by gradient descent [54]. Table 5-1 summarizes the activities in each pass.

Table 5-1 Two passes in the hybrid learning procedure for ANFIS [54]

Parameters and signals	Forward pass	Backward pass
Premise parameters	Fixed	Gradient descent
Consequent parameters	Least-squares estimator	Fixed
Signals	Node outputs	Error signals

5.3 ANFIS Fault Diagnostic Algorithm

A decision-making unit for the O-C fault diagnosis of the grid-connected power converters is developed by ANFIS algorithm in this chapter. The ANFIS diagnostic unit is used to detect, classify, and locate the O-C faults of the power converter in its three main circuits; three-phase rectifier, boost chopper and single-phase inverter circuits. The circuit diagram of the power converter under study is shown in Figure 5-5.

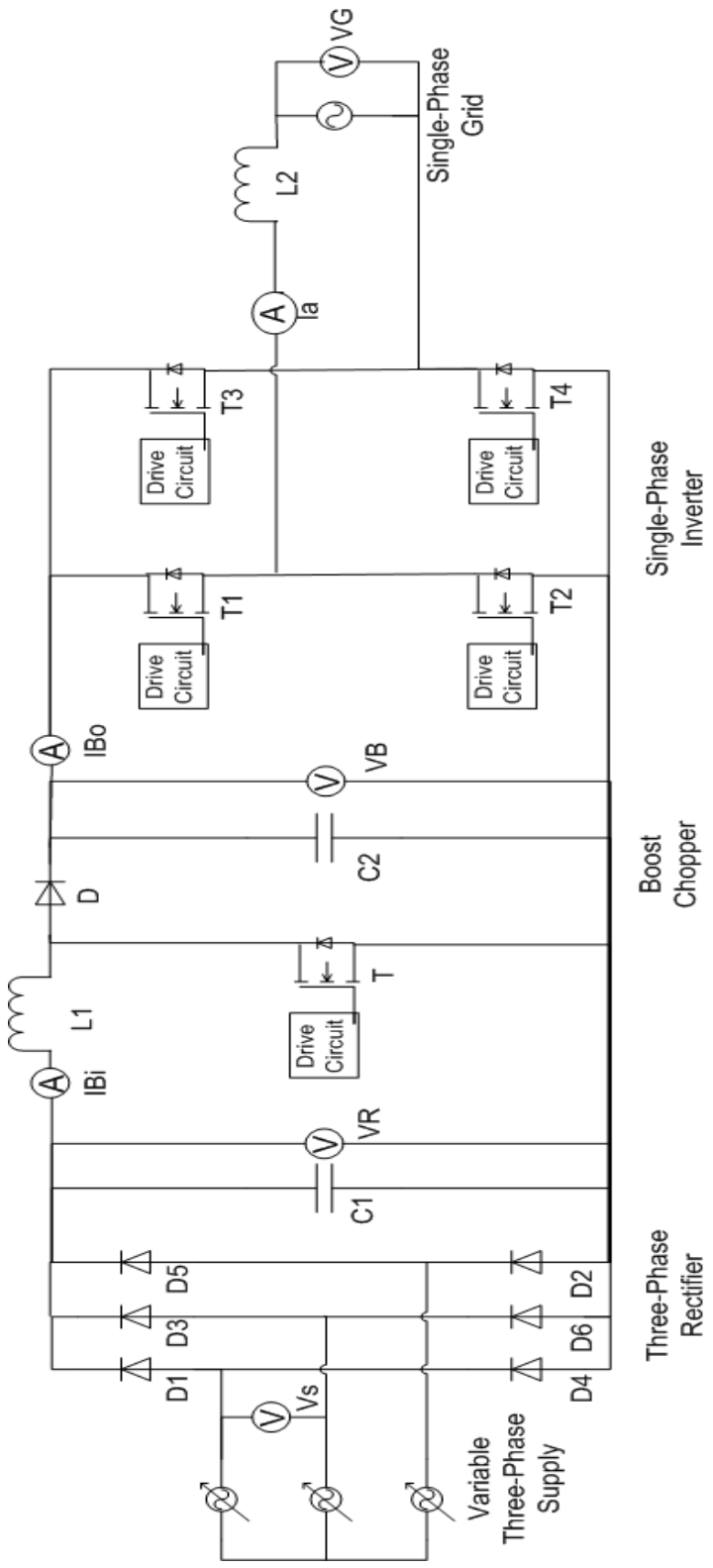


Figure 5-5 Circuit diagram for the power converter

There are five inputs to the ANFIS diagnostic unit, which are given in Table 5-2. On the other hand, there is one output for the proposed ANFIS unit, which is utilized as index for detecting, classifying, and locating the O-C faults in the power converter according to its value, as provided in Table 5-3.

The proposed ANFIS network is demonstrated in Figure 5-6 with its inputs and output indices. Data sets are established in MATLAB/Simulink in order to train and test the proposed ANFIS diagnostic unit at the normal and the fault conditions from input frequency 20 Hz to 80 Hz in steps of 1 Hz. There are a total of 793 data pairs created in order to train and test the proposed ANFIS-fault diagnostic unit.

Table 5-2 The inputs of the ANFIS diagnostic unit

Input No.	Identification
Input 1	The summation of the normalized components of the first and second harmonic orders of V_R, i.e ($V_{R12N} = V_{R1N} + V_{R2N}$)
Input 2	The difference of the average values of the input and out current of the boost chopper circuit, i.e ($I_{BR} = I_{RAVG} - I_{BAVG}$)
Input 3	The output current of the boost chopper circuit, i.e (I_B)
Input 4	The normalized average value of the output current of the inverter circuit, i.e (I_{a0N})
Input 5	The normalized component of the first harmonic order of the inverter circuit, i.e (I_{a1N})

The fault conditions are carried out at the O-C fault conditions of the three main circuits of the power converter as follows:

- Rectifier O-C fault classes, which are described previously in Table 3-2;
- Boost chopper O-C faults at T and D switches;
- Gate Drive O-C faults for the four switches in the inverter circuit;
- IGBT O-C faults for the four switches in the inverter circuit.

80% of the data sets are selected randomly and used to train the proposed ANFIS network. On the other hand, the 20% reminder is utilized in testing and verifying the performance of the ANFIS network.

Table 5-3 The output indices of the ANFIS diagnostic unit

Output Index	Identification
0	Normal conditions
1	O-C fault conditions in the rectifier circuit
2	T O-C fault conditions
3	D O-C fault conditions
4	T1 or T4 Gate Drive O-C fault conditions
5	T2 or T3 Gate Drive O-c fault conditions
6	T1 or T4 IGBT O-C fault conditions
7	T2 or T3 IGBT O-C fault conditions

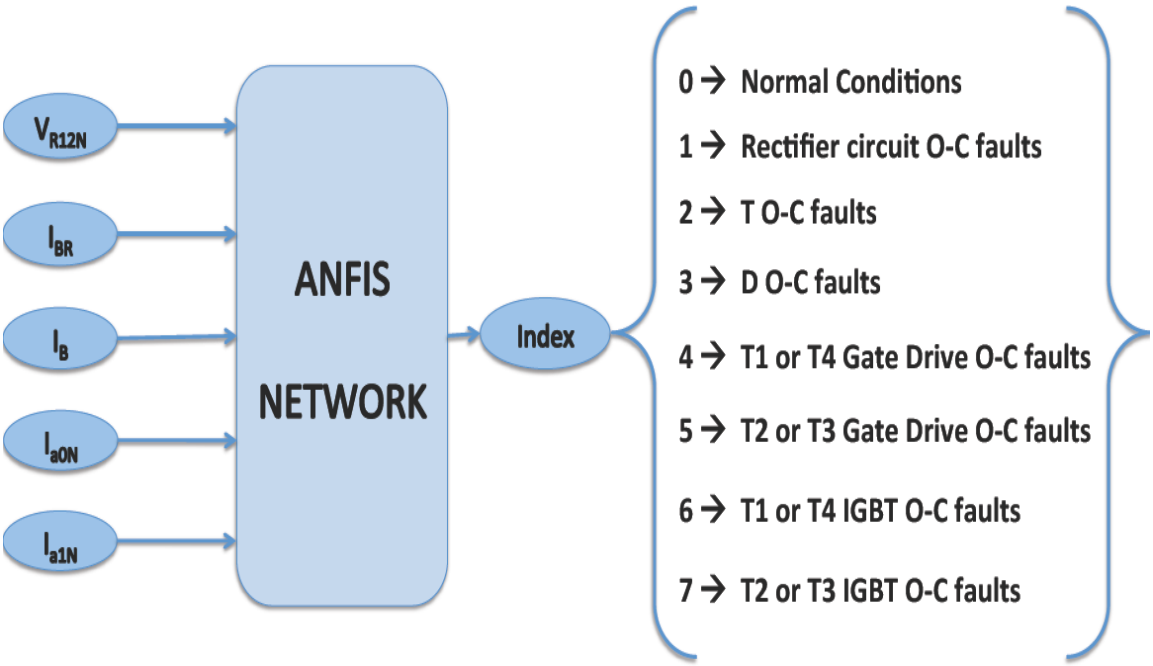


Figure 5-6 ANFIS network with its inputs and output indices for the O-C faults in power converter

Four membership functions are selected for each of the five inputs. The types of the input membership functions are chosen to be either triangular, trapezoidal, or Gaussian functions. Similarly, the types of the output membership functions are selected to be either constant or linear functions. Different combinations of the input and output membership function are implemented in order to determine which combination could achieve the least training error between the output of the training data pairs and their required targets. Table 5-4 provides the training error for each possible combination of the input and output membership functions.

As demonstrated in Table 5-4, the input Gaussian membership function and the output linear membership function is the best selection for the proposed ANFIS-fault diagnostic unit with the minimum training error 1.08%.

Table 5-4 The training error for different combinations of the input and output membership functions (mf)

Membership function (mf)	Output constant mf	Output linear mf
Input triangular mf	9.26%	2.11%
Input trapezoidal mf	28.02%	3.24%
Input Gaussian mf	10.13%	1.08 %

5.4 ANFIS Fault Diagnosis Evaluation

In order to verify the validity of the proposed trained ANFIS system, 20% of the established data sets are used to test the ANFIS network.

Moreover, the testing data includes a white Gaussian noise of signal-to-noise ratio (SNR) of 30 dB and 20 dB in order to represent the non-ideal operating conditions of the power converter, as well as the measurements errors due to the converter sensors and the interference of the signals inside the converter. SNR can be calculated as shown in (5.4.1), where A_S and A_N are the signal and noise amplitudes respectively:

$$SNR = 20\ log_{10}\frac{A_S}{A_N} \quad . \tag{5.4.1}$$

Figures 5-7 to 5-15 provide the ANFIS outputs for the test cases. These ANFIS outputs are compared with the desired target indices as provided in Table 5-3 which are illustrated as dashed straight lines in each figure.

Furthermore, it is found that the proposed ANFIS unit provides false diagnostic decisions when a pulse noise is introduced to the testing data with 30% of the input signal amplitudes where this noise is not including in the training data.

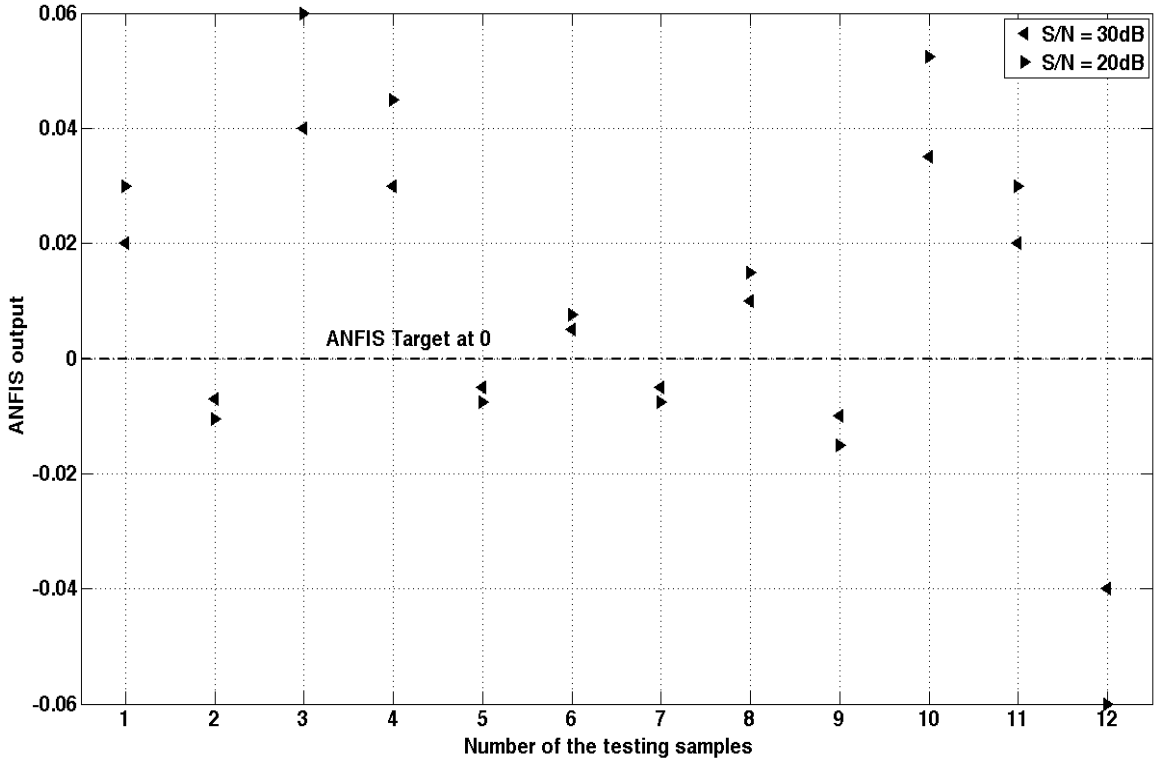


Figure 5-7 ANFIS outputs and target at normal conditions

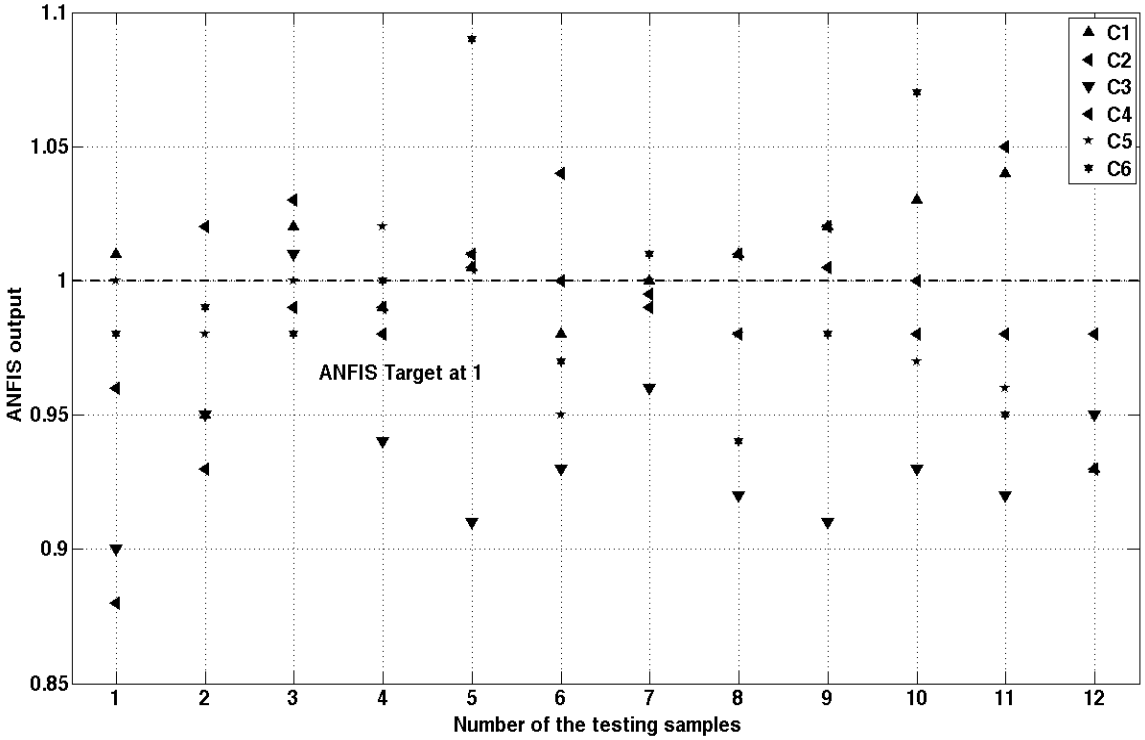


Figure 5-8 ANFIS outputs and target at rectifier fault classes at SNR 30 dB

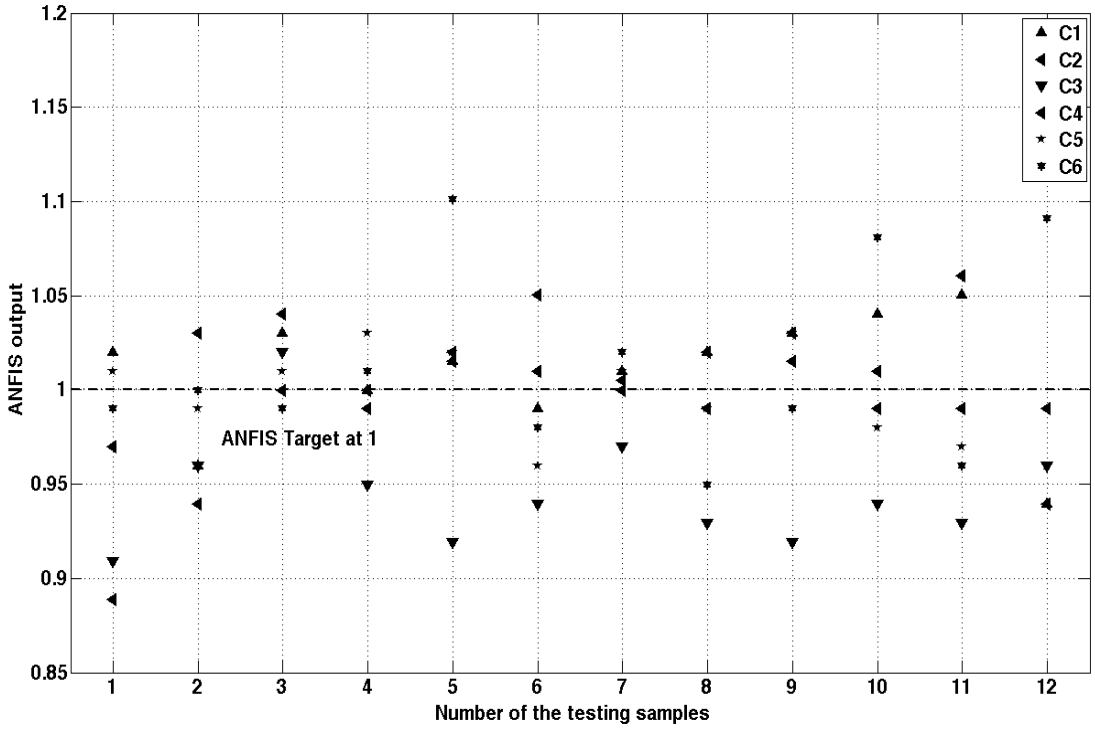


Figure 5-9 ANFIS outputs and target at rectifier fault classes at SNR 20 dB

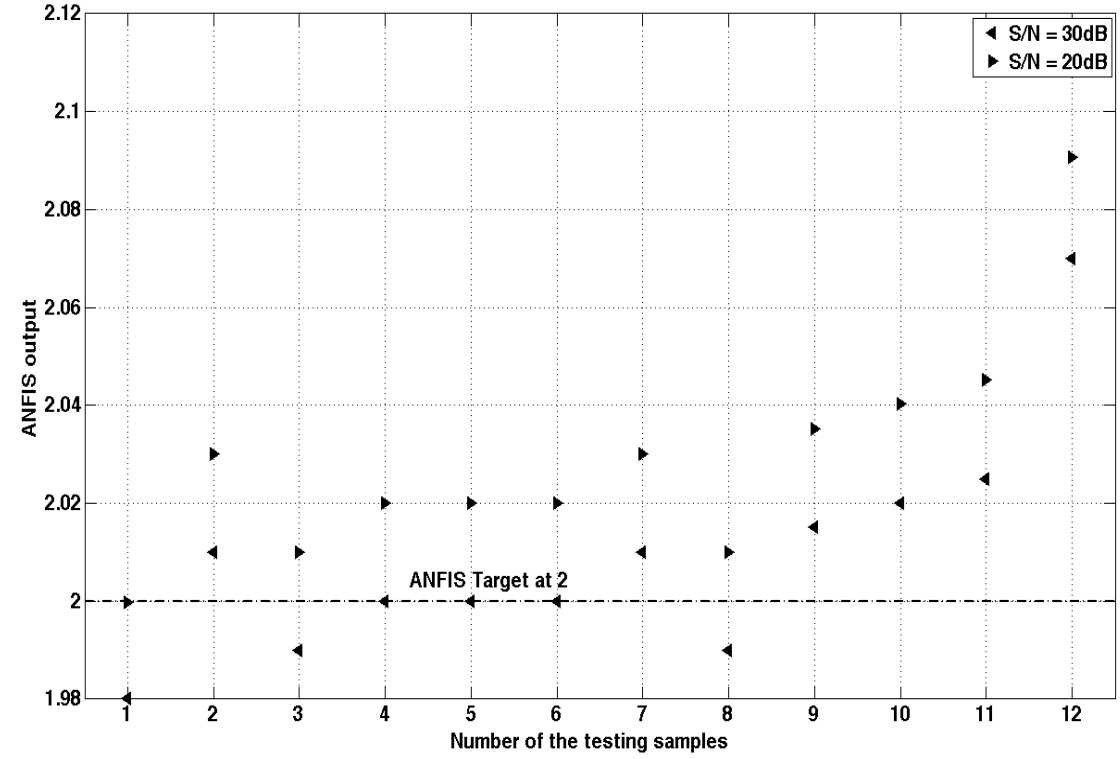


Figure 5-10 ANFIS outputs and target at T O-C fault conditions

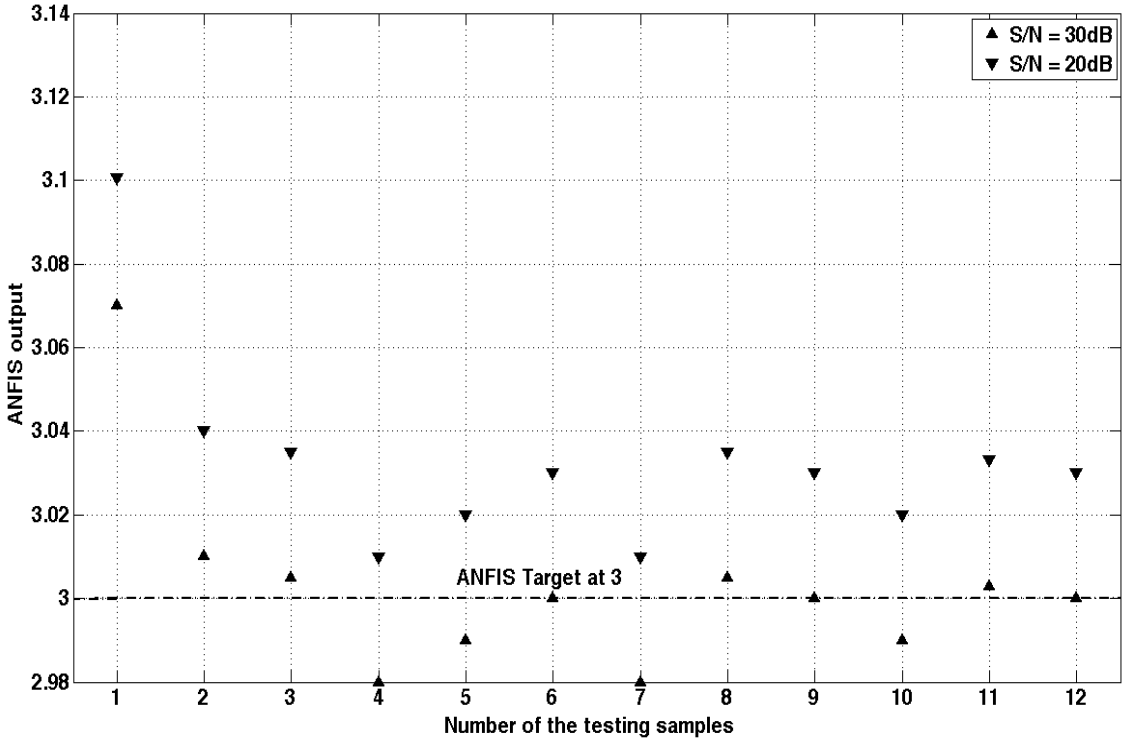


Figure 5-11 ANFIS outputs and target at D O-C fault conditions

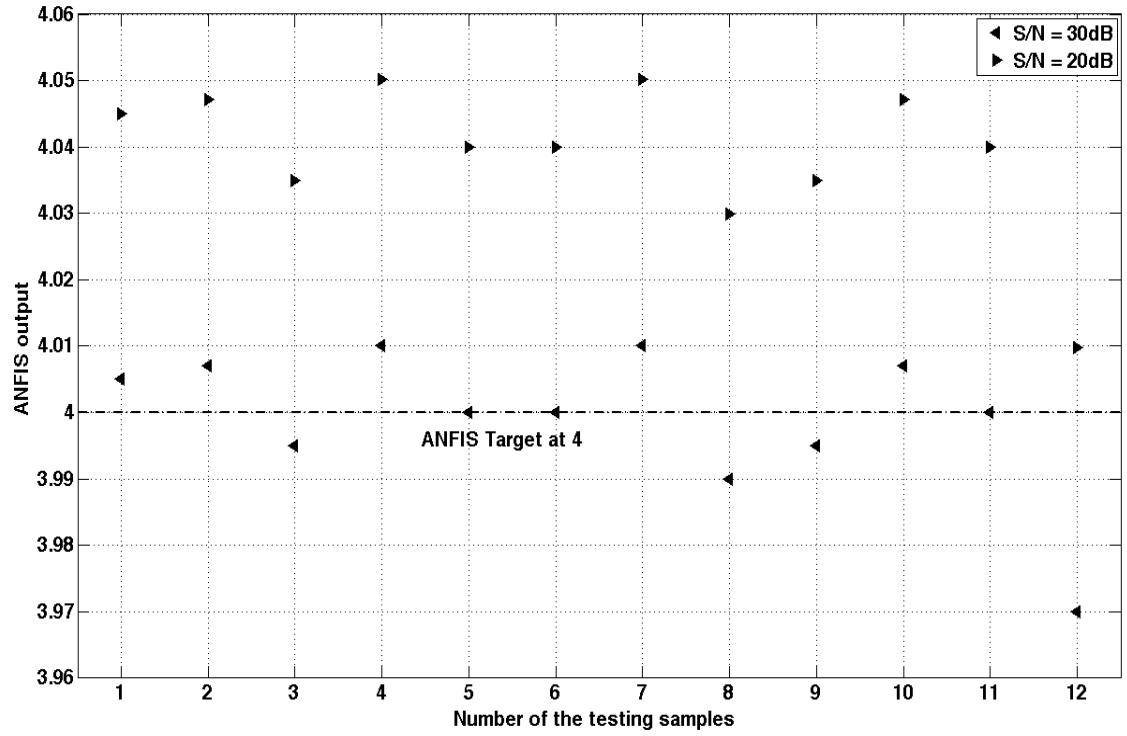


Figure 5-12 ANFIS outputs and target at T1 or T4 Gate Drive O-C fault conditions

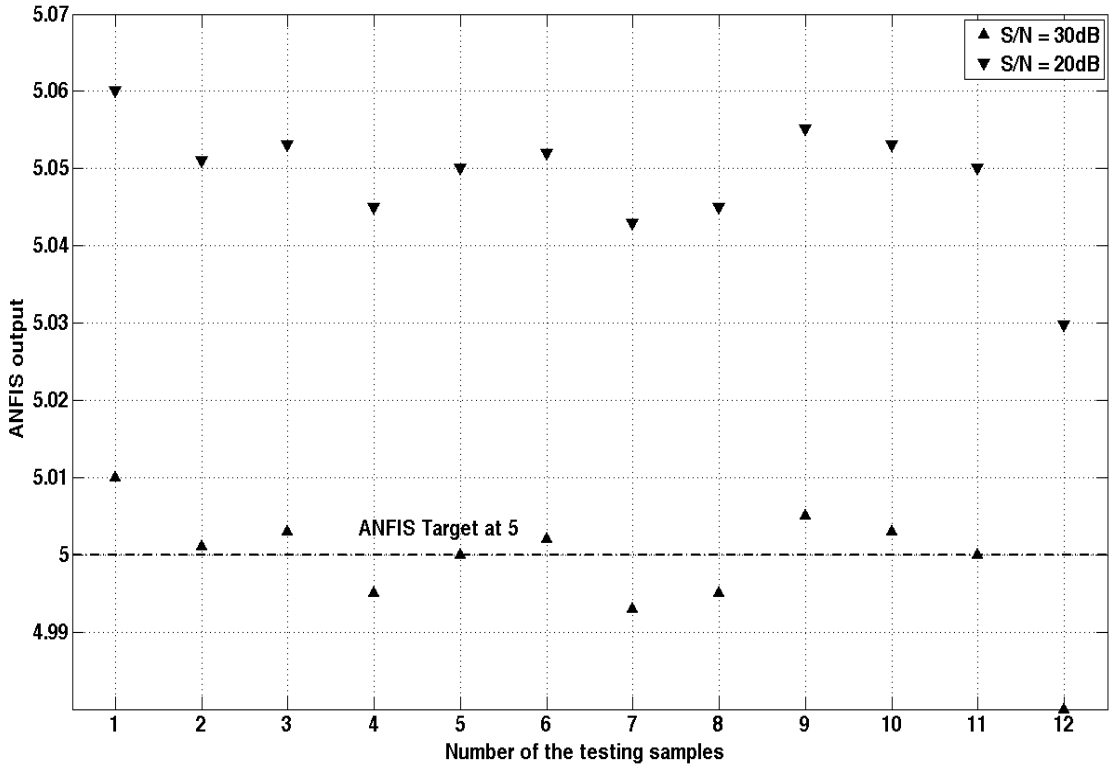


Figure 5-13 ANFIS outputs and target at T2 or T3 Gate Drive O-C fault conditions

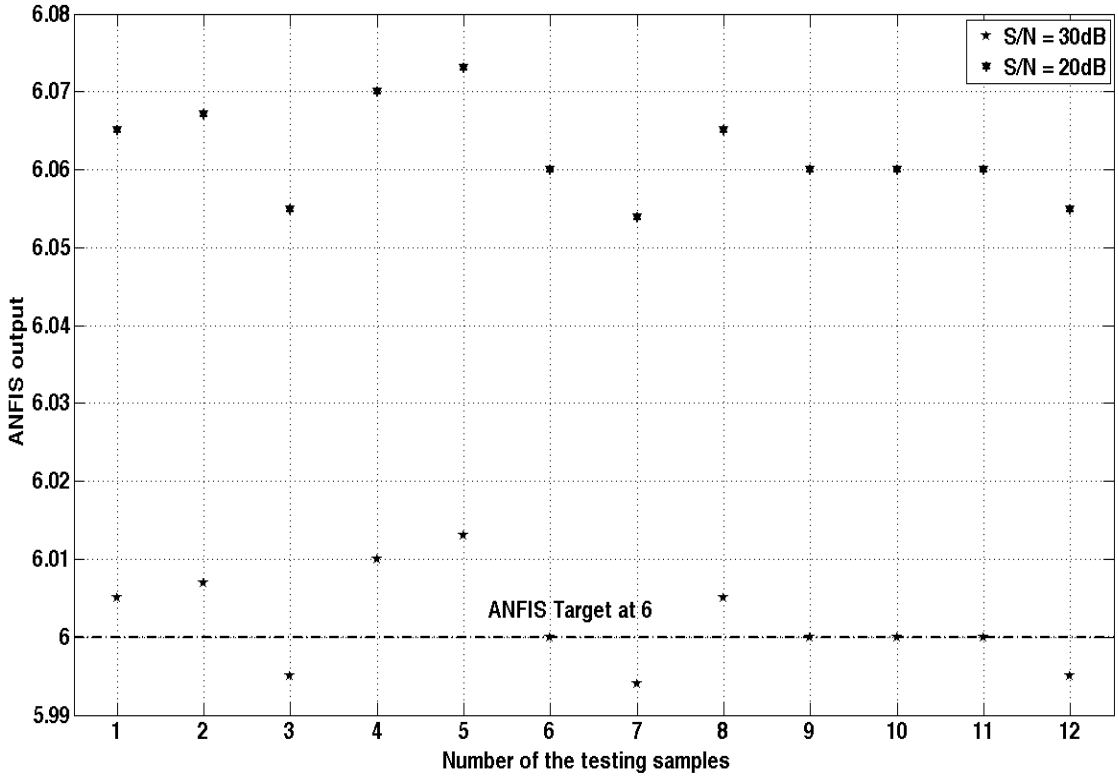


Figure 5-14 ANFIS outputs and target at T1 or T4 IGBT O-C fault conditions

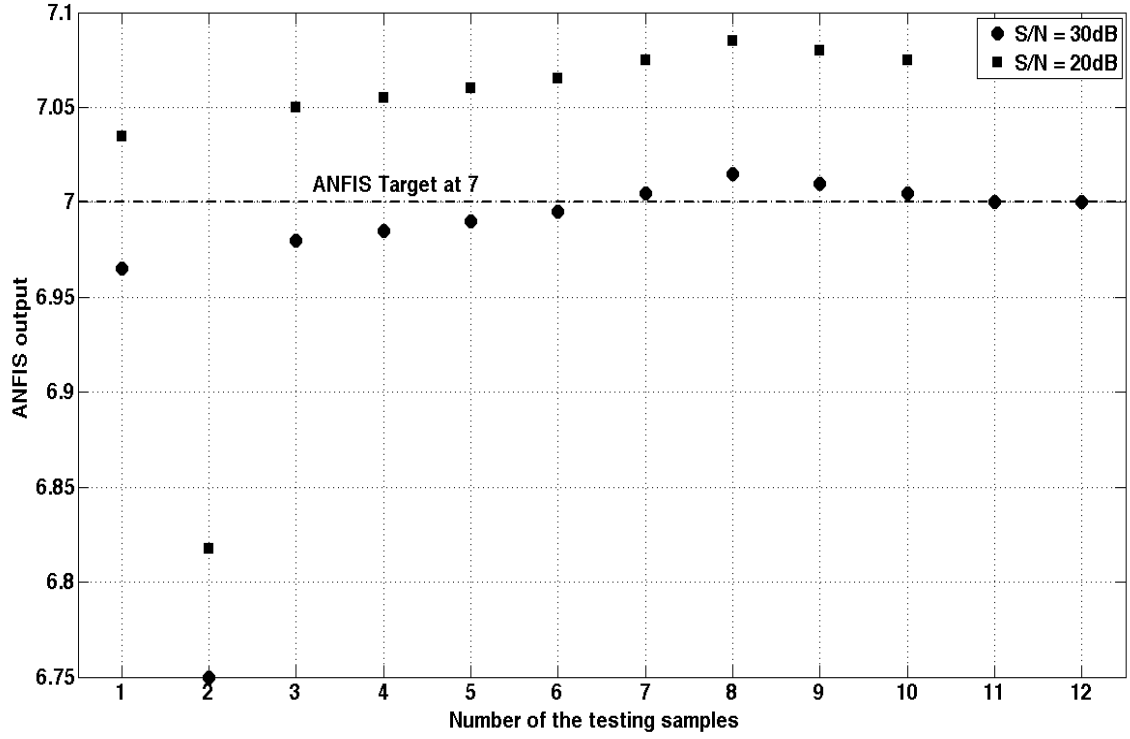


Figure 5-15 ANFIS outputs and target at T2 or T3 IGBT O-C fault conditions

Table 5-5 provides the maximum absolute errors (MAE) between the ANFIS targets ($ANFIS_T$) and outputs ($ANFIS_O$) for the previous testing situations at the normal and fault conditions. Thus,

$$MAE = \left| \; ANFIS_T - ANFIS_O \; \right| \tag{5.4.2}$$

The percentage maximum error is provided in the last column of Table 5-5 and it is calculated as follows:

$$\%E = \frac{MAE}{ANFIS_T} * 100\% \tag{5.4.2}$$

5.5 Summary

Table 5-5 and Figures 5-7 to 5-15 have established that the proposed ANFIS fault diagnostic unit is an accurate and robust detector, classifier and locator for the O-C faults of the power converters in its three main circuits; three-phase rectifier, boost chopper and single-phase inverter circuits. The output of the ANFIS network is utilized as index to identify the O-C faults. Then, it classifies and locates the O-C fault within the converter according to its value. The maximum %E is 12% which meets the industry recommendations

Even though the proposed ANFIS diagnostic unit is evaluated in simulation environment in this chapter, the selected input features for the ANFIS unit (Table 5-2) are chosen according to the experimental analysis which comprehensively indicated in chapter 4.

Furthermore, the proposed ANFIS unit is validated under the inclusion of the noise in the testing data in order to represent the non-ideal behavior of the operation conditions that could take place in the experimental environment.

Table 5-5 The MAE and %E for the testing conditions

Target Index	Identification	MAE	%E
0	Normal conditions	0.06	NA[(1)]
1	O-C fault conditions in the rectifier circuit	0.12	12%
2	T O-C fault conditions	0.09	4.5%
3	D O-C fault conditions	0.1	3.33%
4	T1 or T4 Gate Drive O-C fault conditions	0.05	1.25%
5	T2 or T3 Gate Drive O-c fault conditions	0.06	1.2%
6	T1 or T4 IGBT O-C fault conditions	0.075	1.25%
7	T2 or T3 IGBT O-C fault conditions	0.25	3.5%

[(1)] NA: Non-Applicable because $ANFIS_T$ equal to zero at normal conditions

Chapter 6: ANFIS-Based Diagnosis for DC Capacitor Banks Faults in Power Converter

6.1 Preface

The DC capacitor banks in the power converter have a relatively short lifetime compared to power semiconductor devices. Moreover, the capacitors are responsible for more than half of the failures in power converters as shown in Figure 6-1 [55]. DC capacitor bank failures can be divided into total breakdowns, capacitor aging and open circuit faults. In the case of a total breakdown, the converter usually shuts down because of an insufficient smoothing effect in the DC link. In the other two cases, certain limits should be defined, and a preventive maintenance is necessary to avoid further growing of their effects and subsequent total breakdown [56-58].

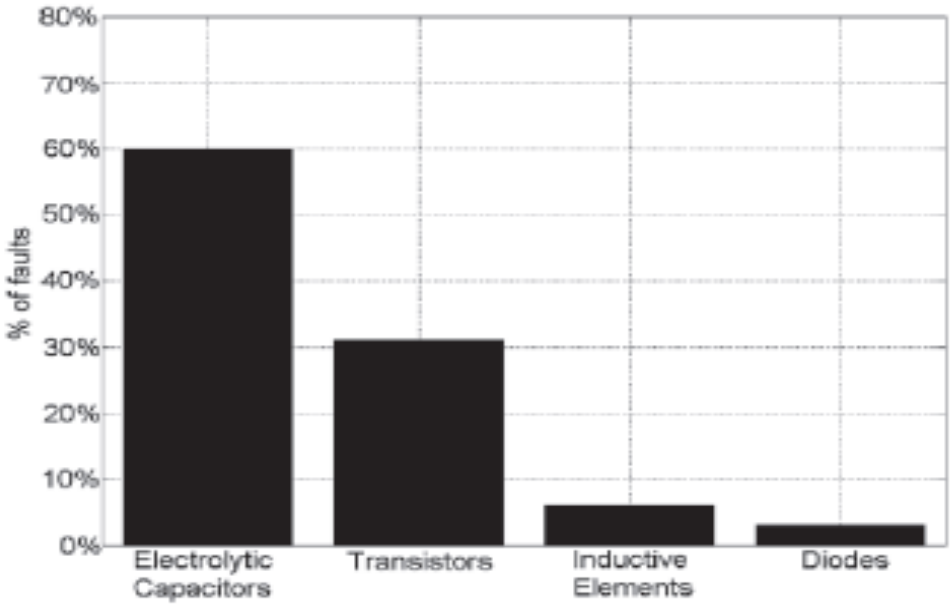


Figure 6-1 Distribution of failures for each power component in power converters, at Ta = 25^0C [55].

Capacitor aging occurs with the evaporation of electrolyte over time. Aging results in increased current ripple and increased temperature within the capacitor. In a simple equivalent model, the aging mechanism causes an increase in the equivalent series resistance (ESR) and a decrease in the capacitance (C). Manufactures define the end-life limit of a capacitor as the point in time when the ESR doubles or C changes by 20% relative to its initial values [58-59]. ESR is the sum of the resistance due to aluminum oxide, electrolyte, spacer, and electrodes (foil, tabbing, leads, and ohmic contacts). The electrolytic capacitor impedance Z can be represented as follows:

$$Z = ESR + j\omega ESL + \frac{1}{j\omega C} \tag{6.1.1}$$

where ω is 2πf where f is the system operating frequency, and ESL is equivalent series inductance. ESL is mainly caused by the capacitor leads, which are cut as short as possible in the practical circuit implementation. The value of the ESL is much smaller than the ESR and could be neglected. At the switching frequency of the converters, the impedance of the electrolytic capacitors is then approximately equal to ESR. As a result, ESR is very significant in representing the DC capacitor banks, as well as in determining the self-heating of the capacitor banks and, so, indirectly, their lifetimes.

Aluminum electrolytic capacitors have a liquid electrolyte characterized by material properties of conductivity and viscosity. Both conductivity and viscosity change with temperature. In the system under the study, the temperature of the environment inside the converter is relatively fixed during the operation due to the ventilation in converter, where small fans are automatically turned on when the temperature rises beyond a certain

limit. As a consequence, the changes in the ESR are mostly caused due to the degradation process of the capacitor banks.

When an open circuit fault occurs in the capacitor bank, it is equivalent to disconnecting one or more capacitors from a capacitor bank. This causes a decrease in the equivalent capacitance and an increase in the ESR. However, the change occurs very rapidly in comparison with capacitor aging, and the rate of change depends on the number of open circuit capacitors.

Several research works have proposed the measurement of ESR as a mean of failure detection in the capacitor banks. The measurement methods for ESR can be categorized into offline and online techniques. The offline ESR measurement methods are easier to use and less expensive [57], [60-63]. However, these methods are inconvenient, since the capacitor needs to be disconnected from the converter.

In order to avoid interrupting the system operation when measuring the ESR, several online techniques have been presented. An online technique is given in [64], where an additional hardware circuit is required to identify the increase of the ESR in the real time. Another research [65] proposed injection of a controlled AC current into the converter input. This controlled current induces an AC voltage ripple component in the dc-link capacitor. The instantaneous AC current and voltage components in the DC output side are then extracted for the ESR estimation. Finally, another online method in [66] detects the variations in the ESR and capacitance of aluminum electrolytic capacitors in uninterruptable power supplies by measuring the capacitor current and voltage ripples.

The aforementioned online techniques require either additional hardware or sensors, which may not be available in commercial power converters that are used in

distributed generation applications. These hardware and sensors include costs and expenses, which are critical for such commercial systems.

This chapter presents an Adaptive Neuro Fuzzy Inference System - based diagnostic algorithm for the DC capacitor bank faults in the power converter using only the measurements of the output voltages of the capacitor banks, as well as the input voltage of the converter. The ANFIS diagnostic unit identifies the capacitor aging and the O-C faults in the capacitor banks. Section 6.2 provides a detailed description of the DC capacitor banks configurations in the power converter under study. Then, Section 6.3 introduces the methodology, which is developed to investigate the effect of the capacitor bank faults on the behavior of their measured output voltages. After that, the proposed ANFIS-based diagnostic unit is demonstrated by MATLAB/Simulink in Section 6.4. Then, the evaluation for the ANFIS diagnostic unit is provided in Section 6.5. Finally, Section 6.6 presents the summary of the proposed diagnostic algorithm in this chapter.

6.2 Capacitor Banks Configuration

There are two DC capacitor banks in the power converter under study, as shown in Figure 5-5: one at the output of the rectifier C_1 and the other at output of the boost chopper C_2. The converter uses electrolytic DC capacitors of 1000 μF/350V. The capacitors have an ESR of 200 mΩ at normal conditions. The first DC filter bank contains three parallel capacitors in series with other three paralleled capacitors. The second bank contains five paralleled capacitors in series with other five paralleled capacitors. Therefore, under normal conditions:

$$C_1 = 1000 * 3/2 = 1500\ \mu F, \quad ESR_1 = 200 * 2/3 = 133.33\ m\Omega, \tag{6.2.1}$$

$$C_2 = 1000 * 5/2 = 2500\ \mu F, \quad ESR_2 = 200 * 2/5 = 80\ m\Omega, \tag{6.2.2}$$

6.3 Fault Diagnostic Methodology of the Capacitor Banks

During the deterioration process, as well as the O-C fault in the capacitor bank, the ESR increases and the capacitance decreases. This results in increasing the ripple of the output voltage of the capacitor banks.

Since the capacitor bank C_1 is connected to the output of the three-phase rectifier, which is driven by a three-phase supply, the main harmonic component of the ripple of the output rectifier voltage, V_R, is $6f_i$, where f_i is the input voltage frequency. On the other hand, the capacitor bank C_2 is connected to the output of the boost chopper, as well as the input of single-phase inverter. Therefore, the main harmonic component of the ripple of the output boost chopper voltage, V_B, is $2f_o$, where f_o is the grid voltage frequency. Consequently, in order to investigate the aging processes or the O-C faults of the two-capacitor banks, a Fast Fourier Transform (FFT) is performed to estimate the 6^{th} harmonic component of the ripple in V_R, denoted by V_1. Similarly, the FFT is also used to estimate the 2^{nd} harmonic component of the ripple in V_B, denoted by V_2.

6.3.1 Factors influencing the ripple of the capacitor banks output voltage

There are two main factors affecting the ripple values of the output voltage of the capacitor banks: the ripple frequency and loading condition.

6.3.1.i The effect of the frequency on the ripple amplitude

As the frequency of the ripple increases, the ripple amplitude of the capacitor bank output voltage decreases. This is due to the reduction of the allowable discharge time of the capacitor bank during the increase of the frequency.

6.3.1.ii The effect of the loading condition on the ripple amplitude

As the loading of the system increases, the ripple amplitude of the capacitor bank output voltage increases. This is due to the rise of the rate of the discharge of the capacitor bank during the increase of the loading current.

6.3.2 Ripple amplitude behaviors in the capacitor banks

Since there are two capacitor banks in the power converter under study, their output voltage ripples are investigated as follows.

6.3.2.i V_1 amplitude behavior for capacitor bank C_1

In the system under study, the input frequency f_i of the converter is varied from 20 to 80 Hz and the input three-phase RMS voltage V_S changes from 100 to 350 V depending on the wind speed. Moreover, the maximum power point tracking algorithm is implemented in this system. Accordingly, the loading of the converter increases with the increase of the input frequency. The behavior of the V_1 amplitude with the increases in both the input frequency and loading conditions is presented in Figure 6-2. The figure is developed under the normal situations, where the amplitude of V_1 is plotted versus the input voltage V_S. As shown in Figure 6-2, there are two distinguished regions in the V_1 amplitude behavior with the increases in both the input frequency and loading conditions, which have opposite influences on the amplitude. The first one is from 100 V to

approximately 180 V, where V_1 increases with the increase of V_S. However, the latter one is from 180 V to 350 V where V_1 is decreasing with the increase of V_S. In the first region, the increase of the loading condition has more powerful influence on V_1 than that of the input frequency, so V_1 amplitude increases with the increase of V_S. On the other hand, in the second region, the increase of the input frequency has the dominant effect on V_1, thus V_1 amplitude decreases with the increase of V_S.

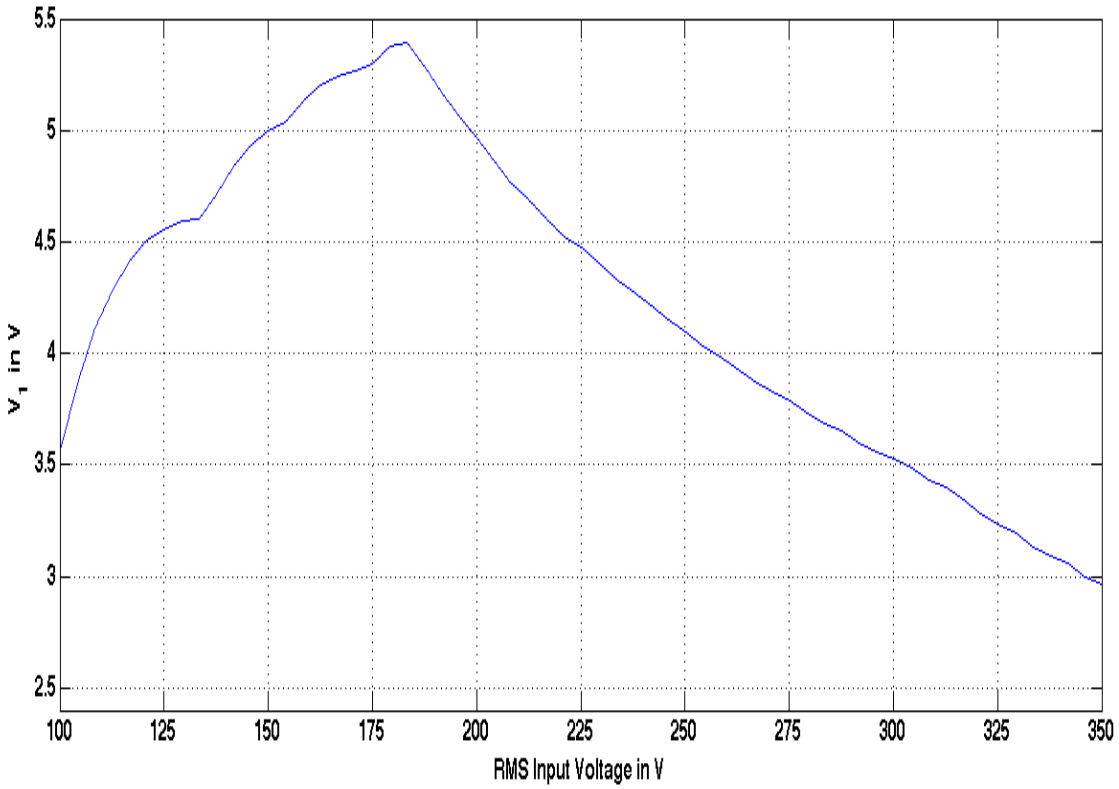


Figure 6-2 V_1 versus V_S at normal situations

6.3.2.ii V_2 amplitude behavior for capacitor bank C_2

The ripple frequency of the output voltage of C_2 is directly related to the grid frequency f_o. Moreover, f_o is fixed at 60 Hz regardless of the loading conditions.

Therefore, the loading condition becomes the sole source of influence on the V_2 amplitude behavior. The V_2 amplitude behavior versus V_S is given in Figure 6-3 at normal situations. As shown in Figure 6-3, there are two distinguished regions in the V_2 amplitude behavior too. The first one is form 100 V to approximately 310 V where V_2 increases with the loading. The latter one is from 310 V to 350 V, where V_2 becomes constant due to the fixed loading conditions in this region according to the MPPT algorithm implemented in this system.

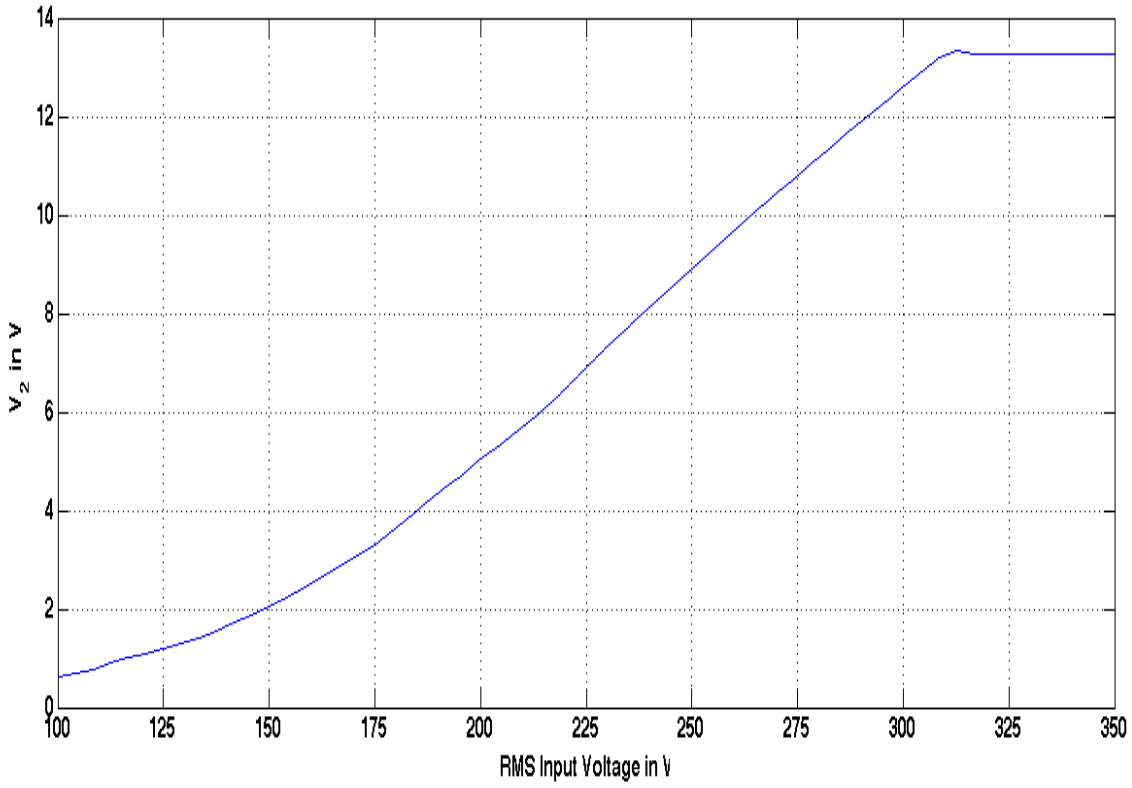


Figure 6-3 V_2 versus V_S at normal situations

6.3.3 Fault detection and classification of the capacitor banks

After the previous analysis for the output voltage of the capacitor banks in the power converter, fault detection and classification algorithms for the capacitor banks can be proposed as follows.

6.3.3.i Capacitor aging diagnosis

In order to investigate the aging of the capacitor banks, V_1 and V_2 are calculated at the end-life states of the two-capacitor banks and they are denoted by V_{1th} for capacitor bank C_1 and V_{2th} for capacitor bank C_2. Therefore, the new values of C_1 and ESR_1 at the capacitor aging of the first capacitor bank become as follows:

$$C_{1ag} = m_1 C_{1n} = 0.8 C_{1n} = 0.8 * 1500 = 1200 \mu F , \quad (6.3.1)$$

$$ESR_{1ag} = n_1 ESR_{1n} = 2 ESR_{1n} = 2 * 133.33 = 266.66 m\Omega , \quad (6.3.2)$$

where C_{1ag} and ESR_{1ag} are the series capacitance and the ESR of the first capacitor bank at the end-life aging condition respectively. On the other hand, C_{1n} and ESR_{1n} are the series capacitance, and the ESR of the first capacitor bank at the normal condition respectively. Finally, n_1 and m_1 are the variation ratios for C_1 and ESR_1, and they are equal to 0.8 (representing 20% decrease in C) and 2 (representing 200% increase in ESR) at the aging state respectively as mentioned previously.

Similarly, the new values of C_2 and ESR_2 at the capacitor aging of the second capacitor bank become as follows:

$$C_{2ag} = m_2 C_{2n} = 0.8 C_{2n} = 0.8 * 2500 = 2000 \mu F \ , \tag{6.3.3}$$

$$ESR_{2ag} = n_2 ESR_{2n} = 2 ESR_{2n} = 2 * 80 = 160 m\Omega \ , \tag{6.3.4}$$

where C_{2ag} and ESR_{2ag} are the series capacitance, and the ESR of the second capacitor bank at the aging condition respectively. On the other hand, C_{2n} and ESR_{2n} are the series capacitance, and the ESR of the second capacitor bank at the normal condition respectively. Finally, n_2 and m_2 are the variation ratios for C_2 and ESR_2 and they are also equal to 0.8 and 2 at the aging state respectively.

The behavior of V_{1th} versus V_S resembles that of Figure 6-2. Similarly the behavior of V_{2th} versus V_S resembles that of Figure 6-3. Consequently, the relationship between V_{1th} and V_S can be linearly interpolated by using the curve fitting techniques in order to be utilized in the fault detection algorithm for the capacitor aging of C_1. Therefore, the relationship between V_{1th} and V_S is developed in MATLAB/Simulink and can be estimated as follows:

$$\hat{V}_{1th} = \begin{cases} 0.029 * V_S + 2.1 & for\ 100 \le V_S \le 180 \\ -0.016 * V_S + 9.9 & for\ 180 < V_S \le 350 \end{cases} \tag{6.3.5}$$

where $\hat{V}_{1th}$ is the estimated value for V_{1th} according to V_S. Similarly for the relationship between V_{2th} and V_S, which is also linearly interpolated, and V_{2th} can be estimated according to V_S as follows:

$$\hat{V}_{2th} = \begin{cases} 0.086 * V_S - 10 & for\ 100 \le V_S \le 310 \\ 17 & for\ 310 < V_S \le 350 \end{cases} \quad (6.3.6)$$

where $\hat{V}_{2th}$ is the estimated value for V_{2th} according to V_S. Finally, a percentage value of the measured V_1 over $\hat{V}_{1th}$ and a percentage of the measured V_2 over $\hat{V}_{2th}$ are evaluated as direct inputs to the proposed fault diagnosis algorithm. Thus, the percentage values can be calculated as follows:

$$\%V_1 = \frac{V_{1m}}{\hat{V}_{1th}} * 100\% \quad (6.3.7)$$

$$\%V_2 = \frac{V_{2m}}{\hat{V}_{2th}} * 100\% \quad (6.3.8)$$

where V_{1m} is the measured V_1 value at the current situation, and V_{2m} is the measured V_2 value at the current situation.

6.3.3.ii Capacitor O-C fault diagnosis

The significant difference between the capacitor aging and capacitor O-C fault is the rate of change of V_1 and V_2 during the two fault conditions. The rate of change of V_1 and V_2 during the capacitor aging is very low due to the slow variation of the capacitance and ESR during the aging. On the other hand, the sudden detachment of number of

capacitors from the capacitor bank causes a rapid variation of the bank capacitance and ESR that leads to a faster rate of change in V_1 or V_2 during the capacitor open circuit faults. As a result, the voltage differences between two successive samples of the V_1 and V_2 are calculated, and these differences are used as direct inputs to the proposed fault diagnosis algorithm. Thus, the voltage differences are evaluated as follows:

$$\Delta V_1 = V_{1m}(k) - V_{1m}(k-1) \tag{6.3.9}$$

$$\Delta V_2 = V_{2m}(k) - V_{2m}(k-1) \tag{6.3.10}$$

where k is the sample index. The amount of the delay between the present and the previous values of V_{1m} and V_{2m} depends on the required time by the signal processing calculations to calculate the steady state values of the V_{1m} and V_{2m} during the running of the power converter within the range of the input frequency. According to the minimum input frequency, i.e. 20 Hz, it is found that 0.05 sec is sufficient to evaluate the present and the previous values of V_{1m} and V_{2m}.

6.4 ANFIS Fault Diagnostic Algorithm

A decision-making unit for the diagnoses of capacitor bank faults is developed with ANFIS algorithm in this chapter. The ANFIS diagnostic unit is used to detect, classify, and locate the faults of the capacitor banks in the power converter under study.

The ANFIS decision-making network has five inputs, which are given in Table 6-1. It has one output whose value is used as an index in order to identify either there is

normal or fault condition for the capacitor banks. Then, during the fault conditions, it classifies the faults types (either capacitor aging or O-C fault) and also locates the fault (either in C_1 or C_2) as provided in Table 6-2. The proposed ANFIS network is presented with its inputs and output indices in Figure 6-4.

Data sets are established in MATLAB/Simulink in order to train and test the proposed ANFIS diagnostic unit at the normal and the fault conditions from input frequency 20 Hz to 80 Hz in steps of 1 Hz. The fault conditions are carried out at the capacitor aging and the open circuit fault for the two-capacitor banks. There are a total of 732 data pairs created in order to train and test the proposed ANFIS-fault diagnostic unit.

Table 6-1 The inputs of the ANFIS diagnostic unit

Input No.	Identification
Input 1	V_S; the RMS value of the input three-phase line voltage
Input 2	$\%V_1$; the percentage value of the measured V_1 over $\hat{V}_{1th}$
Input 3	$\%V_2$; the percentage value of the measured V_2 over $\hat{V}_{2th}$
Input 4	ΔV_1; the voltage difference between two successive samples of the V_1
Input 5	ΔV_2; the voltage difference between two successive samples of the V_2

Table 6-2 The output indices of the ANFIS diagnostic unit

Output Index	Identification
0	Normal conditions
1	Capacitor aging for C_1
2	Capacitor aging for C_2
3	O-C fault for C_1
4	O-C fault for C_2

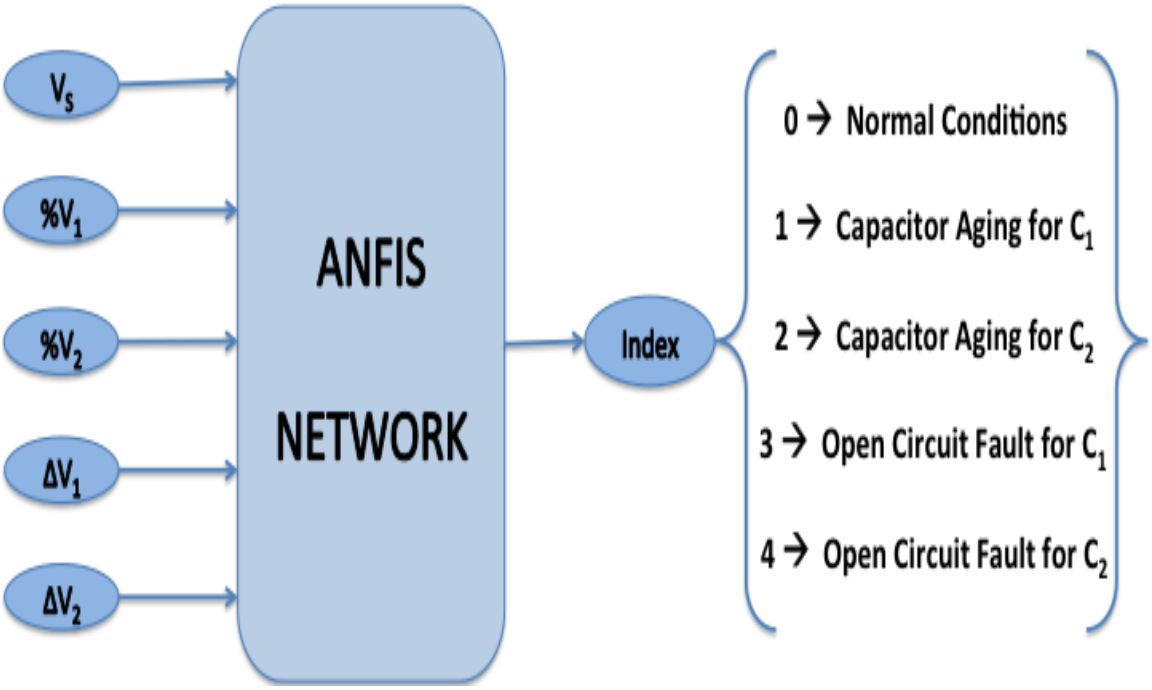


Figure 6-4 ANFIS network with its inputs and output indices for the capacitor banks fault in the power converter

The established data set pairs are carried out at various situations of normal and fault conditions where the m_1, m_2, n_1, and n_2 are chosen to represent different behaviors of the aging process of the capacitor banks as indicating in the following:

- Normal conditions, where $m_1 = n_1 = m_2 = n_2 = 1$.
- Normal conditions, where $m_1 = m_2 = 0.9$ and $n_1 = n_2 = 1.5$
- Capacitor aging for C_1, where $m_1 = 0.65$ and $n_1 = 2.75$, while $m_2 = n_2 = 1$
- Capacitor aging for C_1, where $m_1 = 0.55$ and $n_1 = 3.25$, while $m_2 = n_2 = 1$
- Capacitor aging for C_2, where $m_2 = 0.65$ and $n_2 = 2.75$, while $m_1 = n_1 = 1$
- Capacitor aging for C_2, where $m_2 = 0.55$ and $n_2 = 3.25$, while $m_1 = n_1 = 1$
- O-C fault for C_1, where one capacitor is disconnected from the bank
- O-C fault for C_1, where two series capacitors are disconnected from the bank
- O-C fault for C_1, where two parallel capacitors are disconnected from the bank
- O-C fault for C_2, where one capacitor is disconnected from the bank
- O-C fault for C_2, where two series capacitors are disconnected from the bank
- O-C fault for C_2, where two parallel capacitors are disconnected from the bank

80% of the data sets are selected randomly and used to train the proposed ANFIS network. On the other hand, a 20% reminder is utilized in testing and verifying the performance of the ANFIS network.

Four membership functions are selected for each of the 5 inputs. The type of the input membership functions is chosen to be Gaussian membership function. On the other hand, the type of the output membership functions is selected to be linear membership

function. The chosen types for the input and output membership functions achieve training error 6.9% which is the minimum among the other membership functions types.

6.5 ANFIS Fault Diagnosis Evaluation

In order to verify the validity of the proposed trained ANFIS system, 20% of the established data sets are used to test the ANFIS network.

White Gaussian noise of signal-to-noise ratio (SNR) of 25 dB and 15 dB are also added to the testing data in order to represent the non-ideal operating conditions of the power converter, as well as the measurements errors due to the converter sensors and the interference of the signals inside the converter.

Figures 6-5 to 6-16 provide the ANFIS outputs at the stated testing conditions and compare these outputs with the desired target indices as provided in Table 6-2. The ANFIS target indices are depicted as dashed straight lines in each figure. Table 6-3 provides the MAE and %E between the ANFIS outputs and targets for the previous testing situations at the normal and fault conditions.

Furthermore, it is found that the proposed ANFIS unit provides false diagnostic decisions when a pulse noise is introduced to the testing data with 25% of the input signal amplitudes.

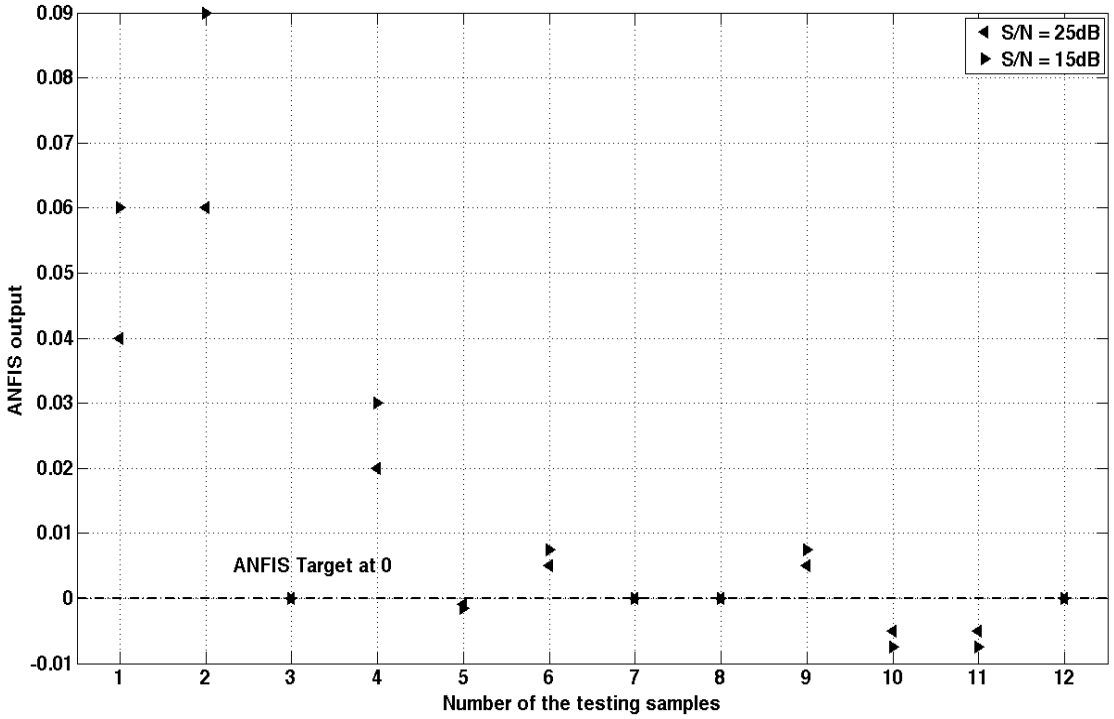


Figure 6-5 ANFIS outputs and target at normal conditions where $m_1=n_1=m_2=n_2=1$

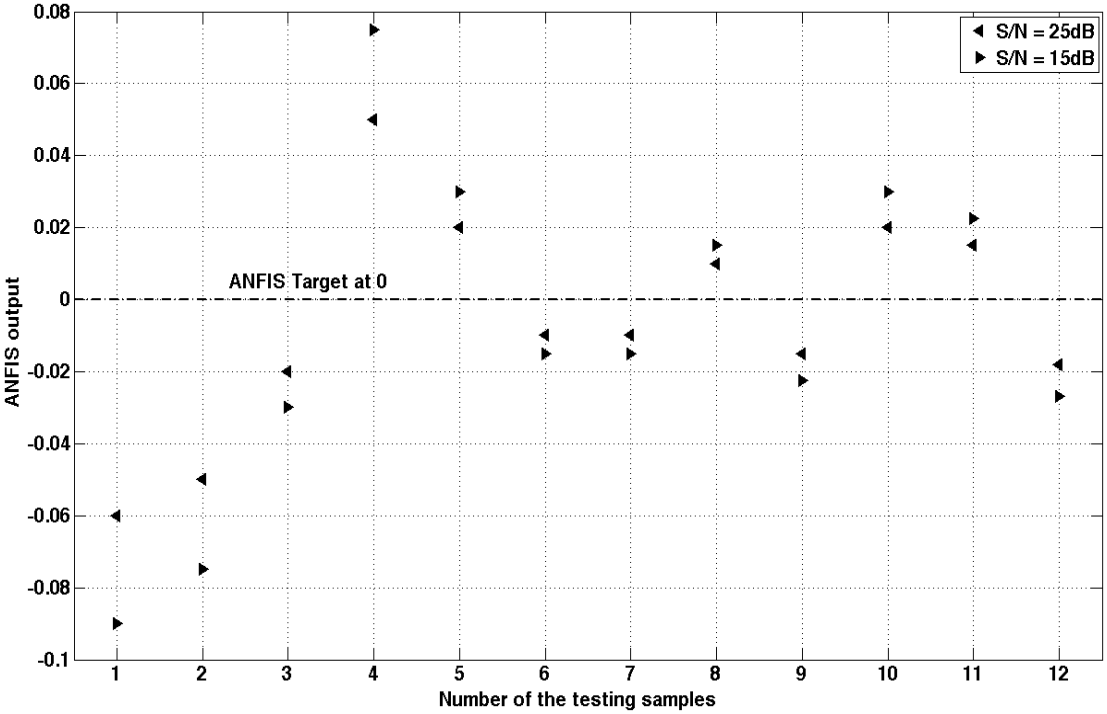


Figure 6-6 ANFIS outputs and target at normal conditions where $m_1 = m_2 = 0.9$ and $n_1 = n_2 = 1.5$

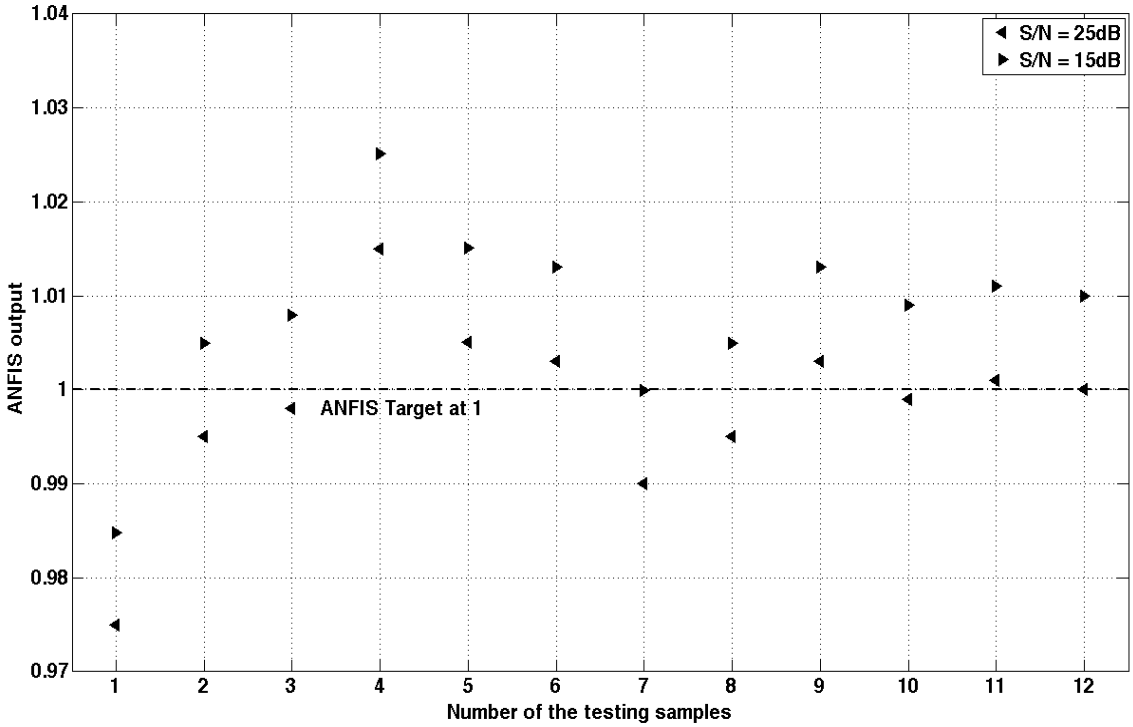


Figure 6-7 ANFIS outputs and target at capacitor aging for C_1, where $m_1 = 0.65$ and $n_1 = 2.75$, while $m_2 = n_2 = 1$

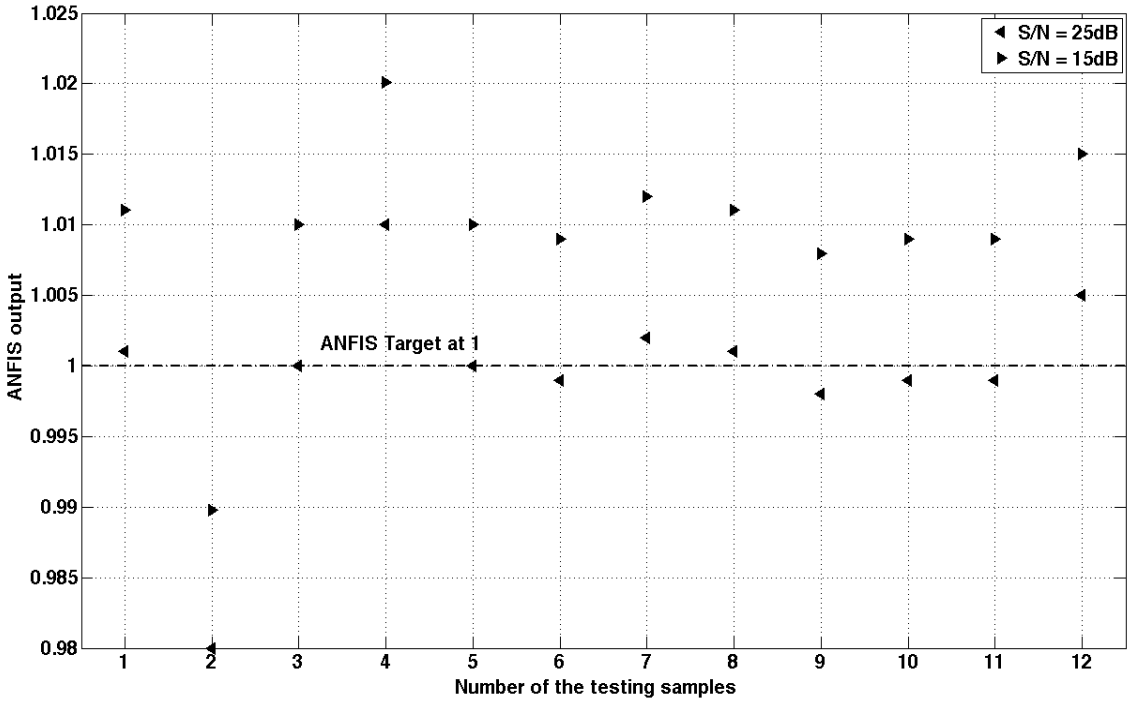


Figure 6-8 ANFIS outputs and target at capacitor aging for C_1, where $m_1 = 0.55$ and $n_1 = 3.25$, while $m_2 = n_2 = 1$

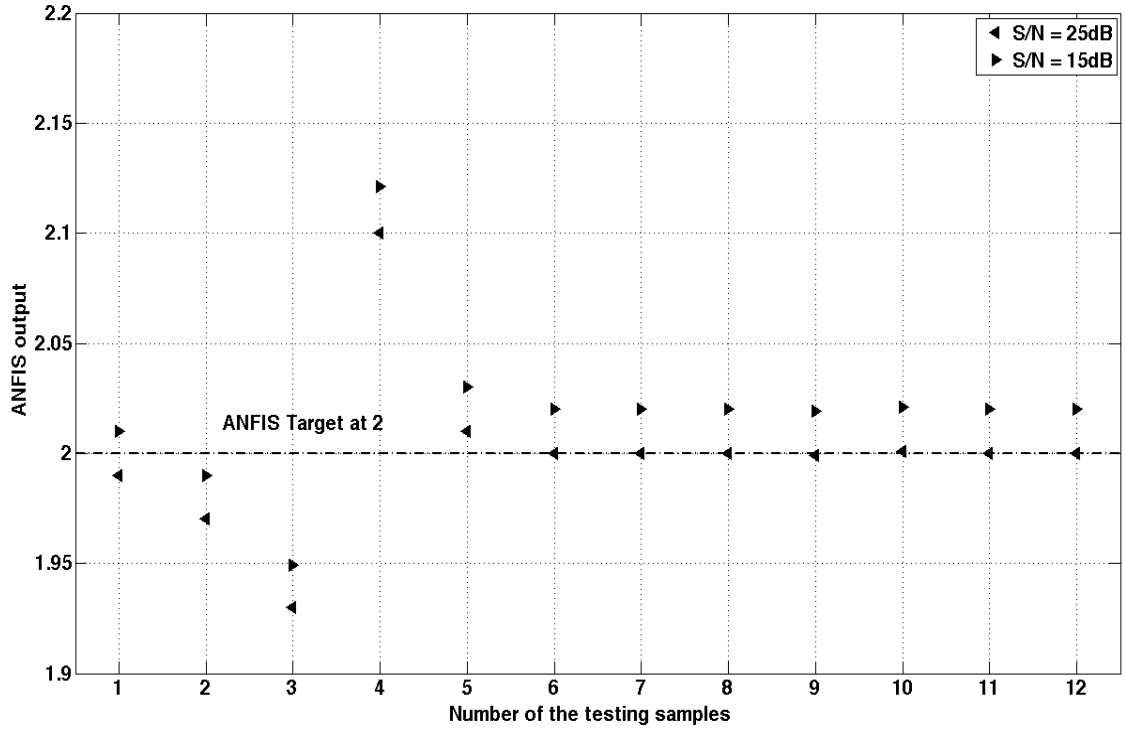


Figure 6-9 ANFIS outputs and target at capacitor aging for C_2, where $m_2 = 0.65$ and $n_2 = 2.75$, while $m_1 = n_1 = 1$

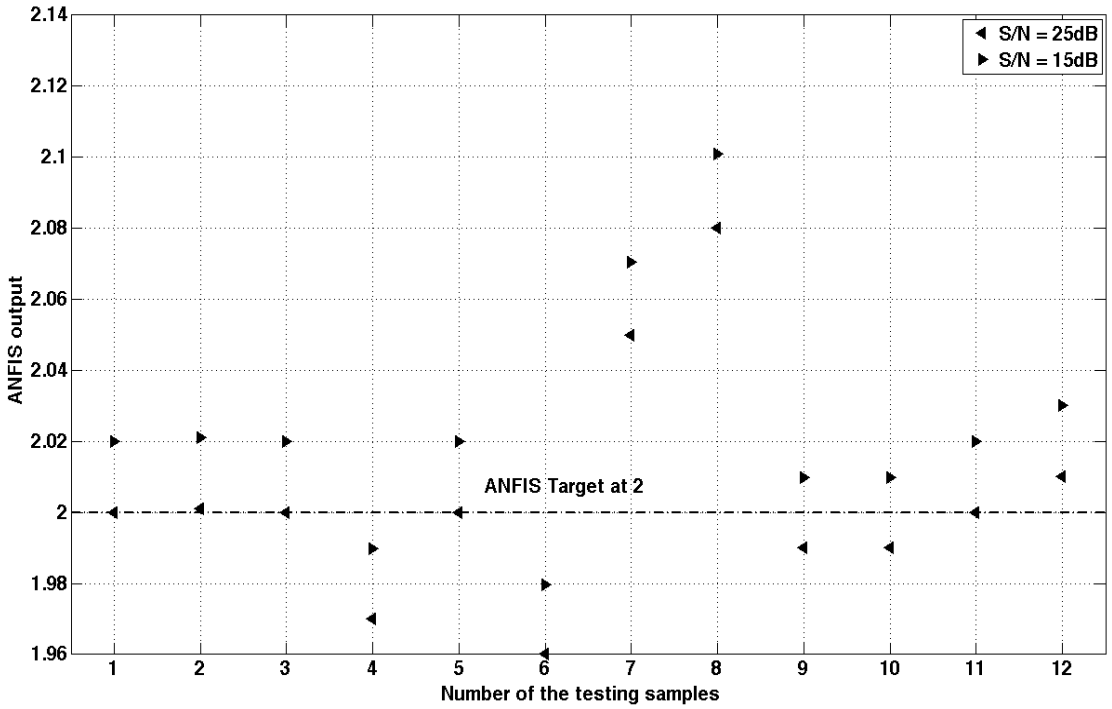


Figure 6-10 ANFIS outputs and target at capacitor aging for C_2, where $m_2 = 0.55$ and $n_2 = 3.25$, while $m_1 = n_1 = 1$

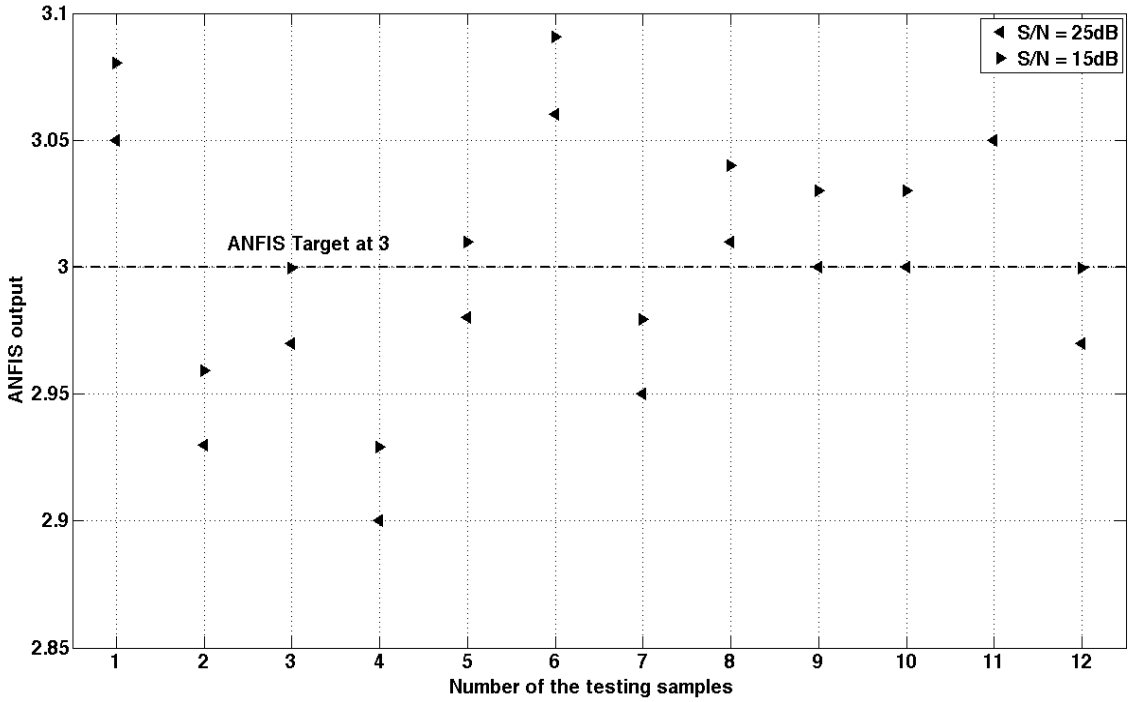


Figure 6-11 ANFIS outputs and target at O-C fault for C_1, where one capacitor is disconnected from the bank

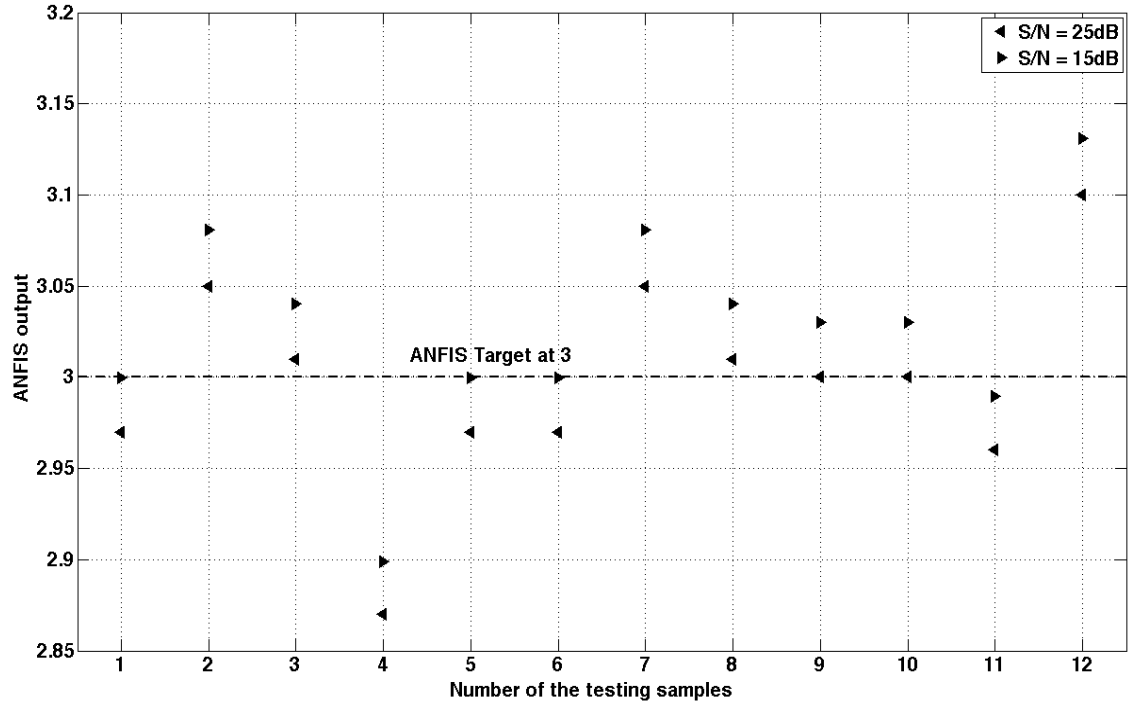


Figure 6-12 ANFIS outputs and target at O-C fault for C_1, where two series capacitors are disconnected from the bank

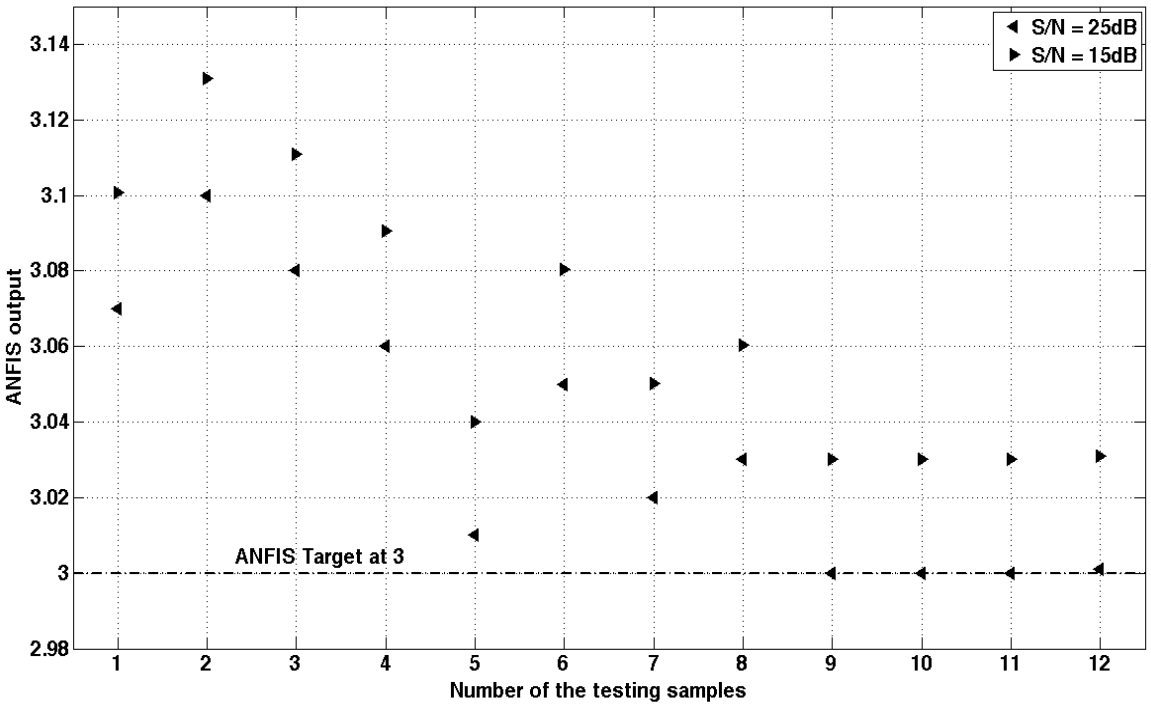


Figure 6-13 ANFIS outputs and target at O-C fault for C_1, where two parallel capacitors are disconnected from the bank

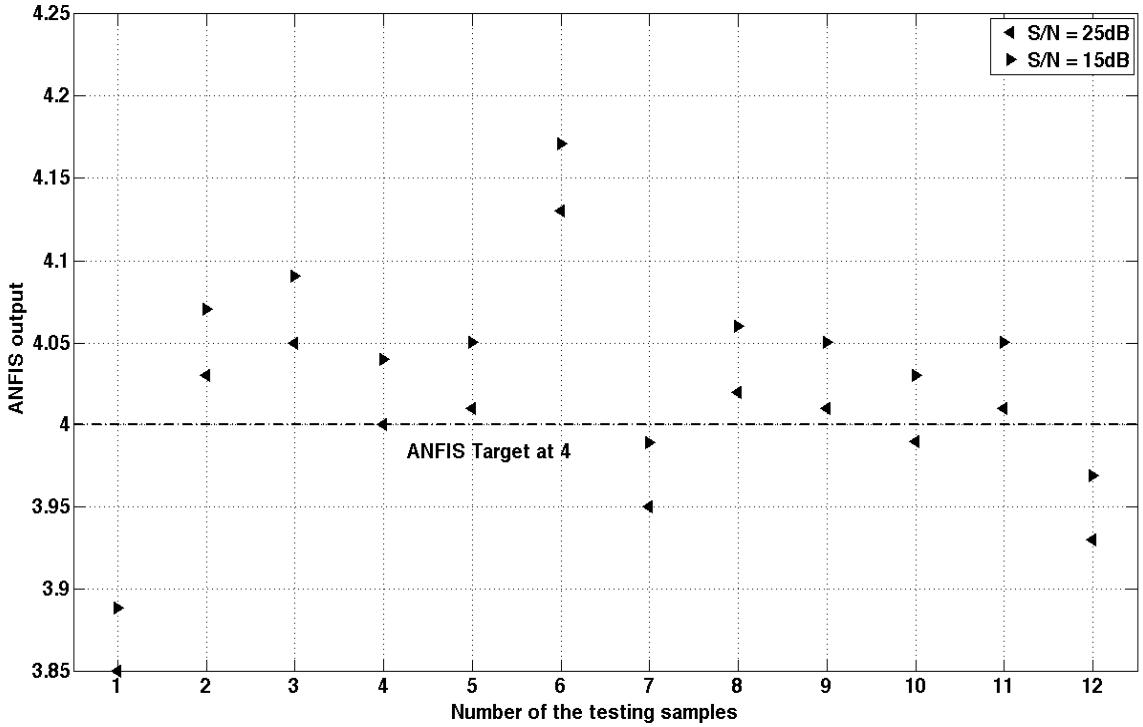


Figure 6-14 ANFIS outputs and target at O-C fault for C_2, where one capacitor is disconnected from the bank

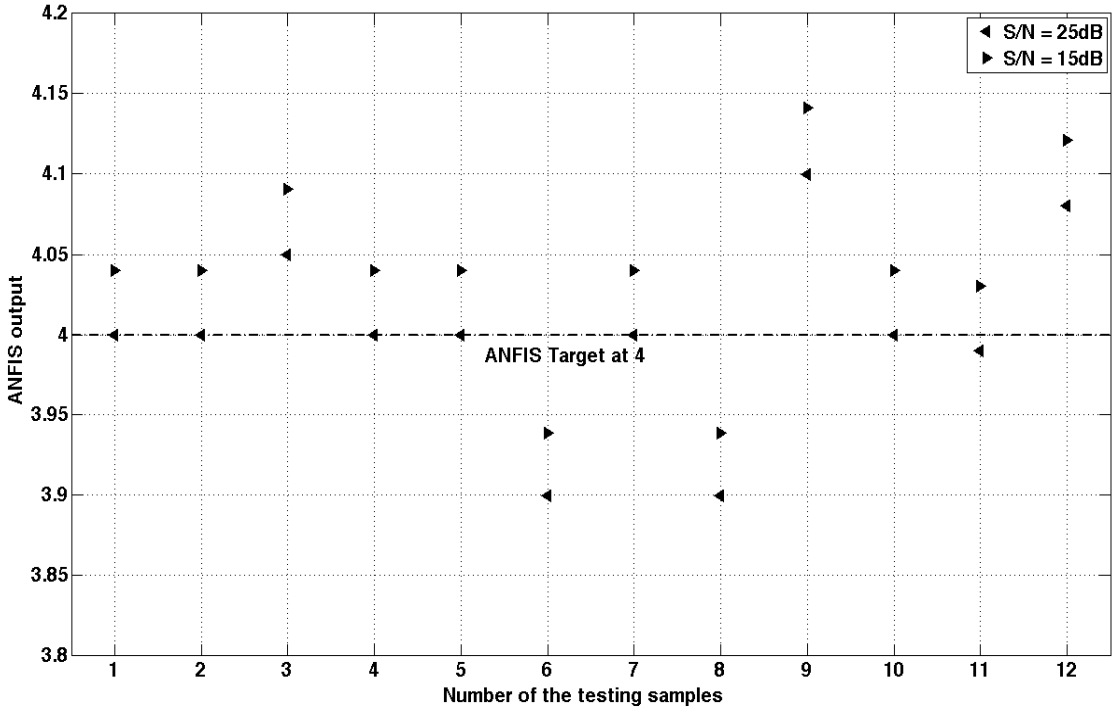


Figure 6-15 ANFIS outputs and target at O-C fault for C_2, where two series capacitors are disconnected from the bank

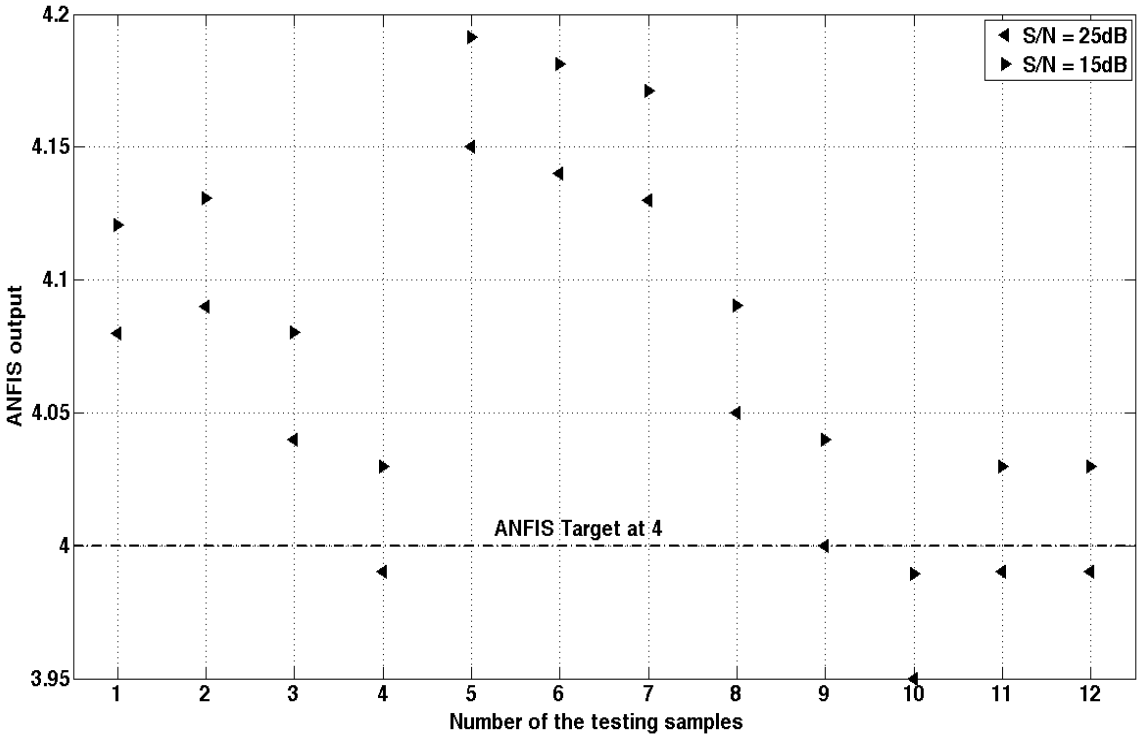


Figure 6-16 ANFIS outputs and target at O-C fault for C_2, where two parallel capacitors are disconnected from the bank

Table 6-3 The MAE and %E for the testing conditions

Target Index	Identification	MAE	%E
0	Normal conditions	0.09	NA[(1)]
1	Capacitor aging for C_1	0.025	2.5%
2	Capacitor aging for C_2	0.13	6.5%
3	O-C fault for C_1	0.14	4.67%
4	O-C fault for C_2	0.18	4.5%

[(1)] NA: Non-Applicable because $ANFIS_T$ equal to zero at normal conditions

6.6 Summary

Table 6-3 and Figures 6-4 to 6-15 have ascertained that the proposed ANFIS fault diagnostic unit is a robust and precise fault identifier for capacitor aging and O-C faults in the capacitor banks of the power converter. Moreover, it succeeds in classifying the fault type (either capacitor aging or O-C fault) and determining the fault location (either in C_1 or C_2) according to the value of its output indices at different normal and fault conditions, as well as supplying and loading conditions. The maximum %E is 6.5% which meets the industry recommendations.

Although the ANFIS diagnostic unit is developed and verified in the simulation environment in this chapter, the methodology behind the chosen input features for the ANFIS can generalized and implemented in the experimental environments.

Chapter 7: Contributions and Future Work

This chapter presents general summary and main contributions of the research work presented in this dissertation as well as the future work. The chapter is organized as follows. The summary of the dissertation is provided in Section 7.1. Section 7.2 lists the major contributions for the research in the dissertation. Finally, Section 7.3 proposes the future work for the research.

7.1 General Summary

- A brief description for the power electronic converter under study is provided with its three main circuits: three-phase uncontrolled rectifier, boost chopper, and single-phase inverter circuits, as well as the governing mathematical formulas and the control loops. This converter is a typical commercial power converter utilized for small wind turbines.
- Open Circuit (O-C) fault detection, classification and localization are provided for the three main circuits of the power converter, as well as the detection of the unbalanced input voltage to the converter by using fewer inputs than those used by the previous research. These inputs are from the available current and voltage sensors in the system under study. The proposed fault diagnoses are investigated in the simulation environment by utilizing the relationship between the sequence components of the electrical signals with their harmonic components. The proposed fault diagnostics assumed that their inputs have consistent behaviors during the faults.
- An on-line digital signal processor (DSP)-based real time fault diagnosis for the faults in the power converter under study is implemented in an

experimental environment. The experimental setup is supplied by an AC synchronous generator coupled with a DC motor. The supply for the DC motor is a variable DC supply so that the output voltage of the AC generator can be controlled by the DC motor in order to represent the variable speed characteristics of a wind turbine. The DSP board for the power converter under tests in this research is TMS320LF2407 from Texas Instruments Incorporated, with implemented switching frequency 10 kHz.

- A decision-making unit for the O-C faults in the power converter is established using the adaptive neuro-fuzzy inference system (ANFIS) network. The ANFIS diagnostic network is used to detect, classify, and locate the O-C faults of the power converters in its three main circuits according to value of the network output index.
- An ANFIS-based diagnostic algorithm for the DC capacitor faults in the power converter is developed. The ANFIS unit is responsible for fault detection, classification (either capacitor aging or O-C fault) and location (either in C_1 or C_2) according to the value of its output indices at different normal and fault conditions as well as supplying and loading conditions.

7.2 Major Contributions

- New fault diagnostic algorithms for the O-C and degradation faults in the power converters are proposed in this dissertation. These O-C faults do not trigger the standard protection systems, but rather cause system malfunction or performance degradation. The new fault diagnostic algorithms have been developed by applying the relationship between the sequence components

of the electrical signals with their harmonic components. The proposed algorithms use less number of sensors than those in the previous works. The extra sensors and hardware include additional costs and expenses according to their numbers and types. As a result, the minimization of the required sensors and hardware becomes significant for low and medium-size commercial power converters implemented in the distribution generation systems connected to small wind turbines. Consequently, the developed fault diagnosis methods can be used directly in existing power converters available on the market to achieve the required diagnosis tasks at low cost. The proposed fault diagnoses are studied and investigated in a simulation environment, then in an experimental one after taking into consideration the implementation considerations and constrains.

- Novel fault diagnostic unit is developed using the ANFIS technique for all O-C faults of power semiconductor switches in the power converter under study based on the available sensors in the system.
- Finally, a novel ANFIS-based fault diagnostic unit for the DC capacitor banks in the power converter is developed based on the measurements of the output voltages of the capacitor banks, as well as the input voltage of the converter.

7.3 Future Work

- Apply short-time FFT technique for the required inputs of the proposed fault diagnosis rather than regular FFT technique in order to achieve faster diagnostic decision in identifying the fault.

- Combine both ANFIS diagnostic units into one diagnostic scheme and implement it. As a result, this scheme becomes the main decision-making unit for the all fault diagnosis in the PECS.

References

[1] N. Mohan, T.M. Undeland, and W.P. Robbins, *Power Electronics Converters Applications and Design*, John Wiley & Sons, Inc., 2003.

[2] M. H. Rashid, *et al.*, *Power Electronics Handbook*, Elsevier Inc. 2007.

[3] http://www.greenrhinoenergy.com/renewable/wind/wind_systems.php

[4] D. Kastha and B. Bose, "Investigation of fault modes of voltage-fed inverter system for induction motor drive," *IEEE Trans. Ind. Appl.*, vol. 30, no. 4, pp.1028-1038, July / August 1994.

[5] N.M.A. Freire, J.O. Estima, and A.J.M. Cardoso, "Open-circuit fault diagnosis in PMSG drives for wind turbine applications," *IEEE Trans. Ind. Electron*, vol. 60, no. 9, pp. pp.3957-3967, Sept. 2013.

[6] Y. Guan, D. Sun and Y. He, "Mean current vector based online real-time fault diagnosis for voltage source inverter fed induction motor drives," in *Proc. IEEE IEMDC*, 2007, pp 1114-1118.

[7] B. Lu, and S. Sharma, "A literature review of IGBT fault diagnostic and protection methods for power inverters," *IEEE Trans. Ind. Appl.*, vol.45, no.5, pp.1770-1777, Sept/Oct. 2009.

[8] F.W. Fuchs, "Some diagnosis methods for voltage source inverters in variable speed drives with induction machines: a survey," in *Proc. IEEE IECON*, 2003, pp. 1378–1385.

[9] S. Shuai, P. W. Wheeler, J. C. Clare, and A. J. Watson, "Fault detection for modular multilevel converters based on sliding mode observer," *IEEE Trans. Power Electron.*, vol. 28, no. 11, pp. 4867–4872, Nov. 2013.

[10] Seshadrinath, B. Singh, and B. K. Panigrahi, “Investigation of vibration signatures for multiple fault diagnosis in variable frequency drives using complex wavelets” *IEEE Trans. Power Electron*., vol. 29, no. 2, pp. 936–945, Feb. 2014.

[11] F. Zidani, D. Diallo, M. E. H. Benbouzid, and R. Naït-Saïd, “A fuzzy based approach for the diagnosis of fault modes in a voltage-fed pwm inverter induction motor drive,” in *IEEE Trans. Ind. Electron*, vol. 55, no. 2, pp. 586–593, Feb. 2008.

[12] M. R. Mamat, M. Rizon, and M. S. Khanniche, “Fault detection of 3-phase VSI using wavelet-fuzzy algorithm,” *Amer. J. Appl. Sci.*, vol. 3, no. 1, pp. 1642–1648, 2006.

[13] F. Bo and N. Jiangchuang, “Three-phase SPWM inverter fault diagnosis based on optimized neural networks,” in *Proc. IEEE PEAM,* 2011, pp.331-335.

[14] F. Bo, D., Z. Jie, and Z. Qiang, “Three-phase inverter fault diagnosis based on optimized neural networks,” in *Proc. IEEE ICCASM*, 2010, pp.482-485.

[15] B. Xu, D. Yang, and X. Wang, “Neural network based fault diagnosis and reconfiguration method for multilevel inverter,” in *Proc. IEEE CCDC*, 2008, pp.564-568.

[16] H. Jing-yong, L. Hong-Da, Y. Wen-jie, and S. Nai-jun, “Fault Detection Method in Micro-Grid Multi-Pulse Thyristor Rectifier Circuit,” in *Proc. IEEE APPEEC*, 2012, pp.1-4.

[17] L. Hong-da, Y. Wen-jie, L. Hai, and Z. Dian-hua, “Fault Diagnosis Method in Controlled Rectifier Based on Support Vector Machines,” in *Proc. IEEE GCIS*, 2010, pp.235-238.

[18] J. Zhang, J. Zhao, D. Zhou, and C. Huang, "High-performance fault diagnosis in PWM voltage-source inverters for vector-controlled induction motor drives", *IEEE Trans. Power Electron*., vol. 29, no. 11, pp. 6087–6099, Nov. 2014.

[19] C. Ui-Min, J. Hae-Gwang, L. Kyo-Beum, and F. Blaabjerg, "Method for detecting an open-switch fault in a grid-connected NPC inverter system*," IEEE Trans. Power Electron*., vol. 27, no. 6, pp. 2726–2739, Jun. 2012.

[20] S. M. Jung, J. S. Park, H. W. Kim, K. Y. Cho, and M. J. Youn, "An MRAS-based diagnosis of open-circuit fault in PWM voltage-source inverters for pm synchronous motor drive systems" *IEEE Trans. Power Electron*., vol. 28, no.5, pp. 2514–2516, May 2013.

[21] R. L. D. Ribeiro, C. B. Jacobina, E. R. C. da Silva, and A. M. N. Lima, "Fault detection of open-switch damage in voltage-fed PWM motor drive systems*," IEEE Trans. Power Electron*., vol. 18, no. 2, pp. 587–593, Mar. 2003.

[22] P.G. Potamianos, E.D. Mitronikas, and A.N. Safacas, "Open-circuit fault diagnosis for matrix converter drives and remedial operation using carrier-based modulation methods," in *IEEE Trans. Ind. Electron*, vol. 61, no. 1, pp. 531-545, Jan. 2014.

[23] M. A. Rodriguez-Blanco, A. Claudio-Sanchez, D. Theilliol, L. G. Vela-Valdes, P. Sibaja-Teran, L. Hernandez-Gonzalez, and J. Aguayo-Alquicira, "A failure-detection strategy for IGBT based on gate-voltage behavior applied to a motor drive system," *IEEE Trans. Ind. Electron*, vol. 58, no. 5, pp. 1625–1633, May 2011.

[24] N.M.A. Freire, J.O. Estima, and A.J.M. Cardoso, "A voltage-based approach without extra hardware for open-circuit fault diagnosis in closed-loop PWM AC regenerative drives," in *IEEE Trans. Ind. Electron*, vol. 61, no. 9, pp. 4960-4970, Sept. 2014.

[25] V. Guerrero, J. Pontt, J. Dixon, and J. Rebolledo, "A novel noninvasive failure-detection system for high-power converters based on SCRs," in *IEEE Trans. Ind. Electron*, vol. 60, no. 2, pp. 450-458, Feb. 2013.

[26] H. Chen, and S. Lu, "Fault diagnosis digital method for power transistors in power converters of switched reluctance motors," in *IEEE Trans. Ind. Electron*, vol. 60, no. 2, pp. 749-763, Feb. 2013.

[27] J.O. Estima, A.J Cardoso, "A new algorithm for real-time multiple open-circuit fault diagnosis in voltage-fed PWM motor drives by the reference current errors," in *IEEE Trans. Ind. Electron*, vol. 60, no. 8, pp. 3496-3505 Aug. 2013.

[28] W. Rongjie, Z. Yiju, Z. Haifeng, and C. Bowen, "A fault diagnosis method for three-phase rectifiers," *Electrical Power and Energy Systems,* vol. 52, no. 1, pp. 266–269, April 2013.

[29] W. Rongjie, Z. Yiju, and Z. Haifeng, "Application of S-transform in fault diagnosis of power electronic circuits," *Scientia Iranica D*, vol. 19, no. 3, pp. 721-726, June 2012.

[30] L. Qingfeng, L. Zhaoxia, S. Jinkun, and W. Huamin, "Fault detection of rectifier based on residuals," *Physics Procedia*, vol. 25, pp. 1329 – 1336, April 2012.

[31] S. Nie, Y. Chen, X. Pei, H. Wang, and Y. Kang, “Fault diagnosis of a single-phase inverter using the magnetic field waveform near the output inductor,” in *Proc. IEEE APEC*, 2011, pp. 1648 - 1655.

[32] W. Baocheng, L. Danhe, S. Xiaofeng and W. Weiyang, “The studies of single-phase inverter fault diagnosis based on d-s evidential theory and fuzzy logical theory,” in *Proc. IEEE IPEMC*, 2006, pp. 1-4.

[33] S. Nie, X. Pei, Y. Chen, and Y. Kang “Fault diagnosis of PWM DC–DC converters based on magnetic component voltages equation” *IEEE Trans. Power Electron.*, vol. 29, no.9, pp. 4978–4988, Sep. 2014.

[34] Y. Chen, X. J. Pei, S. S. Nie, and Y. Kang, “Monitoring and diagnosis For The dc–dc converter using the magnetic near field waveform,” in *IEEE Trans. Ind. Electron*, vol. 58, no. 5, pp. 1634–1647, May 2011.

[35] S. S. Nie, Y. Chen, X. J. Pei, and Y. Kang, “A DSP-based diagnostic system for dc–dc converters using the shape of voltage across the magnetic components,” in *Proc. IEEE ECCE*, 2010, pp. 1908–1915.

[36] E. Ribeiro, A. J. M. Cardoso, and C. Boccaletti, “Open-circuit fault diagnosis in interleaved DC–DC converters” *IEEE Trans. Power Electron.*, vol. 29, no. 6, pp. 3091–3102, Jun. 2014.

[37] M. Shahbazi, E. Jamshidpour ,P. Poure, S. Saadate, and M.R. Zolghadri, “Open- and short-circuit switch fault diagnosis for nonisolated DC–DC converters using field programmable gate array,” in *IEEE Trans. Ind. Electron*, vol. 60, no. 9, pp. pp. 4136-4146, Sept. 2013

[38] E. Muljadi, D. Yildirim, T. Batan, and C.P. Butterfield, "Understanding the unbalanced-voltage problem in wind turbine generation," in *Proc. IEEE IAS,* 1999, vol.2, pp.1359-1365.

[39] Z. Hanzelka and Y. Varetsky, "Negative-sequence active power stream as an index of unbalance source" in *Proc. IEEE EPQU,* 2011, pp.1-4.

[40] T.E. Seiphetlho and A. PJ Rens, "The analysis of voltage and current unbalance by application of active and reactive power in the fundamental frequency negative-sequence components," in *Proc. IEEE ICHQP,* 2012, pp.420-426.

[41] D. Siemaszko, "Positive and negative sequence control for power converters under weak unbalanced networks," in *Proc. IEEE ESARS,* 2012, pp.1-6.

[42] R. Shao, "Power converters for residential PV and hybrid systems," PhD. dissertation, Office of Graduate Studies of University of New Brunswick, 2010.

[43] MATLAB R2013a, The MathWorks Inc., 2013

[44] B. Strobl, "A Diagnostic System for Asymmetries in Bridge Converters," in *Proc. EPE PEMC,* 2000, vol.2, pp.160-164.

[45] A.V. Jouanne, and B. Banerjee, "Assessment of voltage unbalance" *IEEE Trans. Power Delivery*, vol. 16, no. 4, pp. 3091–3102, Oct. 2001.

[46] Jacek M. Zurada, *Introduction to Artificial Neural Systems*, PWS Publishing Company, Inc., 1995.

[47] Kevin M. Passino and Stephen Yurkovich, *Fuzzy Control*, Addison Wesley Longman, Inc., 1998.

[48] F. J. Lin, Y. C. Hung, J. C. Hwang and M. T. Tsai, "3-Fault-Tolerant Control of a Six-Phase Motor Drive System Using a Takagi–Sugeno–Kang Type Fuzzy Neural

Network With Asymmetric Membership Function," *IEEE Trans. Power Electron.*, vol. 28, no. 7, pp. 3557-3572, July 2013.

[49] M. Cirrincione, A. Accetta, M. Pucci, and G. Vitale, "MRAS Speed Observer for High-Performance Linear Induction Motor Drives Based on Linear Neural Networks," *IEEE Trans. Power Electron.*, vol. 28, no. 1, pp. 123-134, Jan. 2013.

[50] Y. Liu, J. Zhao, R. Wang, and C. Huang, "Performance Improvement of Induction Motor Current Controllers in Field-Weakening Region for Electric Vehicles," *IEEE Trans. Power Electron.*, vol. 28, no. 5, pp. 2468-2482, May 2013.

[51] Y. K. Chen, Y. C. Wu, C. C. Song, and Y. S. Chen, "Design and Implementation of Energy Management System With Fuzzy Control for DC Microgrid Systems," *IEEE Trans. Power Electron.*, vol. 28, no. 4, pp. 1563-1570, April 2013.

[52] R. J. Wai, S. J. Jhung, J. J. Liaw, and Y. R. Chang, "Intelligent Optimal Energy Management System for Hybrid Power Sources Including Fuel Cell and Battery," *IEEE Trans. Power Electron.*, vol. 28, no. 7, pp. 3231-3244, July 2013.

[53] H. Kakigano, Y. Miura, and T. Ise, "Distribution Voltage Control for DC Microgrids Using Fuzzy Control and Gain-Scheduling Technique," *IEEE Trans. Power Electron.*, vol. 28, no. 5, pp. 2246-2258, May 2013.

[54] J. R. Jang, "ANFIS: adaptive network based fuzzy inference system," in *IEEE Trans. Syst., Man, and Cybern.*, vol. 23, no. 3, pp. 665-685, May 1993.

[55] M. R. Amaral, and A. J. M. Cardoso, "Using input current and output voltage ripple to estimate the output filter condition of the switch mode DC/DC converter," in *Proc. IEEE SDEMPED*, 2008, pp.1-6.

[56] M. A. Vogelsberger, T. Wiesinger, and H. Ertl, "Life-cycle monitoring and voltage-managing unit for DC-link electrolytic capacitors in PWM converters," *IEEE Trans. Power Electron.*, vol. 26, no. 2, pp. 493–503, Feb. 2011.

[57] A. M. R. Amaral and A. J. M. Cardoso, "A simple offline technique for evaluating the condition of aluminum-electrolytic-capacitors," *IEEE Trans. Ind. Electron.*, vol. 56, no. 8, pp. 3230–3237, Aug. 2009.

[58] M. L. Gasperi, "Life prediction modeling of bus capacitors in AC variable frequency drives," *IEEE Trans. Ind. Appl.*, vol. 41, no. 6, pp. 1430–1435, Nov./Dec. 2005.

[59] K. W. Lee, M. C. Kim, J. H. Yoon, S. B. Lee, and J. Y. Yoo, "Condition monitoring of DC-link electrolytic capacitors in adjustable-speed drives," *IEEE Trans. Ind. Appl.*, vol. 44, no. 5, pp. 1606–1613, Sep./Oct. 2008.

[60] G. M. Buiatti, J. A. M. Ramos, C. H. R. Garcia, A. M. R. Amaral, and A. J. M. Cardoso, "An online and noninvasive technique for the condition monitoring of capacitors in boost converters," *IEEE Trans. Instrum. Meas.*, vol. 59, no. 8, pp. 2134–2143, Aug. 2010.

[61] K. M. Tsang and W. L. Chan, "Low-cost sensing of equivalent series resistance for electrolytic capacitors," *IET Power Electron.*, vol. 2, no. 5, pp. 555–562, Sep. 2009.

[62] K. M. Tsang and W. L. Chan, "Simple method for measuring the equivalent series inductance and inductance and resistance of electrolytic capacitors," *IET Power Electron.*, vol. 3, no. 4, pp. 465–471, Jul. 2010.

[63] A. M. R. Amaral and A. J. M. Cardoso, “Simple experimental techniques to characterize capacitors in a wide range of frequencies and temperatures,” *IEEE Trans. Instrum. Meas.*, vol. 59, no. 5, pp. 1258–1267, May 2010.

[64] Y. M. Chen, H. C. Wu, M. W. Chou, and K. Y. Lee, “Online failure prediction of the electrolytic capacitor for LC filter of switching mode power converters,” *IEEE Trans. Ind. Electron.*, vol. 55, no. 1, pp. 400– 406, Jan. 2008.

[65] X. S. Pu, T. H. Nguyen, D. C. Lee, K. B. Lee and J. M. Kim, “Fault diagnosis of DC-link capacitors in three-phase AC/DC PWM converters by online estimation of equivalent series resistance,” *IEEE Trans. Ind. Electron.*, vol. 60, no. 9, pp. 4118-4127, Sept. 2013.

[66] K. Abdennadher, P. Venet, G. Rojat, J. M. Retif, and C. Rosset, “A realtime predictive maintenance system of aluminum electrolytic capacitors used in uninterrupted power supplies,” *IEEE Trans. Ind. Appl.*, vol. 46, no. 4, pp. 1644–1652, Jul./Aug. 2010.

Appendix A

The Fourier series expansion of the periodic signal w(t) with period T is as follows:

$$w(t) = \sum_{k=-\infty}^{\infty} w[k] e^{j2\pi \frac{k}{T} t} = w[0] + \sum_{k=1}^{\infty} A_k \cos(2\pi \frac{k}{T} t + \theta_k) \tag{A-1}$$

where;

$$w[k] = \frac{1}{T} \int_{-T/2}^{T/2} w(t)\, e^{-j2\pi \frac{k}{T} t}\, dt \tag{A-2}$$

$$A_k = 2\left|w[k]\right| \tag{A-3}$$

$$\theta_k = \angle\left(w[k]\right) \tag{A-4}$$

Figure A-1 shows the output rectifier voltage V_R at one diode O-C fault in the three-phase rectifier circuit with a resistive load. Therefore, the Fourier series expansion for V_R (t) can be calculated as follows:

$$w[k] = \frac{2}{T} \int_{0}^{T/2} w(t) \cos(2\pi \frac{k}{T} t)\, dt \tag{A-5}$$

where w(t) equals to V_R(t) and it is even function as shown in Figure A-1. w(t) can be written as follows:

$$w(t) = \begin{cases} V_{max} \cos(2\pi \frac{1}{T} t - \frac{\pi}{6}) & 0 \le t < T/6 \\ V_{max} \sin(2\pi \frac{1}{T} t) & T/6 \le t < T/2 \end{cases} \tag{A-6}$$

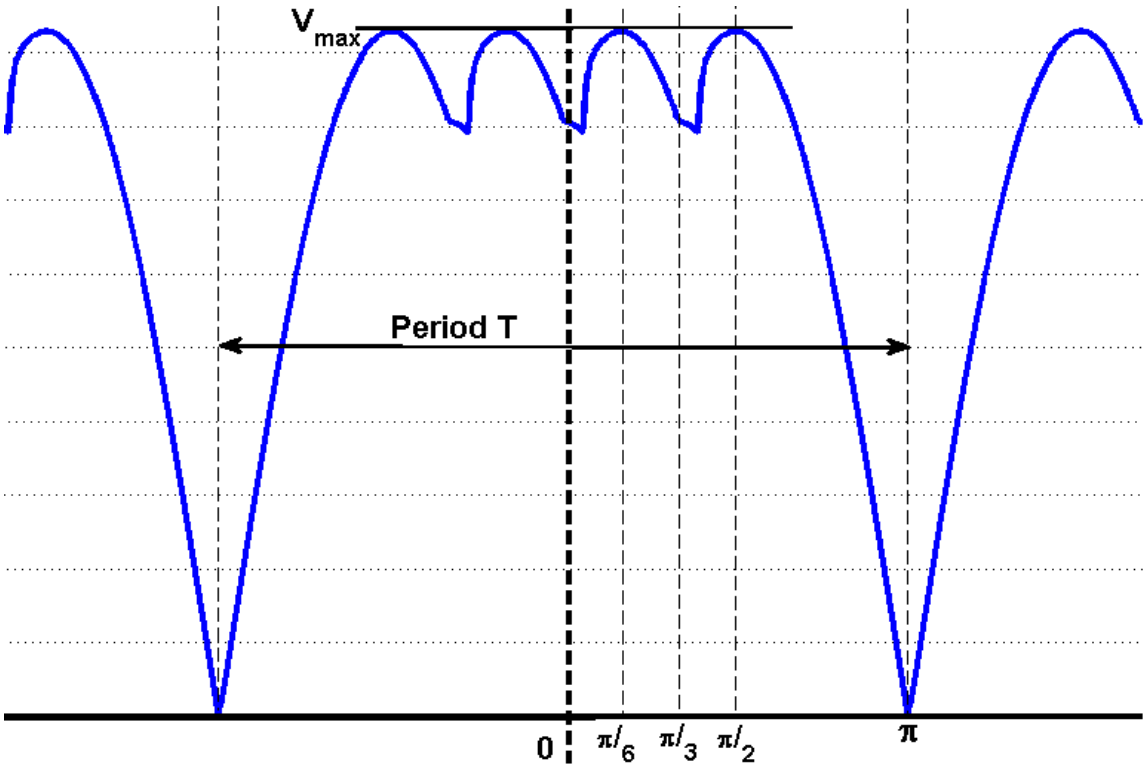


Figure A-1 Output rectifier voltage at one diode O-C fault

Therefore;

$$w[k]=\frac{2}{T}\left[\int_{0}^{T/6} V_{max}\ cos(2\pi\frac{1}{T}t-\frac{\pi}{6})\ cos\ (2\pi\frac{k}{T}t)\ dt\right] + \frac{2}{T}\left[\int_{T/6}^{T/2} V_{max}\ sin(2\pi\frac{1}{T}t)\ \ cos\ (2\pi\frac{k}{T}t)\ dt\right] \quad \text{(A-7)}$$

which could be simplified as follows:

$$w[k]=\frac{V_{max}}{T}\left[\int_{0}^{T/6}\left[cos\ (2\pi\frac{1}{T}t-\frac{\pi}{6}+2\pi\frac{k}{T}t)+cos\ (2\pi\frac{1}{T}t-\frac{\pi}{6}-2\pi\frac{k}{T}t)\right]dt\right]$$
$$+\frac{V_{max}}{T}\left[\int_{T/6}^{T/2}\left[sin\ (2\pi\frac{1}{T}t+2\pi\frac{k}{T}t)+sin\ (2\pi\frac{1}{T}t-2\pi\frac{k}{T}t)\right]dt\right] \tag{A-8}$$

$$w[k]=\frac{V_{max}}{T}\left[\frac{sin(2\pi\frac{1+k}{T}t-\frac{\pi}{6})}{2\pi\frac{1+k}{T}}\Bigg|_{0}^{T/6}+\frac{sin(2\pi\frac{1-k}{T}t-\frac{\pi}{6})}{2\pi\frac{1-k}{T}}\Bigg|_{0}^{T/6}\right]$$
$$-\frac{V_{max}}{T}\left[\frac{cos(2\pi\frac{1+k}{T}t)}{2\pi\frac{1+k}{T}}\Bigg|_{T/6}^{T/2}+\frac{cos(2\pi\frac{1-k}{T}t)}{2\pi\frac{1-k}{T}}\Bigg|_{T/6}^{T/2}\right] \tag{A-9}$$

Therefore, w[k] can be written as follows:

$$w[k]=\frac{V_{max}}{T}\left[A-B\right] \tag{A-10}$$

where;

$$A=\frac{sin(\frac{\pi}{6}+\frac{\pi k}{3})+sin(\frac{\pi}{6})}{2\pi\frac{1+k}{T}}+\frac{sin(\frac{\pi}{6}-\frac{\pi k}{3})+sin(\frac{\pi}{6})}{2\pi\frac{1-k}{T}} \tag{A-11}$$

$$A = \frac{T}{2\pi}\left[\frac{\frac{1}{2}\cos(\frac{\pi k}{3}) + \frac{\sqrt{3}}{2}\sin(\frac{\pi k}{3}) + \frac{1}{2}}{1+k} + \frac{\frac{1}{2}\cos(\frac{\pi k}{3}) - \frac{\sqrt{3}}{2}\sin(\frac{\pi k}{3}) + \frac{1}{2}}{1-k}\right]$$

(A-12)

$$A = \frac{T}{2\pi}\left[\frac{\cos(\frac{\pi k}{3}) - \sqrt{3}\,k\sin(\frac{\pi k}{3}) + 1}{1-k^2}\right]$$

(A-13)

On the other hand, B equals to

$$B = \frac{\cos(\pi + k\pi) - \cos(\frac{\pi}{3} + \frac{k\pi}{3})}{2\pi\frac{1+k}{T}} + \frac{\cos(\pi - k\pi) - \cos(\frac{\pi}{3} - \frac{k\pi}{3})}{2\pi\frac{1-k}{T}}$$

(A-14)

$$B = \frac{T}{2\pi}\left[\frac{-\cos(\pi k) - \frac{1}{2}\cos(\frac{\pi k}{3}) + \frac{\sqrt{3}}{2}\sin(\frac{\pi k}{3})}{1+k}\right] + \frac{T}{2\pi}\left[\frac{-\cos(\pi k) - \frac{1}{2}\cos(\frac{\pi k}{3}) - \frac{\sqrt{3}}{2}\sin(\frac{\pi k}{3})}{1-k}\right] \quad \text{(A-15)}$$

$$B = \frac{T}{2\pi}\left[\frac{-2\cos(\pi k) - \cos(\frac{\pi k}{3}) - \sqrt{3}\,k\sin(\frac{\pi k}{3})}{1-k^2}\right] \quad \text{(A-16)}$$

Based on (A-13) and (A-16), w[k] can be written as follows

$$w[k] = \frac{V_{max}}{2\pi(1-k^2)}\left[2\cos(\frac{\pi k}{3}) + 2\cos(\pi k) + 1\right] \quad \text{(A-17)}$$

Moreover, w[1] is calculated separately using (A-7) by put k =1

$$w[1] = \frac{V_{max}}{4\sqrt{3}} \quad \text{(A-18)}$$

Besides, w[0] is calculated using (A-17) as follows:

$$w[0] = \frac{5V_{max}}{2\pi} \quad \text{(A-19)}$$

Finally, A_k is deduced based on (A-17) and (A-18) as follows:

$$A_k = \left\{ \begin{array}{ll} \dfrac{V_{max}}{2\sqrt{3}} & , k=1 \\ \dfrac{V_{max}(3+2\cos(\frac{\pi k}{3}))}{2\pi(k^2-1)} & , k=2,4,6,..... \\ \dfrac{V_{max}(1-2\cos(\frac{\pi k}{3}))}{2\pi(k^2-1)} & , k=3,5,7,..... \end{array} \right\} \quad \text{(A-20)}$$

Figure A-2 illustrates V_R at two diodes O-C fault in the same branch.

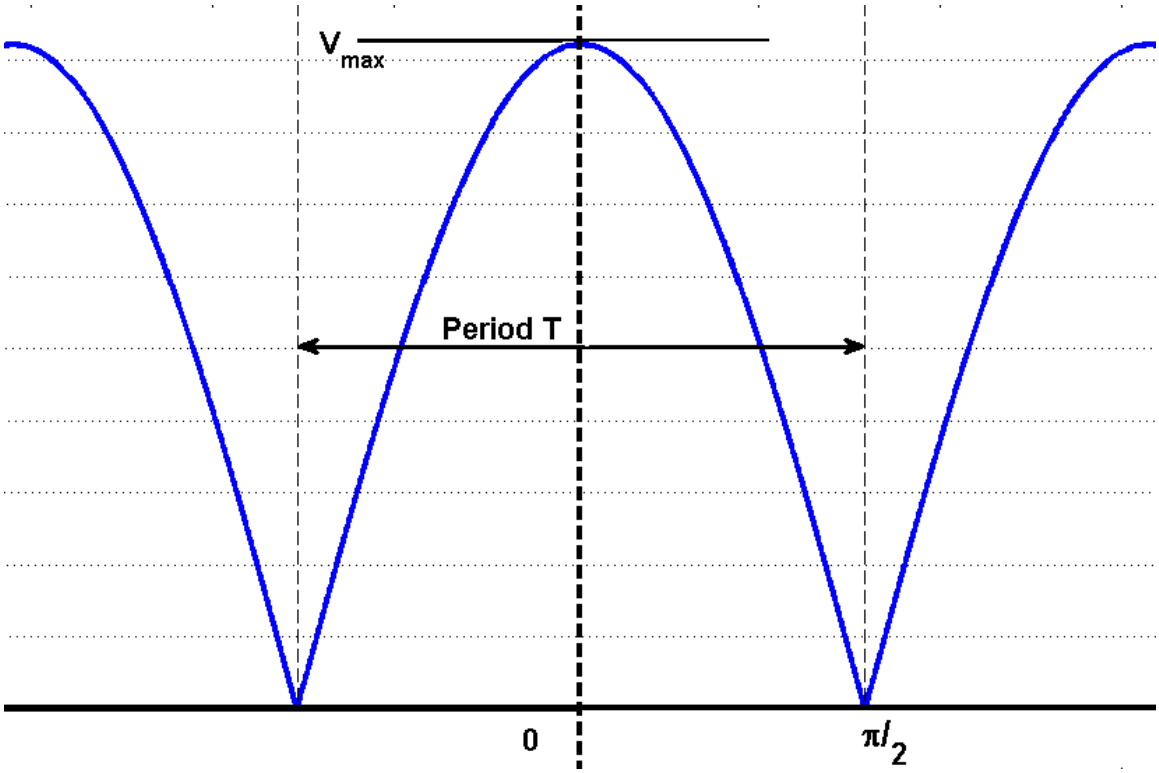


Figure A-2 Output rectifier voltage at two diodes O-C fault in same branch

Therefore, w(t) can be written as follows:

$$w(t)=V_{max}\ cos(2\pi\frac{1}{2T}t) \qquad , 0 \le t < T/2 \tag{A-21}$$

As a result, w[k] can be calculated, given that w(t) is an even function, as follows

$$w[k]=\frac{2}{T}\left[\int_0^{T/2} V_{max}\ cos(2\pi\frac{1}{2T}t)\ cos\ (2\pi\frac{k}{T}t)\ dt\right] \tag{A-22}$$

$$w[k]=\frac{V_{max}}{T}\left[\int_0^{T/2}\left[cos\,(2\pi\frac{1}{2T}t+2\pi\frac{k}{T}t)+cos\,(2\pi\frac{1}{2T}t-2\pi\frac{k}{T}t)\right]dt\right] \tag{A-23}$$

$$w[k]=\frac{V_{max}}{T}\left[\frac{sin(\pi\frac{1+2k}{T}t)}{\pi\frac{1+2k}{T}}\Bigg|_0^{T/2}+\frac{sin(\pi\frac{1-2k}{T}t)}{\pi\frac{1-2k}{T}}\Bigg|_0^{T/2}\right] \tag{A-24}$$

$$w[k]=\frac{V_{max}}{\pi}\left[\frac{sin(\frac{\pi(1+2k)}{2})}{1+2k}+\frac{sin(\frac{\pi(1-2k)}{2})}{1-2k}\right] \tag{A-25}$$

$$w[k]=\frac{V_{max}}{\pi}\left[\frac{(1-2k)\,cos(\pi k)+(1+2k)\,cos(\pi k)}{1-4k^2}\right] \tag{A-26}$$

$$w[k]=\frac{V_{max}}{\pi}\left[\frac{2\,cos(\pi k)}{1-4k^2}\right] \tag{A-27}$$

Finally, A_k can calculated based on (A-27) as follows:

$$A_k=\frac{V_{max}}{\pi(4k^2-1)} \tag{A-28}$$

Curriculum Vitae

Candidate's Full Name: Tamer Sayed Saleh Elsayed Kamel

Universities attended: 2010–2015 University of New Brunswick

2007-2010 Cairo University, M.Sc.

2002-2007 Cairo University, B.Sc.

Publications:

T. Kamel, Y. Biletskiy, and L. Chang, (Nov. 2014) "Fault diagnoses for industrial grid-connected converters in the power distribution systems", Forthcoming in *IEEE Transactions on Industrial Electronics*.

T. Kamel, Y. Biletskiy, and L. Chang, (April 2015) "Fault Diagnosis and On-line Monitoring for Grid-Connected Single-Phase Inverters", Forthcoming in *Electric Power Systems Research*

T. Kamel, M. Hassan, and A. El Morshdy, (Jan. 2012) "Advanced distance protection technique based on multiple classified ANFIS considering different loading conditions for long transmission lines in EPS", in *International Journal of Modeling Identification and Control*, vol. 16, no.2, pp. 108-121.

T. Kamel, M. Hassan, and A. El Morshdy, (Jan. 2011) "An ANFIS based distance relay protection for transmission lines

in EPS", in *International Journal Of Innovations In Electrical Power Systems*, vol.3, no.1, pp.1-13.

Submitted Publications: **T. Kamel**, Y. Biletskiy, and L. Chang, (May 2015) "Real time fault diagnosis for power electronic converters connected to small wind turbines", under review in *IEEE Transactions on Industrial Electronics*

T. Kamel, Y. Biletskiy, and L. Chang, (June 2015) "ANFIS-based open circuit fault detection and localization for power converters", under review in *IEEE Transactions on Power Electronics*

T. Kamel, Y. Biletskiy, and L. Chang, (June 2015) "ANFIS-based diagnosis for DC capacitor banks faults in power converter", under review in *IEEE Transactions on Power Electronics*

Conferences Presentations: **T. Kamel**, Y. Biletskiy, and L. Chang, (Sept. 2015) "On-line diagnosis for rectifier open circuit faults and input voltage unbalance based on the output dc voltage", in Proceedings of the *IEEE Energy Conversion Congress and Exposition (ECCE 2015)*, Montreal, QC, Canada

T. Kamel, Y. Biletskiy, and L. Chang, (June 2015) "Data communication to monitor power electronic converters", in Proceedings of the *IEEE International Symposium on*

Industrial Electronics (ISIE 2015), Búzios, Rio de Janeiro, Brazil

T. Kamel, Y. Biletskiy, and L. Chang, (June 2015) "Open circuit fault diagnoses for power electronic converters", in Proceedings of *ISIE 2015*, Búzios, Rio de Janeiro, Brazil

T. Kamel, Y. Biletskiy, and L. Chang, (May 2015) "Open circuit fault diagnosis for the power electronic converter stages using ANFIS algorithm", in Proceedings of the *IEEE Canadian Conference on Electrical & Computer Engineering (CCECE 2015)*, Halifax, NS, Canada

T. Kamel, Y. Biletskiy, and L. Chang, (May 2015) "Capacitor aging detection for the DC filters in the power electronic converters using ANFIS algorithm", in Proceedings of *CCECE 2015*, Halifax, NS, Canada

T. Kamel, C. Diduch, Y. Biletskiy, and L. Chang, (Sept. 2012) "Fault diagnoses for the DC filters of power electronic converters", in Proceedings of *ECCE 2012*, Raleigh, NC, USA

T. Kamel, Y. Biletskiy, C. Diduch, and L. Chang, (May 2012) "Fault diagnoses for all the stages of the power electronic converter" in Proceedings of *CCECE 2012*, Montreal, QC, Canada

T. Kamel, Y. Biletskiy, C. Diduch, and L. Chang, (May 2012) “Failure detection of the capacitor bank of the three phase diode rectifier” in Proceedings of *CCECE 2012*, Montreal, QC, Canada

T. Kamel, M. Hassan, and A. El Morshdy, (Sept. 2009) “Advanced distance protection scheme for long transmission lines in electric power systems using multiple classified ANFIS networks”, in Proceedings of the *IEEE International Conference on Soft Computing, with Words and Perceptions in System Analysis, Decision and Control, (ICSCCW)*, pp.1-5, Famagusta, North Cyprus

T. Kamel, M. Hassan, and A. El Morshdy, (Sept. 2009) “Using a combined artificial intelligent approach in distance relay for transmission line protection in EPS”, in Proceedings of *ICSCCW*, pp.1-6, Famagusta, North Cyprus

T. Kamel, M. Hassan, and A. El Morshdy, (Sept. 2009) “Application of artificial intelligent approach in distance relay for transmission line protection”, in Proceeding of the *International Scientific & Technical Conference in the Actual Trends in Development of Power System Protection and Automation*, pp. 28-36, Moscow, Russia